Measurement and Analysis of Magnetic and Magneto Optical Properties of Thin Films

By:

Wala Dizayee

A thesis submitted in partial fulfilment to the requirements for the degree of Doctor of Philosophy

University of Sheffield

Faculty of Science

Department of Physics and Astronomy

March, 2017

Acknowledgements

I would like to express my sincere gratitude to all those who have helped me throughout the duration of my PhD.

Firstly and foremost, a special appreciation and thanks to my supervisor Prof. G.A. Gehring for her continuous support, motivation and her immense knowledge. I am very grateful to her for giving me the opportunity to be one of her students and work within her group. Thanks for being a human, friend and supporter.

I am also extremely grateful to my second supervisor Prof. A.M. Fox for his assistance and valuable suggestions. I would like to thank Dr. H.J. Blythe for help and advice. My sincere thanks also go to Dr. J. Neal for assistance in repairing and re-running the MCD system again.

I would like to express my great appreciation to Dr. Steve M. Heald of the Argonne National Laboratory in United States, for his time investment and willingness to carry out EXAFS measurements on various samples. I would also like to extend a special thanks to Dr. Minju Ying and Dr. li Xiaoli for help and co- operation.

I would like to thank all department and faculty staff, especially the helium liquefier and the workshop technicians. I greatly appreciate the excellent assistance and the spiritual supports of my colleagues Mr. Hasan Albargi, Dr. Mohammed Alqahtani, Dr.Qi Feng, Dr. Marzook Alshammary, Mrs.Aliaa Zaki, Mrs. Fatma Gerriu, and Mr. Ahmad Saeedi.

Finally, I should like to express my sincere gratitude to my lovely parents, brothers and sister for the love, support, and constant encouragement throughout my studies.

Publications

- Minju Ying, **Wala Dizayee**, Z. X. Mei, X. L. Du, A. Mark Fox and Gillian A Gehring, **ZnO gap states investigated using magnetic circular dichroism,** J. Phys. D: Appl. Phys. 48 ,255502 (8pp), (2015).

- **Wala Dizayee**, Minju Ying, Mark F. Fox and Gillian A. Gehring, **Magnetic Circular Dichroism Measurements of Thin Films**, arXiv: 1505.03458.

- Minju Ying , Harry J. Blythe, **Wala Dizayee**, Steve M. Heald, Fatma M. Gerriu, A. Mark Fox, and Gillian A. Gehring, **Advantageous use of metallic cobalt in the target for pulsed laser deposition of cobalt doped ZnO films,** Appl. Phys. Lett. 109, 072403 (2016).

- Qi Feng, **Wala Dizayee**, Xiaoli Li, David S Score, James R Neal, Anthony J Behan, Abbas Mokhtari, Marzook S. Alshammari, Mohammed S. Al-Qahtani, Harry J Blythe, Roy W Chantrell, Steve M Heald, Xiao-Hong Xu, A Mark Fox and Gillian A Gehring, **Enhanced magnetic properties in ZnCoAlO caused by exchange-coupling to Co nanoparticles**, New J. Phys. 18, 113040, (2016).

- **Wala Dizayee**, Yalei Wang, A. Mark Fox and Gillian A. Gehring, **Magneto-Optics Properties of Graphite and graphene**. (Paper in preparation and title may change before submission).

- Minju Ying, **Wala Dizayee**, Mohammed S. Alqahtani, Jonathan Griffin, Alastair Buckley, A. Mark Fox and Gillian A Gehring , **Magnetic circular dichroism studies of amorphous MoOx**. (Will be submitted to a peer-reviewed journal).

- **Wala Dizayee**, Xiaoli Li, Steve M. Heald, Harry J. Blythe, A. Mark fox and Gillian A. Gehring, **Optimising and characterising the magnetic properties of thin films of cobalt doped ZnO fabricated by pulsed laser deposition.** (Will be submitted to a peer-reviewed journal).

- Fatma M. Gerriu, **Wala Dizayee**, Harry J. Blythe, Mark F. Fox and Gillian A. Gehring, **Magnetic Circular Dichroism study of point defects in ZnO**. (Will be submitted to a peer-reviewed journal).

Conferences

- **Postgraduate Magnetism Techniques Workshop**. National Science Learning Center, University of York, UK, 16-17 December 2013.

- Xiaoli Li, **Wala Dizayee**, James R. Neal, Harry Blythe, Steve M. Heald A. Mark Fox and Gillian A. Gehring, **Films containing some metallic cobalt exchange coupled to polarized defect states as a source of polarized electrons for spin injection**, The 14th REIMEI Workshop on Spin Currents and Related Phenomena, ILL, Grenoble, France, on February 10-13, 2014.

- Xiaoli Li, **Wala Dizayee**, James R. Neal, Harry Blythe, Steve M. HealdA. Mark Fox and Gillian A. Gehring , **Films containing some metallic cobalt exchange coupled to polarized defect states as a source of polarized electrons for spin injection,** IOP Magnetism2014, UK, University of Manchester, Manchester, April 07-08, 2014.

- **Wala Dizayee**, Yalei Wang, A. Mark Fox and Gillian A. Gehring, **Magneto-Optics Properties of Graphite and graphene**, Graphene 2014, Toulouse (France): May06-09, 2014.

- Minju Ying, **W. Dizayee**, S.M. Heald, H.J Blythe, A. M. Fox, and G. A. Gehring. **The effects of different precursors in the production of target for pulsed laser deposition on the magnetism of cobalt doped ZnO films**, IOP Magnetism2015, UK, University of Leeds, Leeds, March 30-31, 2015.

- **Wala Dizayee**, Xiaoli Li, Harry Blythe, Steve Heald, Mark Fox, **Gillian Gehring, Magnetism due to substitutional and metallic cobalt in ZnO films**, IOP Magnetism2015, UK, University of Leeds, Leeds, March 30-31, 2015.
- Minju Ying, **W. Dizayee**, S.M. Heald, H.J Blythe, A. M. Fox, and G. A. Gehring. **The effects of different precursors in the production of target for pulsed laser deposition on the magnetism of cobalt doped ZnO films**, ICM2015, Spain, Barcelona, July 5-10,2015.

- **Wala Dizayee**, Yalei Wang, A. Mark Fox and Gillian A. Gehring, **Magneto-Optics Properties of Graphite and graphene,** UK, University of Sheffield, Sheffield, April 04-05, 2016

Abstract

This thesis describes investigations of the magnetic and magneto-optical (MO) properties of three different types of thin films. The growth techniques, structural characterisation, magnetic, optical and magneto-optical measurements have been performed for a number of different materials grown as thin films. These are; graphite and graphene, for nonmagnetic ZnO and Al-doped ZnO and transition metal cobalt-doped ZnO with and without aluminum. Films were grown by pulsed laser deposition (PLD). Although, there has been much recent work on graphite and graphene, there has been no experimental work on the optical and magneto-optical (M-O) (Faraday rotation FR and magnetic circular dichroism MCD) measurements in the visible region. This thesis presents the first study of such measurements for both graphite and graphene thin films at room temperature in the optical region. To date, MCD has been used mainly to investigate the electronic states in magnetic materials; we have also extended it is use to the study of non-magnetic materials too. The MCD was measured on O polar ZnO and Zn polar ZnO films grown by molecular beam epitaxy (MBE), to study the impact of the surface termination on gap states. I also applied this method to ZnO films doped with 1% and 2% Al when, a negative MCD signal was observed near the band edge. I used different methods were used to make targets for PLD of ZnO doped with transition metal Co, with or without Al, and to grow films with different thicknesses. Magnetic, optical and magneto-optical measurements were performed to investigate the exciting area of magnetism in the ZnO host lattice that is coupled to that from magnetic nanoparticles of metallic cobalt. I used MCD to distinguish between the magnetism arising from the ZnO matrix and the magnetism arises from metallic cobalt.

Contents:

Chapter 1

Introduction and Thesis Structure

1.1 Introduction

This thesis is concerned with the characterisation of the magnetic, optical, structural and magneto-optical MO of a range of thin films; graphite and graphene, nonmagnetic ZnO doped with aluminium, polar ZnO based films and ZnCoO and ZnCoAlO films containing small amounts of metallic cobalt. The majority of these films were prepared by pulsed laser deposition (PLD) method, whereas a few others were prepared using different growth techniques, as described in the text. The main motivation of this study was to use the versatility of the magnetic circular dichroism (MCD) technique to identify and measure the properties of the gap states and defect states in different types of thin films in the visible region of the spectrum.

The effect of applying various conditions to influence the magnetic and magneto-optical properties of the ablated films will be investigated. The conditions during the growth method can be changed by varying various parameters; like the deposition time for film growth, substrate temperature, the precursors and the oxygen pressure. SQUID magnetometry was performed to measure the hysteresis loops, low field magnetisation as a function of temperature and zero field-cooled/

field-cooled ZFC/FC measurements. X-ray diffraction (XRD) was performed for all films, extended x-ray absorption fine structure (EXAFS) for ZnCoO and ZnCoAlO films, additionally, the techniques of scanning probe microscopy (AFM), were used for graphite films, all the measurements done in order to investigate the environment of doped species and surface film structure topography. Absorption and reflection measurements were performed to investigate the band gap. Finally, MCD measurements were used to explore the spin polarisation of the electronic states and the band structure of the films.

Graphite is a layered structure of carbon atoms; they are arranged in a honeycomb lattice in each layer, the separation between two carbon atoms is 1.42Å, and the inter plane distance is 3.35Å [1-3]. Graphene is, however, a single layer of graphite [3-5]. The interest in graphite is well known, recently, however, there has been a massive increase in the interest in graphene, this is especially because of it is optical properties and high conductivity, which made it a good candidate for many applications, such as in terahertz-IR detectors and solar cells [2, 6].

The magneto-optical properties, Faraday rotation (FR) and magnetic circular dichroism (MCD) of both graphite and graphene have been investigated in the IR region [7-9]. This thesis contains a report of the first studies of FR and MCD in the visible region in this material, and the results for FR for graphite are compared with theory.

In classical electronics the electronic charge is used to carry information. However, the electron spin is the most important aspect of magnetic materials and a new discipline is the use of the electron's spin to carry or process information; this area is known as spintronics. Possible materials for use in spintronics are diluted

magnetic semiconductors, (DMS). The unique properties of ZnO offer good technological applications, making it one of the most valuable materials of the diluted magnetic semiconductors DMS group. ZnO is a transparent material in the visible spectrum region with a wide band gap of around 3.4eVat room temperature RT. [10-12]

The unique properties of ZnO depended on the energy gap states, which are due to the presence of intrinsic point defects, particularly oxygen vacancies and zinc interstitials [10-12]. These, point defects in ZnO are donors; hence ZnO is an n-type material [10-12]. Consequently, controlling the concentration of defects and impurities, can lead both to improved performance and to new applications. In addition, doping with transition metals (TM) such as Co, with Al as an additional donor, has increased the magnetism in pure ZnO, for example, due to the increase in the number of carriers when co-doping with Co and Al [13, 14].

Zinc oxide is polar material, hence there are differences between the samples grown with O-polar or Zn-polar surfaces; this includes the density of defects and the different optical states that are related with the O-polar sample [15-17]. We have used MCD to investigate the effect of polar ZnO with O- or Zn- terminations on the gap states because of the many applications of polar films of ZnO [18, 19].

We have also used MCD technique; to illustrate it is capability to measure the weak absorbing gap states in non-magnetic thin films of ZnO.

It still remains under debate as to whether the source of the observable room temperature ferromagnetism in thin films of ZnO when doped with different TM such as; Co, Fe and Mn, is due to the presence of nanoparticles of ferromagnetic

material [20-23]. We investigate the possibility of achieving magnetism in the ZnO lattice, which is in coupled with the magnetism of nanoparticles of metallic cobalt. A number of different targets, using various growth conditions such as target annealing and the addition of Al to the target, have been used to grow thin films of ZnCoAlO and ZnCoO with different thicknesses [24-25].

1.2 Thesis Structure

This thesis consists of seven chapters. The aim of this thesis is to study and measure the magnetic, optical and magneto optical properties of oxide and graphite thin films and also graphene. The body of the thesis consists of seven chapters, as follows;

- **Chapter One,** contains the introduction of the thesis.

- **Chapter Two,** contains a brief presentation of the theory of magneto – optical systems, magneto-optics theory in terms of dielectric tensor and a discussion about the classical and quantum theories of absorption.

- **Chapter Three,** describe the experimental techniques used in the thesis with a brief details and physical background. This includes PLD, SQUID magnetometer, Dektak surface profiler, optical measurements, and magnetic circular dichroism MCD.

- **Chapter Four,** contains a discussion of the optical and magneto-optical studies of graphite and graphene thin films in the visible region over an energy range of between 1.5 - 4.5 eV at room temperature. It also gives a literature review on the graphite and graphene and their properties.

- **Chapter Five,** describes the ability of the magnetic circular dichroism MCD technique to identify the weakly absorbing gap states in a set of nonmagnetic ZnO thin films. A discussion of the optical and magneto optical data will be presented also in this chapter.

- **Chapter Six,** the investigation of structural, magnetic, and magneto-optical properties of a series of ZnCoO and ZnCoAlO thin films, will be described, to explain the effect of varying the growth conditions at the origin of the magnetisation within the energy states for these films.

- **Chapter Seven,** includes a summary of the results achieved in the thesis and a proposals for future work and projects.

1.3 References

[1] D. D. L. Chung, "Review graphite," Journal of Materials Science, vol. 37, pp. 1475-1489, (2002).

[2] M. Fox, Optical Properties of Solids vol. Second Edition ed. Oxford Universtiy: Press Inc., New York (2010).

[3] B. Partoens and F. M. Peeters, "From graphene to graphite: Electronic structure around the K point," Physical Review B, vol. 74, pp. 075404, (2006).

[4] X. Li, "Epitaxial Graphene Films On Sic: Growth, Characterization, And Devices," Institute of Technology: Georgia. p. 141, Georgia, (2008).

[5] C. N. R. Rao, et al., "Graphene: The New Two-Dimensional Nano material," Angewandte Chemie-International Edition, vol. 48, pp. 7752-7777, (2009).

[6] C. Lee, et al., "Optical response of large scale single layer graphene," Applied Physics Letters, vol. 98, pp.071905, (2011).

[7] T. G. Pedersen, "Tight-binding theory of Faraday rotation in graphite," Physical Review B, vol. 68, p. pp.245104, (2003).

[8] G. E. Jellison, Jr., et al., "Measurement of optical functions of highly oriented pyrolytic graphite in the visible," Physical Review B, vol. 76, p. pp.085125, (2007).

[9] J. C. Martinez, et al., "Giant Faraday and Kerr rotation with strained graphene," Optics Letters, vol. 37, pp. 3237-3239, (2012).

[10] M. Ying, et al., "ZnO gap states investigated using magnetic circular dichroism," Journal of Physics D-Applied Physics, vol. 48, p. 255502, (2015).

[11] U. Ozgur, et al., "A comprehensive review of ZnO materials and devices," Journal of Applied Physics, vol. 98, p. 041301, (2005).

[12] Sze. S. M, Semiconductor Devices Physics and Technology vol. 2nd edn. New York: Wiley, (2002).

[13] X. H. Xu, et al., "Carrier-induced ferromagnetism in n-type ZnMnAlO and ZnCoAlO thin films at room temperature," New Journal of Physics, vol. 8, p. 135, (2006).

[14] F. Leiter, et al., "Oxygen vacancies in ZnO," Physica B-Condensed Matter, vol. 340, pp. 201-204, (2003).

[15] T. Nakamura, et al., "Near-surface structure of polar ZnO surfaces prepared by pulsed laser deposition," Thin Solid Films, vol. 559, pp. 88-91, (2014).

[16] J. Williams, et al., "Polarity-dependent photoemission spectra of wurtzite-type zinc oxide," Applied Physics Letters, vol. 100, p. 051902, (2012).

[17] D. C. Oh, et al., "Comparative study of photo luminescence for Zn-polar and O-polar faces of single-crystalline ZnO bulks," Applied Physics Letters, vol. 93, p. 241907, (2008).

[18] H. Tampo, et al., "Two-dimensional electron gas in Zn polar ZnMgO/ZnO hetero structures grown by radical source molecular beam epitaxy," Applied Physics Letters, vol. 89, p. 132113,(2006).

[19] Z. L. Wang, "ZnO nano-wire and nan-obelt platform for nanotechnology," Materials Science & Engineering R-Reports, vol. 64, pp. 33-71, (2009).

[20] S. A. Wolf, et al., "Spintronics: A spin-based electronics vision for the future," Science, vol. 294, pp. 1488-1495, (2001).

[21] M. Bibes and A. Barthelemy, "Oxide spintronics," Ieee Transactions on Electron Devices, vol. 54, pp. 1003-1023, (2007).

[22] U. Ozgur, et al., "A comprehensive review of ZnO materials and devices," Journal of Applied Physics, vol. 98, p. 041301, (2005).

[30] J. Coey, Magnetism and Magnetic Materials, first edition ed. (Cambridge University press, 2010).

[24] Q. Feng, et al., "Enhanced magnetic properties in ZnCoAlO caused by exchang-ecoupling to Co nanoparticles," New Journal of Physics, vol. 18, p. 113040, (2016).

[25] M. J. Ying, et al., "Advantageous use of metallic cobalt in the target for pulsed laser deposition of cobalt-doped ZnO films," Applied Physics Letters, vol. 109, 072403, (2016).

Chapter 2

Magneto-Optics Background in Magnetic Oxide Materials

2.1 Introduction

This chapter provides an overview of the literature that was considered to be pertinent to this investigation. Specifically, this section provides an analysis of key concepts needed to understand the experimental techniques applied in this investigation including magneto-optics, magneto-optics in terms of the dielectric tensor.

2.2 Fundamentals of Magnetism

All substances are made up of atoms that contain electrons, with m_e mass and $-e$ charge that are in constant motion. The motion of electrons is commonly referred to as atomic currents. Accordingly, there are three types of currents: atomic current, displacement current, and the conventional current.

These three sources of current within an atom may result in a magnetic moment of the free atom;

- The change in the orbital momentum of an electron that is caused by the introduction of a magnetic field.
- The orbital angular momentum of the electrons, *l*, results from the motion of electrons around the nucleus.
- The intrinsic electrons spin, *s*,.

The orbital angular momentum of electron and their intrinsic spin cause paramagnetic contributions to the process of magnetization while the shift in the orbital momentum of an electron that is caused by inducing a magnetic field results in a diamagnetic contribution. Magnetic moments emanate from electron shells that are partially filled, since atoms that have filled electron shells have zero orbital momentum and zero spin because the orientation of the magnetic moments of the electrons cancel each other out [1-5].

The relationship between an applied magnetic field *H* and the magnetic induction *B* in a material is given by:

$$B = \mu_o(H + M) \qquad \text{..... (2.1)}$$

Where, $\mu_o = 4\pi \times 10^{-7} H\text{m}^{-1}$ is the free space magnetic permeability, and *M* is the magnetisation. The variation of *M* in an applied magnetic field *H*, defines the magnetic properties of the material.

The susceptibility χ, is very important magnetic feature, which is defined as the ability of the material to become magnetiesd, and it is a temperature dependent and a dimensionless, is given by:

$$\chi = \frac{\partial \mathrm{M}}{\partial \mathrm{H}}\Big|_{\mathrm{H}\to 0} \quad \text{OR} \quad \chi = \frac{\mu_o \mathrm{M}}{\mathrm{B}} = \frac{\mathrm{M}}{\mathrm{H}} \qquad \text{..... (2.2)}$$

Moreover, the property of the material that describes the degree of the materials magnetisation which responds to a linear magnetic field is called the permeability μ, and given by:

$$\mu = \frac{\mathrm{B}}{\mathrm{H}} \qquad \text{..... (2.3)}$$

While, the relative permeability of the material μ_r is given by:

$$\mu_r = \frac{\mu}{\mu_o} \qquad \text{..... (2.4)}$$

Where, it is the ratio of the material permeability, μ, to the free space permeability, μ_o (which is constant). Also, known that μ_r is equal to 1+ χ, therefore we now have;

$$B = \mu_o(1+\chi)H = \mu_r \mu_0 H \qquad \text{..... (2.5)}$$

The values of susceptibility χ and the relative permeability of the material μ_r are used to classify the magnetic materials. Materials with a small and negative magnetic susceptibility χ are known as diamagnetic. This happens by applying an external magnetic field to the material, producing an induced electromagnetic force

that accelerates the electrons in the materials with a constant independent of temperature. Whereas, the permeability and susceptibility χ are positive in paramagnetic materials, also χ is small and decreases as a function of temperature increasing in paramagnetic materials. This relation is known as the Curie-Weiss law, as written by:

$$\chi(T) = \frac{C}{T \pm \theta} \qquad \text{..... (2.6)}$$

Where T is the temperature, C is the Curie constant and θ it is known as non-negative constant or the temperature parameter.

On the other, the susceptibility, χ, for a ferromagnetic material is positive too, similar to the paramagnetic materials, but it is much larger than that for para materials [1-5]. The plus and minus sign for θ is used for anti-ferromagnetism and ferromagnetism, respectively.

The main difference between paramagnetism and ferromagnetism is that in the absence of an applied field the ferromagnetism still has a spontaneous magnetisation.

The theory of the localized moment explains that, electrons originate the ferromagnetism in the materials. In an insulator, the atom magnetic moments and the electrons are localized and cannot move in the crystal, where the majority of the spins stay aligned due to the exchange mechanism among them. While the electrons are not localized according to band theory and they are free to move from atom to another, originating the ferromagnetism in the crystal.

Under a critical temperature, more spins are aligned by applying a magnetic field, and the system achieves its maximum magnetization and is saturated; this point is known as the saturation magnetization M_s. When by removing the external field, the weak coupled spins will move randomly due to the thermal fluctuation, thus the magnetic moment does not vanish, like in paramagnet; rather, this permanent magnetization is known as remanence, or remaining magnetization M_r. The magnetic field wanted to remove the remaining magnetization is call the coercively, or coercive field Hc . Whereas, the ferromagnetic material have a zero coercive field and behaves like a paramagnet, above a critical temperature; is known as the Curie temperature *Tc*.

Accordingly, in free spins where magnetic energy, -mB, competes with thermal energy, then;

$$\chi(T) = \frac{C}{T} \qquad \text{..... (2.7)}$$

If the spins feel exchange interaction favoring ferromagnetism, and accordingly, θ is about the same as *Tc* the Curie temperature, which is a characteristic property for ferromagnetic materials, that gives;

$$\chi(T) = \frac{C}{T - T_c} \qquad \text{..... (2.8)}$$

Where, for T < Tc the material is ferromagnetism due to the magnetic moments alignment, whilst, above Tc, the thermal variation destroy the alignment and the material revert to paramagnetic behaviour.

Whereas, the susceptibility for antiferromagnetic materials the exchange interaction tends to align the magnetic moments antiparallel to each other. The susceptibility is given by:

$$\chi(T) = \frac{C}{T+\theta} \qquad \text{..... (2.9)}$$

The susceptibility for antiferromagnetic materials is a temperature dependent, were it increases with a decrease in temperature to a maximum value known as the Neel temperature T_N . The materials is antiferromagnetic below T_N , $T_N \leq \theta$, and above T_N the material is paramagnetic [1, 6].

2.3 Magneto-Optical Effect

Magneto-optics (MO) is a powerful system used to identify the origin of ferromagnetism in the materials spectroscopicly. It may be used to determine whether any secondary impurity phases are the source of the ferromagnetism, or if it is caused by the effect of TM ions added to the host lattice material or by a polarized defect band. It describes how light undergoes modification when passed through a crystal under the influence of an external magnetic field. In an electromagnetic wave, in free space, the direction of the electric field is called the polarization, which is constant as the wave propagates. The polarization is linear if the electric field vector, E, points along a constant direction. Hence, for isotropic transparent

materials with refractive index *n*, the relation between the magnitude of wave vector q and the angular frequency ω is given by this formula;

$$q = \frac{n\omega}{c} = \frac{2\pi}{\lambda/n} \qquad \text{..... (2.10)}$$

where, *c* is the speed of light. If light is passed through an absorbing material of thickness *l*, the refractive index *n* and *q* become complex, $\tilde{n}\ and\ \tilde{q}$, the matter would be presented; then equ. (2.10) becomes:

$$\tilde{q} = \frac{\tilde{n}\omega}{c} \qquad \text{..... (2.11)}$$

Where $\tilde{n}$ is the sum of real, n_o, and imaginary, *k*, parts, $\tilde{n} = n_0 + ik$; *k* is also called the extinction coefficient. Then, when an electric vector E_{in} of light, incident on a transparent material of thickness L, the electric vector E_{out} of the transmitted beam, is given by the following:

$$E_{out}e^{i\omega t} = E_{in}e^{i\omega t}e^{i\tilde{q}L}$$

$$= E_{in}e^{i\omega t}exp\left(i\frac{\omega\tilde{n}}{c}L\right)$$

$$= E_{in}e^{i\omega t}[exp\left(i\frac{\omega n_0}{c}L\right).exp\left(-\frac{\omega k}{c}L\right)] \qquad \text{..... (2.12)}$$

There are two refractive indices in a magnetic medium; $\tilde{n}_+ \neq \tilde{n}_-$, both of which may be complex. Hence we must discuss propagation of light through a magnetic

medium in terms of two circularly polarised beams. Light that is linearly polarised comprises of equal parts of right and left circularly polarised light RCP and LCP. This implies the equation above can be rewritten into:

$$\tilde{n}_{\pm} = n_{0\pm} + ik_{\pm} \quad \text{..... (2.13)}$$

Figure (2.1) (a) and (b) shown a summary of the representation of RCP (+) sign and LCP (-) signs.

Removed
by the author
for copyright reasons

Figure (2.1): (a) linear polarised light is made up of equal parts of LCP and RCP light. (b) If the LCP and RCP light after passing through a perpendicularly magnetized sample are unequal, then the transmitted or reflected light becomes elliptically polarised and rotated. Where θ is the rotation angle and φ is the ellipticity angle, where both actually are very small for our experiments. Figure adapted from A.Behan [7] after few amendment have been taken.

From figure (2.1a) [7], it is evident that linear light has two equal parts RCP and LCP, where, these parts are unequal after passing through a magnetic field, the reflected light is elliptically polarised and rotated parallel to the direction of the magnetic field as illustrated in figure (2.1b). The RCP light component, in this case, is smaller than the LCP light component.

The MO effect is observable when the refractive indices of RCP and LCP upon recombination are not equal $\tilde{n}_+ \neq \tilde{n}_-$, where, $\tilde{n}_+$ and $\tilde{n}_-$ represent the refractive indices for right and left circularly polarised light, respectively. This results in a shift in the relative amplitude and phase of the RCP and LCP light, which indicates a magnetic circular birefringence. This is demonstrated in figure (2.1b) where light is polarised elliptically by a rotation of angle θ and is accompanied by a change in intensity.

MO effect is a result of a direct or indirect split of energy levels in an applied magnetic field. The absorption of light and refractive index in a solid are occurs by electric dipole transitions. Circularly polarised transitions occur between electronic states that are magnetically quantized, where $\Delta m_j = \pm 1$, mj is the orbital quantum number. Therefore, spin-orbital coupling is playing an essential role for orbital moments which reflecting information about the system magnetism. For a weak spin-orbit coupling the allowed selection rules are $\Delta m_s = 0$ and $\Delta m_l = \pm 1$, where m_s is the electron spin ($\pm\frac{1}{2}$) for spin up and down, respectively, this be a symbol for orbital moment that gives information about the magnetism of the system [6, 8].

In transmission, Faraday effects , FR, is due to the difference between the real parts of the refractive indices for left and right CP light, while, a measure of the difference in absorption for left and right CP light is known as the magnetic circular dichroism, MCD [9]. All the experiments performed for this work were done in Faraday geometry. The FR is determined by the weighted average of all the transitions within the material. In a spectral range where the crystal is not absorbing, the FR effect is finite, unlike the MCD that depends on absorption.

As mentioned earlier the magnetic circular dichroism (MCD) presents a difference in intensity between right and left circularly polarised light at a given frequency ω, and is non-zero at energies where the crystal is absorbing, because it is depends on the transitions at frequency ω. For that reason, MCD is very useful to determine the nature of the magnetic state, and therefore the MCD measurements are the most important investigation in this thesis. Furthermore, the FR is used, to check if the MCD effect is not due to the medium is absorbing at the band edge, but it might be due to the materials intrinsic magnetism or induced by an external magnetic field.

As been predicted from quantum selection rules, the transition with $\Delta m_l = \pm 1$ occur in RCP and LCP lights respectively. This results in two possible sources of an MO effect. There might be differences in the absorption energies for RCP and LCP light if the condition bands or valences are split or due to the difference in the RCP and LCP strength which is due to the population difference in the orbital states.

In the cases, where only one of these effects exists, it shows a distinct line shape, which are referred to a diamagnetic and paramagnetic line shapes. A diamagnetic line shape is shown when RCP and LCP transitions take place at different energy levels due to band splitting, consequently, the dispersive feature in the MCD is occurring due to the transitions at energy differences, as shown in figure (2.2a). The paramagnetic line shape is seen when the occupation of the orbital states that are participated in transition for RCP and LCP light, is different. The transitions take place at the same energy level but with differences in strengths implying that subtracting one from the other results in MCD peak, as seen in figure (2.2b), more details in the following sections.

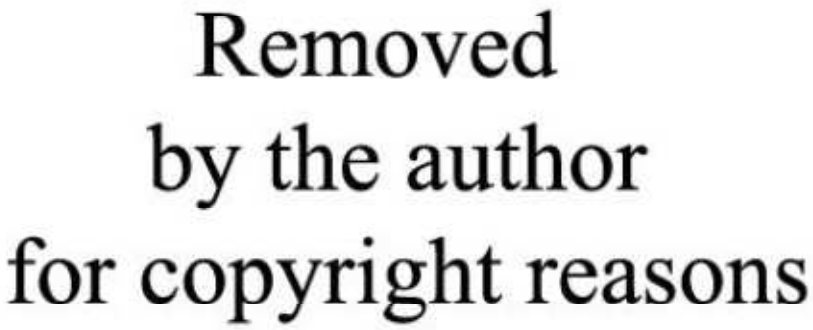

Figure (2.2): (a) Diamagnetic effect from LCP and RCP transitions occurring at different energies. (b) Paramagnetic effect from LCP and RCP transitions occurring at the same energies [7].

Furthermore, the process of separating the effects of population and energy is an extreme case since it is unlikely for population differences to exist without having some form of energy splitting. Hence, the only possibility to have the paramagnetic line shape if the spectral resolution is broad enough to determine the splitting which results in a difference in the population [7, 10-11]. The pure diagrammatic effect will depict a dispersive feature with equal size of positive and negative parts. If these parts are not sized equally, then the populations of the states are not equal too.

Faraday rotation can be applied in determining whether an MCD signal that is detected is real and not a construction that can emanate from a sample that absorbs strongly at the band edge. Figure (2.2) above demonstrates this consistency, where a peak in Faraday rotation is shown at the zero point of the MCD signal, and vice versa. This is due to the Kramers-Kronig relation [9, 12].

2.4 Macroscopic Theory

2.4.1 Magneto-Optics Theory in Terms of Dielectric Tensor

In this section we show how $n_{\pm}$ arises from off-diagonal terms in the dielectric tensor. The dielectric tensor $\tilde{\varepsilon}$ is used to describe the propagation of electromagnetic waves through a medium at optical frequencies, where an external magnetic field is applied. In a uniaxial crystal that is magnetized along the optical propagation direction of light $\vec{M} \,||\, \hat{z}$, so the tensor has the form written in equ.(2.14) [9, 13]:

$$\tilde{\varepsilon} = \begin{pmatrix} \tilde{\varepsilon}_{xx} & i\tilde{\varepsilon}_{xy} & 0 \\ -i\tilde{\varepsilon}_{xy} & \tilde{\varepsilon}_{xx} & 0 \\ 0 & 0 & \tilde{\varepsilon}_{zz} \end{pmatrix} \quad \text{…….……. (2.14)}$$

Where, in a magnetic medium, the off-diagonal components $\tilde{\varepsilon}_{xy}$ are non-zero, will shown later. The dielectric tensor $\tilde{\varepsilon}_{xy}$ for an absorbing material is complex with a real and imaginary part, given by $\tilde{\varepsilon}_{ij} = \varepsilon'_{ij} + i\varepsilon''_{ij}$.

Now, eqn.(2.14) gives the propagation of light in a medium with dielectric tensor. Then based on Maxwell equations in a non-conducting medium, where total density, j = 0, ρ = 0, then:

$\nabla.\mathbf{B} = 0$ ……...……. (2.15)

$\nabla.\mathbf{D} = \rho = 0$ ……..……. (2.16)

$\vec{\nabla} \times \vec{\boldsymbol{H}} = j + \frac{\partial \mathbf{D}}{\partial t} = \frac{\partial \vec{\mathbf{D}}}{\partial t}$ ……..……. (2.17)

$\vec{\nabla} \times \vec{\mathbf{E}} = -\frac{\partial \vec{\mathbf{B}}}{\partial t}$ ...……...……. (2.18)

The electric displacement and magnetic field are related by [9]:

$\vec{\mathrm{B}} = \mu_0 \vec{\mathrm{H}}$ ……..……. (2.19)

$\vec{D} = \tilde{\varepsilon}\varepsilon_o E$ ……..…….. (2.20)

At low frequency the relation of $\vec{M} = \chi \vec{H}$ for ferromagnets and $\mu \neq 1$, however, at optical frequencies it could be assumed that $\mu_r = 1$ even for ferromagnets [1, 9, 14-16].

Solutions are taken at frequency ω propagation along z-axis. The electric fields are given by the form:

$$\frac{\omega^2\tilde{n}_{\pm}^2}{c^2}E_o(\hat{e}_x \pm i\hat{e}_y)exp[i(\omega t - q_{\pm}z)] = \varepsilon_o\mu_o\omega^2E_o[(\tilde{\varepsilon}_{xx} \pm \tilde{\varepsilon}_{xy})\tilde{e}_x + (i\tilde{\varepsilon}_{xy} \pm$$

$$i\varepsilon xxeyexpi\omega t - q\pm z \qquad \text{…….…….. (2.21)}$$

Where $q_{\pm}^2 = \frac{\omega^2\tilde{n}_{\pm}^2}{c^2}$ and $c = \frac{1}{\sqrt{\varepsilon_0\mu_0}}$, then solution is for complex refractive indices, $\tilde{n}_{\pm}$. Solving Maxwell's equations using eqn, (2.14), (2.20) in (2.21) we find that

$$\left(\frac{\omega^2}{c^2}(\varepsilon_{xx} \pm \varepsilon_{xy}) - q_{\pm}^2\right)E_{\pm} = 0 \qquad \text{…….…….. (2.22)}$$

This may be solved for $\tilde{n}_{\pm}$. one find

$$\tilde{n}_{\pm}^2 = \tilde{\varepsilon}_{xx} \pm \tilde{\varepsilon}_{xy} \quad \text{and} \quad \tilde{\varepsilon}_{\pm} = \tilde{\varepsilon}_{xx} \pm \tilde{\varepsilon}_{xy} \qquad \text{……..….. (2.23)}$$

which simplified to give:

$$\tilde{n}_{\pm} = \sqrt{\tilde{\varepsilon}_{xx}} \pm \frac{\tilde{\varepsilon}_{xy}}{2\sqrt{\tilde{\varepsilon}_{xx}}}$$, were provided that $\tilde{\varepsilon}_{xx} \gg \tilde{\varepsilon}_{xy}$. ……. (2.24)

As been mentioned earlier, MO effects are given by the difference in refractive index between LCP and RCP light, therefore;

$$\tilde{n}_+ - \tilde{n}_- = \frac{\tilde{\varepsilon}_{xy}}{\sqrt{\tilde{\varepsilon}_{xx}}} \qquad \text{……. (2.25)}$$

And

$$\Delta\tilde{n} = \tilde{n}_+ - \tilde{n}_- = \Delta n + i\Delta k \quad \text{..... (2.26)}$$

Where; $\mathrm{Re}\Delta\tilde{n} = \Delta n$ and $\mathrm{Im}\Delta\tilde{n} = \Delta k$

In a sample of thickness l_0, the Faraday rotation θ_F , and the MCD, η_F are given by:

$$\theta_F = Re\left[\frac{\omega l_0}{2c}(\tilde{n}_+ - \tilde{n}_-)\right] = \frac{\omega l_0}{2c}\Delta n \quad \text{..... (2.27)}$$

$$\eta_F = tan\left[\mathrm{Im}[\frac{\omega l_0}{2c}(\tilde{n}_+ - \tilde{n}_-)]\right] \approx \frac{\omega l_0}{2c}\Delta k \quad \text{..... (2.28)}$$

In Equ.(2.28), an approximation has been used for the small angle, which is almost always valid in our measurements. Equ.(2.25) shows that, to obtain the spectrum of $\tilde{\varepsilon}_{xy}$, the spectrum of $\tilde{\varepsilon}_{xx}$ and the measurement of $\tilde{n}_+ - \tilde{n}_-$ are both required. From the previous assumption of $\tilde{\varepsilon}_{xx} \gg \tilde{\varepsilon}_{xy}$, we could write that $\tilde{\varepsilon}_{xx} = (n + ik)^2$ which is independent of the magnetisation.

The value of the off-diagonal constant is:

$$\tilde{\varepsilon}_{xy} = (\tilde{n}_+ - \tilde{n}_-)(n + ik) \quad \text{..... (2.29)}$$

Which may be referring in terms relates to the measured FR and MCD effects:

$$\varepsilon'_{xy} = \frac{2c}{\omega l_0}(n\theta_F - k\eta_F) \quad \text{..... (2.30)}$$

$$\varepsilon''_{xy} = \frac{2c}{\omega l_0}(k\theta_F - n\eta_F) \quad \text{..... (2.31)}$$

In the case of a very small overall absorption when, k ≪ n, the real and imaginary part of $\tilde{\varepsilon}_{xy}$ simply related to the FR and MCD, respectively, by [9, 17], where the two following equations used in this thesis:

$$\varepsilon'_{xy} \approx \frac{2c}{\omega l_0} n\theta_F \quad \text{..... (2.32)}$$

$$\varepsilon''_{xy} \approx \frac{2c}{\omega l_0} n\eta_F \quad \text{..... (2.33)}$$

Considering the change in phase and amplitude for RCP and LCP light reflected components to obtain the expressions for the dielectric tensor and the Kerr angles. This leads to give a clear explanation for the difference between the Kerr and Faraday effects [17]. The FR and MCD are given by;

$$\theta_F = Re\left[\frac{\omega l_o}{2c}\frac{\tilde{\varepsilon}_{xy}}{\sqrt{\tilde{\varepsilon}_{xx}}}\right] \quad \text{..... (2.34)}$$

$$\eta_F = tan\left[\text{Im}\left[\frac{\omega l_o}{2c}\frac{\tilde{\varepsilon}_{xy}}{\sqrt{\tilde{\varepsilon}_{xx}}}\right]\right] \quad \text{..... (2.35)}$$

2.4.2 Classical and Quantum Theories of Absorption

When a light pass through a material with a large number of atoms and small inter atomic separation, the force of the electric field intensity for the incident light, $\vec{E}(t)$, could make each atom under this force to oscillate, e.g. in the z-direction. We consider a classical oscillator of single electron charge q_e , and mass m_e, with natural frequency ω_o , driven by an electric field $\vec{E}(t)$ is given by:

$$\vec{F}_E = q_e\vec{E}(t) = e_z q_e E_o e^{i\omega t} \quad \text{..... (2.36)}$$

where, q_e is the electron dipole moment along z-direction. The equation of motion from Newton's second law is:

$$q_e E_o e^{i\omega t} = m_e \frac{d^2z}{dt^2} - m_e\gamma\frac{dz}{dt} + m_e\omega_o^2 z \quad \text{..... (2.37)}$$

then solution for (2.37) will be either:

$$z(t) = \frac{q_e/m_e}{\omega_0^2-\omega^2+i\gamma\omega}\, E_o e^{i\omega t} \quad \text{..... (2.38)}$$

Equation (2.38) represents the displacement between the electron (-) and the nucleus (+). Where ω_o, is the resonant frequency for the vibration without an external force effect. Now, assume a density of dipole moments, *P*, which is the electric polarization for *N* electrons per unit volume is give by,

$$P = q_e z N \quad \text{..... (2.39)}$$

Hence:

$$P = \frac{q_e^2 NE/m_e}{\omega_0^2-\omega^2+i\gamma\omega} \quad \text{..... (2.40)}$$

Now to describe *n* as a function of ω, we use the dispersion equation, by using the fact that $\tilde{n}^2 = \tilde{\varepsilon}_{xx}$,

$$\tilde{\varepsilon}_{xx} = 1 + \frac{P(t)}{\varepsilon_0 E(t)} = 1 + \frac{q_e^2 N/m_e}{\varepsilon_0(\omega_0^2-\omega^2+i\gamma\omega)} = \tilde{n}^2 \quad \text{..... (2.41)}$$

The above classical expression is used to obtain the quantum mechanical result, by supposing that there are N molecules per unit volume, and each molecule with f_i oscillators, having natural frequencies, ω_{oj}, and j = 1,2,3,…. ., [6, 9]. Therefore

$$\tilde{\varepsilon}_{xx} = 1 + \frac{Nq_e^2}{\varepsilon_0 m_e} \sum_j \left(\frac{f_j}{\omega_{0j}^2 - \omega^2 + i\gamma_j \omega} \right) \qquad \text{…….……..……} \quad (2.42)$$

Similarly, if we consider transitions where the orbital angular momentum changes by ±1, were *i*=0, then we get; [9].

$$\tilde{\varepsilon}_{xy} = \frac{Nq_e^2}{2\varepsilon_0 m_e} \left[\sum_j \frac{f_{j+}}{\omega_{0j+}^2 - \omega^2 + i\gamma_{ij}\omega} - \sum_j \frac{f_{j-}}{\omega_{0j-}^2 - \omega^2 + i\gamma_{ij}\omega} \right] \qquad \text{……..……..……} \quad (2.43)$$

Where $f_{j\pm}$ are the oscillator strengths for transitions caused by RCP and LCP light.

2.5 References

[1] J. Coey, *Magnetism and Magnetic Materials*: first edition ed. (Cambridge University press, 2010).

[2] B. Cullity and C. Graham, *Introduction to Magnetic Materials,* : second edition ed. (IEEE PRESS, 2009).

[3] S. Blundell, *Magnetism in Condensed Matter,*: second edition ed. (Oxford University press, 2003).

[4] C. Kittel., *Introduction to Solid State Physics,* : second edition ed. (Oxford University press, 2010).

[5] A. M. Fox, *Optical Properties of Solids,* : eighth edition ed. (John Wiley & Sons, 2005).

[6] E. Hecht, *Optics*, : 4th edition, Addison-Wesley (2002).

[7] A. Behan, "Characterisation of Doped ZnO Thin Films for Spintronic Applications, ," in Department of Physics and Astronomy 2008, The University of Sheffield.

[8] S.M.Thompson and Y.B.Xu, *Spintronic materials and technology. Series in materials science and engineering* . New York: Taylor & Francis. 423 p, (2007).

[9] F. J. Kahn, *et al.*, "Ultraviolet Magneto-Optical Properties Of Single-Crystal Orthoferrites, Garnets, And Other Ferric Oxide Compounds," *Physical Review*, vol. 186, pp. 891-&, (1969).

[10] J. C. Suits, "Faraday And Kerr Effects In Magnetic Compounds," *Ieee Transactions on Magnetics*, vol. MAG8, pp. 95-&, (1972).

[11] K. Sato, "Measurement Of Magneto-Optical Kerr Effect Using Piezo-Birefringent Modulator," *Japanese Journal of Applied Physics*, vol. 20, pp. 2403-2409,(1981).

[12] V. Antonov, *et al.*, *Electronic structure and magneto-optical properties of solids*, Dordrecht ; Boston: Kluwer Academic Publishers. xiii, p528,(2004)

[13] S. Kahl, *et al.*, "Optical transmission and Faraday rotation spectra of a bismuth iron garnet film (vol 94, pg 5688, 2003)," *Journal of Applied Physics*, vol. 96, pp. 1767-1767, (2004).

[14] X. Zhang, *et al.*, "Kerr-Effect And Dielectric Tensor Elements Of Magnetite (Fe3o4) Between 0.5 And 4.3 Ev," *Solid State Communications*, vol. 39, pp. 189-192, (1981).

[15] G. Q. Di and S. Uchiyama, "Optical and magneto-optical properties of MnBi film," *Physical Review B*, vol. 53, pp. 3327-3335, (1996).

[16] A. Schlegel, *et al.*, "Optical-Properties Of Magnetite (FE3O4)," *Journal of Physics C-Solid State Physics*, vol. 12, pp. 1157-1164, (1979).

[17] W. Reim and J. Schoenes, *Handbook of ferromagnetic materials*, : edited by E. P. Wohlfarth, K. H. J. Buschow (North-Holland, Amsterdam (1990).

Chapter 3

Experimental Techniques

3.1 Introduction

The following chapter will describe the sample preparation, the experimental technique and characterisation utilized in this work to analyze the data. The procedure for preparing the films is explained first; the majority of the samples used in this work were grown in University of Sheffield, and a few films were obtained from our collaborators in different groups, which will be mentioned throughout the thesis. Then this is followed by a explanation of the measurement methods of the thickness, and finally describes the optical and magneto optical procedure. Also, it includes an explanation of the magnetic measurements that were performed to obtain the magnetic properties for the samples such as; the hysteresis loops, and the field cooled (FC) and zero field cooled (ZFC).

3.2 Target Fabrication:

The desired amount of each target component is weighed out on an electrical balance followed by a standard solid-state reaction route. The stoichiometric weighted

quantities of powders were ground in a mortar and pestle three times for around (20-30) minutes each, in order to mix all the components. Then, the resulting mixture was fired in air for 12 hours (or more if required) at different temperatures, for instance, 400^{o}C, 600^{o}C, and 900^{o}C in a furnace (temperatures were changed when needed). The high-temperature sintering and the grinding repetition procedure are required to form the desired oxide compound and to reduce the impurity phases of any un-reacted powders.

The final powders were compressed by a hydraulic press in a vacuum at a pressure of 25000 kPa to form a cylindrical pellet with 25 mm diameter and about 5 mm thickness. Finally, the target was annealed in air at ~ (900-1150)^{o}C for up to 15 hours in order to get a smooth surface of the target. The target preparation steps, sintering, temperatures and time changes according to the material, which will be explained in later chapters when required. All the materials and tools used to prepare the target were cleaned regularly to avoid any contamination.

All of the prepared targets were placed on holders by a sticker, in order to be used in the laser ablation chamber to make the films. Thus, up to four days were required to prepare one target, which could change depending on the characteristics of the powders used. This method was found to be the best to prepare targets for pulsed laser deposition technique (PLD).

A cylinder of carbon was used to prepare a graphite target. The cylinder was chopped in the workshop to a small cylindrical pellet of 25 mm diameter and about 5 mm thickness and then located on the holder using a sticker. More details are given later in section 4.6.1.1.

3.3 Pulsed Laser Deposition System (PLD)

3.3.1 Introduction

Pulsed Laser Deposition is among the simplest techniques [1-3], which are used to produce thin films and multilayers. The other widespread methods are sputtering [4] and molecular-beam epitaxy (MBE) [5-7]. In comparison with other techniques, PLD has a number of good features, such as [1-3, 8-9]:

- The establishment costs are not very expensive comparing to sputtering and MBE.

- There is flexibility to grow highly pure multilayer thin films in a vacuum and in different ambient gases at different pressure.

- There is a strikingly high similarity in stoichiometric between the target and deposited films, thus enabling high-quality films to be grown.

- The laser source system is independent of the deposition chamber for the PLD comparing with other techniques. This feature allows the possibility of growing multilayer films easily by controlling the target movement in and out of the beam's focal point.

In spite of all these advantages for PLD there are also some negative points of this technique. "Splashing" is considered one of the major disadvantages that affect the uniformity of thin film, because of fast vaporisation which occurs around the target′ s

liquid layer formed by the laser power. Another drawback for PLD is the degradation of the target with the continuous use by the PLD for long deposition times, which leads to a reduction of the film quality, due to random particulates coming off the target and becoming incorporated in the film [1-3].

3.3.2 Pulsed Laser Deposition Set-up and Procedure

Figure (3-1) [10] shows the three main parts of the PLD system: the laser, optical arrangement and deposition chamber [1-3]. The laser employed in the experiment was an excimer XeCl laser model (Lambda Physik LEXTRA 200) possesses with an operating wavelength of 308 nm. The optical pulse length for the laser is very short at about 28 ns and it operates at 10 Hz pulse frequency with pulse energy up to 400mJ.

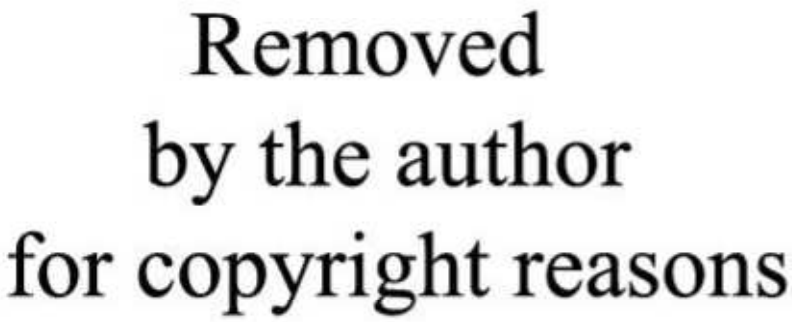

Figure (3-1): Schematic diagram of the pulsed laser deposition chamber. Adopted from [10]

The quartz lens which is a part of the optical arrangement for the PLD was located at the same horizontal line with the laser beam, and parallel to the front optical window glass of the chamber. The role of this lens is to focus the laser beam to be incident on the rotating target at 45^{o}, and to produce a spot size on the target surface of area roughly about 3 mm^{2}.

The deposition chamber is a high vacuum stainless-steel compartment, containing the target holder, the substrate holder and the pressure gauge unit. The target holder and substrate holder face each other at a fixed distance (of about 5 centimetres). The target holder is rotated at a speed of 60 rpm by an electric motor. The main advantage of this rotation is that it prevents the creation of a hole on the target from continuous ablation by the laser and, therefore, decreases the formation of splashing onto the substrate.

After clamping the target inside the chamber, the substrate which is usually sapphire (or glass) is cleaned ultrasonically in acetone, and then clamped onto the holder with two small clamps. This is a positive point because it provides two free blank areas of the substrate to consider as a reference when recording the films thickness using Dektak, more details will be shown later. The substrate holder as shown in Figure (3-2) is wired to two electric heater bars which are connected to a power supply in order to heat the substrate to the required temperature. During the deposition the substrate temperature is monitored by using a Chrome-Alumel thermocouple, where one side of the thermocouple is attached to the film holder, and the other junction is immersed in an ice-bath.

The chamber is then locked and pumped-down to the desired pressure. By using the turbo-molecular pump (TMP) synchronously with the rotary pump the chamber can be evacuated to the minimum base pressure of 10^{-5} Torr.

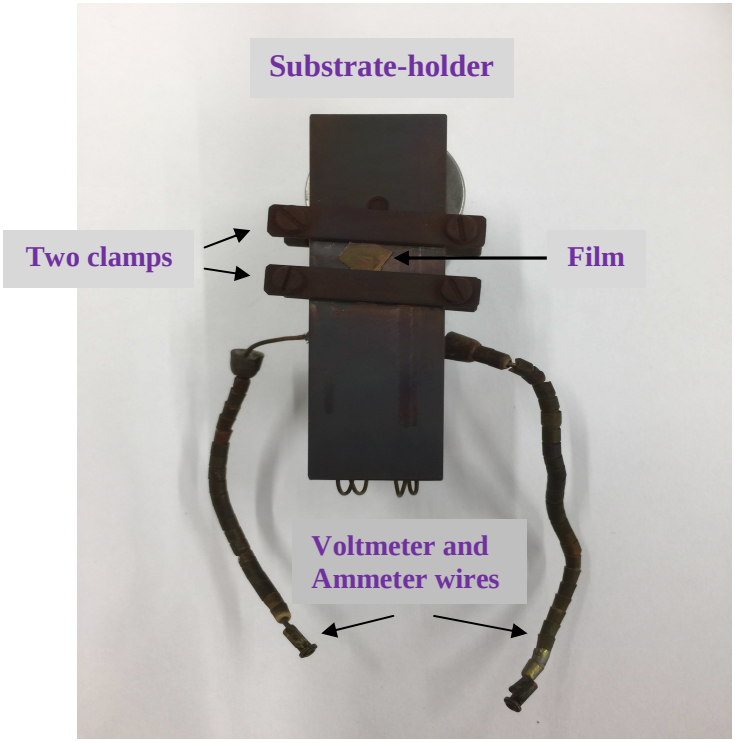

Figure (3-2): A photo of the substrate holder with a deposited film placed between the clamps.

In addition, there are three extra valves: a gas valve, a roughing pump valve and gate valve, used to control the changing of the pressure from the base pressure to an accuracy of a hundred of a mTorr. Once the required conditions are attained, the laser is switched on and the deposition of the atoms on the substrate (for different deposition time) is performed.

The chosen parameters; the substrate temperature, the laser energy and plume quality, and the chamber pressure were all monitored throughout the deposition process. The laser beam incident at the rotating target will transfer energy to the target and evaporate it, producing a plume at the target surface. The plume includes atoms, molecules, electrons, ions and clusters, which depends on the quality of the target and the chamber pressure. Clearly, the interaction between the laser, target and plume will affect the film deposition in a positive way. The film thickness depends on the deposition time, and the plume quality, finally, after the deposition process is finished, the film can be allowed to cool down slowly at RT for period of time.

The PLD technique is suitable for complex materials growth, as will be mention later in the following chapters. It reflects the target stoichiometric in the film very well. It is also very convenient for oxides as it may be used with variable oxygen pressure. Some studies have reported differences between PLD and MBE especially at high intensity, while at low intensity; PLD resembles MBE [11-12], as will be explained in chapter 5.

There are two main differences between PLD and MBE: in PLD the atoms, or ions, arrive at the substrate with a considerable kinetic energy [11-12]; whereas in MBE the atoms have a much smaller kinetic energy which is characteristic of the temperature needed for thermal evaporation, the second difference is that atoms arrive in pulses in PLD whereas they arrive as a continuous stream in MBE. Films made by standard PLD are usually textured and may have inclusions of target material known as boulders.

Single layer epitaxial films can be grown by a laser using a modification known as laser assisted molecular beam eptaxy LAMBE in which the length of time between laser

pulses is greatly increased, by a factor of 10 or 100. In this case the surface quality and morphology for films prepared by LAMBE may be better than MBE. In addition, Tan et al. [12-13] showed that at low substrate temperatures the properties of films deposited by PLD are similar to those deposited by MBE. While by decreasing the pulse duration for the PLD, an increase of the island densities has been noticed, at high temperatures [12-13] . Polar ZnO films can only be grown by MBE or by LAMBE and not by the standard PLD; more details is given in chapter 5.

3.4 Dektak Surface Profiler- Measuring Film Thickness

A Dektak Surface Profiler is an instrument used to measure the texture profiler of the sample surface vertically. It measures the thickness of samples ranging from 40nm to 500nm, by the mechanical lever (the moving part), which is connected to the optical lever controlled by a computer.

A sensitive diamond-tipped stylus on the Dektak, as shown in Figure (3-3) is moved vertically along the film surface, from the blank area at the corners of the substrate, which represent the clamped area of the sample holder, to the area of the deposited film. The stylus pressing force onto the sample could be adjusted. After adjusting the stylus height to the desired work circular stage, which is an important part of the Dektak moves to the front and back, a vertical displacement of the stylus directed from the blank area to the middle of the film is recorded by a varying electrical inductance. The resulted inductance data is recorded, and later switched into a height and plotted by

Dektak software as a function of horizontal distance. The thickness value of the film was obtained by taking the average of a number of recorded measurements.

The thickness value measured by Dektak may vary from an area to another on the film surface, due to several reasons related with films grown by PLD. The substrate type, the quality of the laser plume and the chamber pressure, all these parameters affects on the surface uniformity of the film.

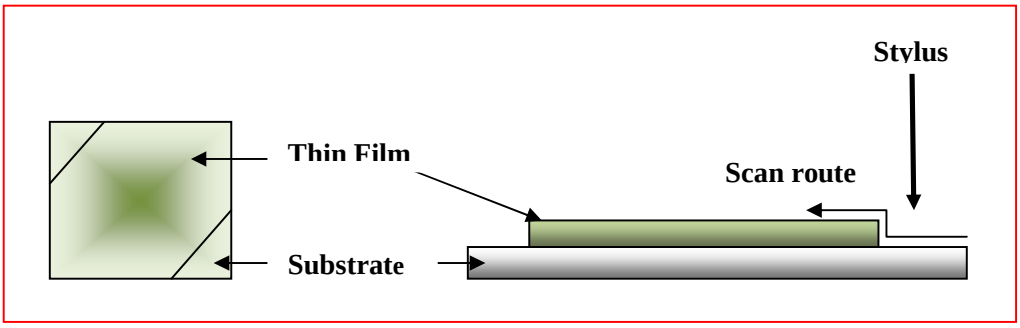

Figure (3-3): A side view of the Scan route for the Dektak thickness measurements for the films and deposited film on a substrate.

3.4 Optical Measurements

A number of optical phenomena, including transmission, reflection, absorption and scattering, are observed as a result of light propagation through the film [14]. In this system, the absorption spectrum was determined by direct measurements of the transmission and reflection spectra as a function of energy at room temperature, in order to provided information about the electronic structures and essential optical properties of the sample. A tungsten halogen lamp generates at 250 watts was used as a light source in order to measure over a wide spectral range from 1.7 eV to 4.5 eV. The position for the photomultiplier detector (PMT) in the system set-up can be changed during the experiment to detect the light for the transmission and reflection, as required.

Monochromatic light was produced when the light passed through a (Spectro-275) spectrometer. A filter is used to split the light into two beams. The first beam (called a reference) passes through an optical chopper with a given frequency which is then recorded by the PMT. Whereas the second beam (called the sample beam) is also chopped by the chopper with a given frequency too, then goes to the sample and then is detected by the second PMT detector after being reflected from, or transmitted through, the samples. The detector's job is to convert the intensity of light to an electrical signal and then amplify the signal by the conditioning unit and split it into the AC and DC components. The lock-in amplifiers were used to amplify and record the AC signals, and to measure the intensities of the incident I_o, the reference I_r the transmitted I_1 and the reflected I_2 beams. In addition, the two lock-in amplifiers also record the transmitted or reflected beam and the reference beam.

The optical phenomena can be calculated by their parameters. The transmission is quantified by the transmission coefficient (T), which is defined as the ratio of the transmitted light intensity to the total incident light intensity [14-15]. Similarly, the reflectivity or reflection coefficient (R) indicates the ratio of the power for the reflected light to the power of the incident light [14-15]. If there is no scattering or absorption occurs in the system, these two coefficients will equal to the unity [14-15]:

$$T+R=1 \qquad \text{.....} \quad (3.1)$$

When the light passes through a sample of thickness *l* and is absorbed, this is quantified by the absorption coefficient α. This is defined as the fraction of intensity that has been absorbed by a unit length of the film. Therefore, the integration of the intensity along the film thickness gives us Beer′s Law

$$I(I) = I_o e^{-\alpha l} \qquad \text{…….....…..} \quad (3.2)$$

I_o here refers to the intensity of the incident light. Assuming that the reflectivity of the substrate is negligible and only the reflectivity of the deposited film is taken into consideration, then from equation (3.1) the transmission will be:

$$T = (1-R)^2 e^{-\alpha l} \qquad \text{…….....…..} \quad (3.3)$$

By derivation using Beer′s Law, the absorption coefficient α, can be calculated using the following equation, in order to identify the band gap

$$\alpha = \frac{1}{l}\ln\left(\frac{(1-R)^2}{T}\right) \qquad \text{…….....…..} (3.4)$$

The band gap energy for the direct interband can be determined from the absorption coefficent by the following equation, [16-18]

$$\alpha h\upsilon = A(h\upsilon - E_g)^{1/2} \qquad \text{…….....…..} (3.5)$$

where $h\upsilon$ refers to photon energy, E_g to the band gap energy of the material and A is a constant for a given sample. The band gap can be obtained from the intersection on the energy axis by plotting α^2 as a function of $h\upsilon$ as shown in Figure (3-4):

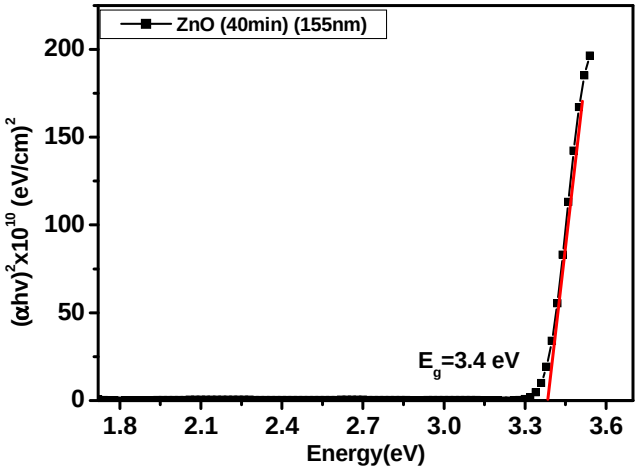

Figure (3-4): Plot of α^2 the absorption coefficient as a function of energy for pure ZnO, were E_g= 3.4 eV.

3.5 Set-up for Magneto-Optical Measurement

Magneto-Optics is the technique that used to investigate the modifications which occur to the light when it is passed through a magnetic crystal. The system set-up used is based on Sato methods [19] that enables magneto-optical spectra to be obtained using a Piezo-Birefringent modulator. Our magneto-optic system setup was put together by Dr Neal of the University of Sheffield, with Prof. Kucera from Charles University, our MO setup is shown in Figure (3.5) [20]. This system allows simultaneous determination of the two MO parameters, MCD and Faraday rotation θ and is the main factor that makes this approach used widely. An important feature of this technique is the ability to perform an accurate measurement over a wide range of wavelengths. Also this method provides a 12 nm resolution and a sensitivity of 0.0020 at wavelength of 500 nm.

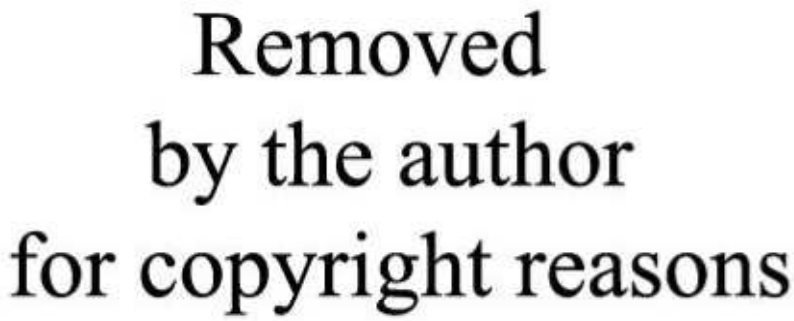

Figure (3.5): Schematic diagram of MO setup for measurement in either Faraday or Kerr geometry. Adapted from [20].

The magneto-optics set-up geometry can be switched during the measurements depending on the samples used. If the sample is highly absorbing and not transparent (opaque), Kerr geometry is more suitable for the measurement. The Faraday geometry is the most appropriate for the use where the sample is transparent. This set-up can be achieved by changing the position of the photoelastic modulator (PEM), photomultiplier (PMT), and analyser to detect the reflected light for Kerr geometry or the transmitted light for Faraday geometry. The set-up uses either a tungsten halogen lamp with a power of 250 watt that covers a wide spectral range between 0.6 - 3.8 eV, or a Xenon lamp with a power of 150 watt to cover a spectral range between 1.5 - 4.5 eV. Both lamps are set in a metal container aligned at the right angles to the set-up.

The aligned light from the source then passes through a spectrometer (Spectro-275) to create a monochromatic light. The spectrometer has three different gratings blazed for different wavelengths which can be selected according to the wavelength of the required light. Meanwhile a band pass filter was used to remove the unfavourable wavelengths from higher order reflections. In order to produce a plane polarized light, therefore, the light is passed through a Glan-Taylor UV prism polarizer positioned 45^{o} to the analyser and 90^{o} to the optical axis, before focused onto the sample. The polariser angle is controlled by using a motor and a PC, where the position of the polariser needs to be optimised whenever the optical alignment is changed.

After cleaning the sample carefully with acetone or ethanol, the sample is mounted on a metallic disc with aperture of about 2-3 mm diameter. The sample holder is held vertically between the two poles of the electromagnet. The maximum magnetic field

obtainable from the poles is 1.8 Tesla for room temperature and 0.5 Tesla for low temperature due to the different gap size. The field is applied perpendicularly to the sample and parallel to the direction of incidence.

A series of mirror and lenses were used to focus the light beam to a size similar to that of the holder aperture. A regular optimisation for these mirrors is required for the purpose of maintaining the maximum amount of the polarized light passing through the sample, and ensures that the light is not scattered.

A photo-elastic modulator with a frequency of 50 kHz (PEM) purchased from Hinds instrument is used (to produce a signal proportional to the rotation θ and ellipticity η when the light passes through it). The PEM works on the photoelastic effect principle, where a sample under mechanical stress exhibits a birefringence that is proportional to the resulting strain. The PEM is consists of a birefringent crystal placed on the top of a piezo-vibrator that is used to modulate the frequency, f [20-22]. A periodic retardation in the phase of the light will occurs parallel to the vibration direction, which will causes a change in the birefringent of the crystal. Therefore the PEM will modulate the polarisation of the light with a fixed frequency. The birefringent crystal is set to a quarter of the wavelength and also the angle between the vibration direction of the crystal and the first polarizer is set at 45^0 [20-22].

The light then passes through an analyser to be analysed and focused on the photomultiplier tube detector (PMT). The light intensity is un modulates if there are no magneto-optics effects, however the light intensity will be modulated with a frequency

of *f* or 2*f*, if the sample exhibits any M-O effect, due to the effect of MCD or rotation respectively [19, 23].

The main function for this PMT detector is to convert the intensity of the light to an electrical signal and then the signal is amplified by feeding it to a Hinds signal conditioning unit and splitting it into AC and DC components. In order to record the DC component, a Keithley voltmeter was used, which can be controlled to conserve a constant sensitivity. Meanwhile two signal recovery lock-in amplifiers were used to record the AC voltage. In this study, the voltmeter and lock-in amplifiers (one and two) are used to measure the intensities I_0 (DC intensity), I_f (MCD intensity) and I_{2f} (rotation intensity) respectively.

The values of the MCD and Faraday rotation can be obtained by measuring three intensities, I_0, I_f and I_{2f}, as explained by Sato [19], and these are given in the following equations:

$$I_1(0) = I_0 T\{1 + J_0(\delta_0)\sin(\Delta\theta + 2\phi)\} \quad \text{..... (3.6)}$$

$$I_2(f) = I_0 \Delta T J_1(\delta_0) \quad \text{..... (3.7)}$$

$$I_3(2f) = 2I_0 T J_2(\delta_0)\sin(\Delta\theta + 2\phi) \quad \text{..... (3.8)}$$

$$\Delta T = (t_+^2 - t_-^2) \quad \text{..... (3.9)}$$

$$T = \frac{1}{2}(t_+^2 + t_-^2) \quad \text{..... (3.10)}$$

where, ϕ is the analyser angle always set to zero in our set-up and $\Delta\theta$ the difference in LCP and RCP rotation, I_0 is an intensity constant, δ_0 is the amplitude of the retardation, and $t_{\pm}$ are the Fresnel coefficients that represent the RCP and LCP transmitted light. The J_0, J_1 and J_2 terms are the (zero, first and second) order Bessel functions which are proportional to the light intensity, MCD and Faraday rotation respectively. This function is used to control the retardation to be set by the PEM, were it is set to 0.383 [24], were J_1 and J_2 are near their maximums, while J_0 is around zero. The purpose of setting the retardation to 0.383, is achieve the maximum sensitivity for the MO, and while being insensitive to fluctuations in light intensity.

In addition, Sato stated the formulas which are used to get the values of Faraday rotation θ_F and Faraday ellipticity η_F from the measurement of the I_0, I_{1f} and I_{2f} intensities, are given by [19]:

$$\theta_F = -\frac{1}{2}\Delta\theta \qquad \text{…….....} \quad (3.11)$$

$$\eta_F = \frac{1}{4}(\Delta T/T) \qquad \text{…….....} \quad (3.12)$$

Therefore, by analysing the ratios of (I_2/I_1) and (I_3/I_1) that can be linked to the MCD and Faraday rotation respectively, θ_F and η_F can be calculated by the following equations :

$$\frac{I_2(f)}{I_1(0)} = A\frac{J_1(\delta_0)\Delta T/T}{1+J_0(\delta_0)\sin(\Delta\theta)} = AJ_1(\delta_0)\frac{\Delta T}{T} \approx \eta_F \quad \text{..... (3.13)}$$

$$\frac{I_3(2f)}{I_1(0)} = B\frac{2J_2(\delta_0)\sin(\Delta\theta)}{1+J_0(\delta_0)\sin(\Delta\theta)} = BJ_2(\delta_0)2\Delta\theta \approx \theta_F \quad \text{..... (3.14)}$$

The values obtained by the previous formulas were in arbitrary units, which can be converting into real units (degrees) by the analyser. This is done by rotating the polariser angle to reach a minimum output for $I_3(2f)$. Then the analyser is rotated from ($+2^0$ to -2^0) by steps of 1.0^o, associated with recording the value of ($I_3(2f)/I_1(0)$) at each angle. So, by recording the different values at each analyser angle the calibration factor can be determined.

The measurements for this system are controlled automatically via the PC using Labview software. Furthermore the (MCD) is the difference in intensity between the left and right circularly polarised light at a frequency ω. MCD is a useful technique to determine the nature of a magnetic state and properties of a material, since it is only dependent on the transitions occurring on the measuring frequency ω.

During the MCD measurements, we have faced a major issue with this experiment. The first problem was related to the Labview program that we use to control the measurement; therefore, I have put an effort to learn at least the basics about this program, by taking few courses, to enable me to specify the source of the problem. Then after, I found that the issue was caused by a fault in the PEM. Therefore, we had to investigate the source of the problem with the PEM with the manufacturing company. I have played a major role in the group to incorporate the new PEM into the Labview program and start running the MCD again.

3.6 Measuring Magnetisation-SQUID Magnetometer

3.6.1 SQUID Fundamentals

A superconducting quantum interface device magnetometer, SQUID is one of the most sensitive magnetic flux sensors, which is used for doing magnetisation measurements. A number of applications are associated with the SQUID, including material property measurements and bio-magnetism, which is due to it is excessive ability to detect small magnetic fields; more details on the general use of a SQUID can be found in refs [25-27].

All the measurements in our laboratory were obtained by a radio frequency (RF) SQUID magnetometer model MPMS-5 manufactured by Quantum Design, as shown in Figure (3.6) [28]. The temperature range of SQUID used is from about 5K to 300K, and the magnetic field could be set from 10^{-17} T to about 5T. The SQUID system is consists of an Nb-superconducting material ring and an RF circuit which are coupled inductively to the field sensing coil using superconducting transformers that are maintained at liquid helium temperatures. The RF circuit is supplied by a constant current RF oscillator, which has a 20 MHz resonance frequency.

If the ring is not superconducting (its normal state), an applied magnetic field will permeate the material in the ring through it. The field will be expelled from the material when the ring is superconducting [26-29]. Therefore, due to the induced

surface current, the superconducting ring will be able to trap different levels of magnetic flux after a magnetic field is removed.

The trapped magnetic flux will induce a current in the superconducting ring that will exist for an indeterminate time. Furthermore, this trapped flux is quantized in multiples of (Φ_0=h/2e), and is equal to 2 x10^{-15} Tm^2.

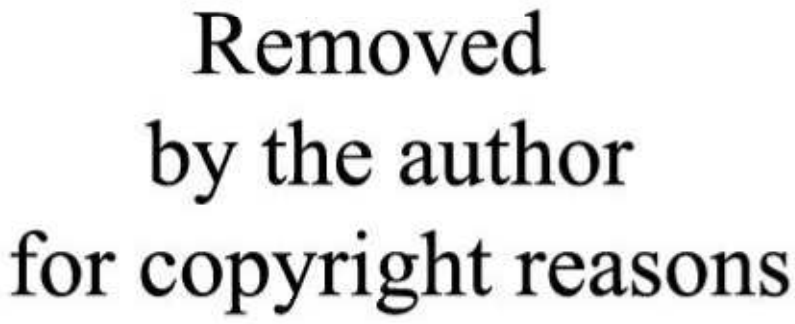

Figure (3.6): The SQUID system components, adapted from [28].

1. Sample Rod 2. Sample Rotator 3. Sample Transport 4. Probe Assembly 5. Helium Level Sensor 6. Superconducting Solenoid 7. Flow Impedance 8. SQUID Capsule with Magnetic Shield 9. Superconducting Pickup Coil 10. Dewar Isolation Cabinet 11. Dewar 12. HP ThinkJet Printer 13. Magnet Power Supply 14. Model 1802 Temperature Controller 15. Console Cabinet 16. Power Distribution Unit 17. Model 1822 MPMS Controller 18. Gas Magnet Control Unit 19. HP Vectra Computer 20. Monitor.

There is a critical super current value for the ring, beyond which the induced current must not be exceeded. As it is known that measuring a change voltage is easier than measuring a change of the magnetic field, the SQUID has been designed in a way that measures the change in the voltage. Furthermore, the flux changes that occur in the superconducting ring cause damping of the resonance of the RF circuit, which then can be amplified and recorded by the controlling system. The variation of the flux is converted to a magnetisation using a least-squares fitting program [27-29].

3.6.2 SQUID operation

We address the steps which have been used to measure the samples using the SQUID. A typical sample dimensions to be measured in the SQUID is 5 x 5 x 0.3 mm^3. First the sample needs to be cleaned before putting it in the SQUID chamber. The sample is mounted either by wedging it into the middle of the straw or putting it in a gelatine capsule and stitching the capsule into a long plastic straw and fixes the position to the centre. After that, the straw is attached to the sample-holder rod, which is a brass end of a stainless steel rod approximately 1.5 m in length.

The rod is then introduced partially into the SQUID through an access port on the top of the SQUID system. An air-lock is used to ensure a clean environment inside the SQUID system by preventing the contamination of the atmospheric gases. This is followed by venting and purging the upper part of the chamber before opening the air-lock and inserting the rod into the SQUID completely. Once in the system, the position

of the sample needs to be matched with the centre of the field-sensing coils, so a scan over a length of 8 cm is run to determine the location of the sample that can be centered either manually or automatically.

In order to achieve an accurate position for the sample in the centre, the scan is repeated using a shorter scan length of 2 cm. Then, the appropriate measurement sequence, temperature and the magnetic field can be selected and set. The helium level in the SQUID should be over 50% if we set a magnetic field of 1T. It is important to know that the measurements have not been run until both the temperature and magnetic fields are stable. Finally, the scan sequence measurement can be started.

During the scan, the sample is stepped through a 2^{nd} order gradiometer field-sensing coils, which consists of two sets of coils wired oppositely to each other, to reduce any external noise and give more accurate measurements. The sample then starts to generate a field due to it is magnetic moment, which then induces a super-current in the coils and produces a magnetic flux through the ring. Therefore, a record of these measurements as a function of field provides us with data for the magnetisation of the sample.

There are several measurement programs that have been used by the SQUID in our lab. One of the types of measurement is hysteresis loops of the magnetisation with a maximum magnetic induction up to 5T, where 1T is used normally for our measurements, a at fixed temperatures ranging from 5K to 400K. The magnetic field (H) can be applied either parallel or perpendicular to the plane of the film.

The remanence magnetization (Mr), coercive field (Hc) and magnetization saturation (Ms) are obtained from the hysteresis loops. The magnetization (M) of the sample is measured as a function of the external field. As mentioned previously, a super-current will be generate in the coils from the magnetic field produced by the sample, causing it to induce a magnetic flux through the superconducting ring. The result will consist of a contribution from both the sample and the substrate. There are three main contributions which can be noticed; the diamagnetic contribution from the substrate, ferromagnetic contribution from the film and also a paramagnetic behaviour of the film which is possibly due to a small fraction of unreacted components in the film.

To get a correct result for the hysteresis loop, all other contributions need to be subtracted off. So, the separation of the ferromagnetic behaviour from others can be achieved by calculating the slope of the linear line for both high-field regions then subtracting it from each point. The raw SQUID data for 5% Co doped ZnO film on a sapphire substrate, Figure (3.7a), shows two clear contributions. There is linear dependency in high field due to the diamagnetic contribution, and in low field, there is a saturating ferromagnetic contribution from the film. Figure (3.7b), shows the separate ferromagnetic contribution obtained after subtracting off the linear component.

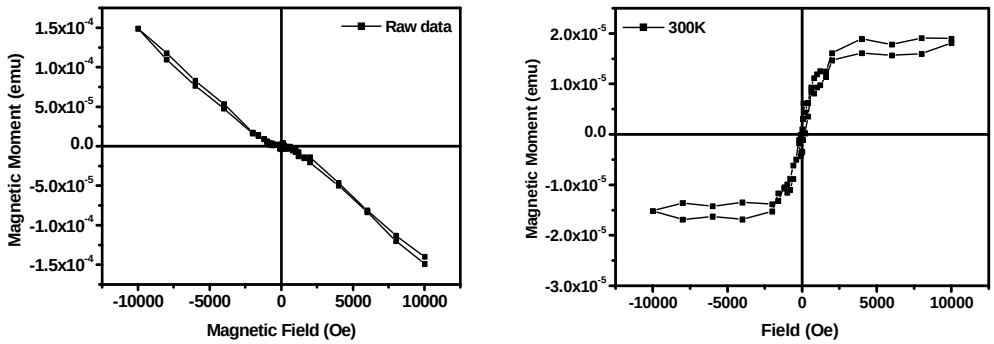

Figure (3.7): The room temperature SQUID data for 5% Co doped ZnO (a) raw data, (b) after subtraction of linear contribution.

In addition, zero field-cooled (ZFC) and field-cooled (FC) measurements are another type of measurement used extensively in this thesis. The magnetisation is measured, as a function of temperature (T) for a sample both ZFC and FC conditions in order to show the dependence on the magnetic field history. As it is done in low magnetic field, typically 100Oe, the ZFC data gives the temperature dependence of low field susceptibility. It also provides information about the irreversibility of the system within the considered temperature range. ZFC/FC measurements can be run in the SQUID for a range of thin films of various compositions and also for bulk samples.

A ZFC sequence is done by setting the magnetic field is set to zero when the sample is cooled down to usually 5K. Then after temperature stabilisation is achieved, a small magnetic field of about 100 Oe is applied, and the sample magnetic moment is measured in increased temperature range from 5K up to 300K (warming-up).

In the FC sequence the magnetisation is measured when the sample is cooled down from 300K to 5K in the small field up to 100 Oe, and the magnetic moment is measured in a temperature range as the sample is warmed up to 300K.

A majority of the magnetic moments of particles remain along easy axis as temperature increases from 5K due to the local anisotropy. Above a specific temperature, there is sufficient thermal energy for the magnetic moments to reorient and a superparamagnetic behaviour occurs; where is called TB blocking temperature. The magnetisation for $T < T_B$ is depends on H and T as well as on history, while, the magnetisation is only depends on H and T for $T > T_B$, where it is in equilibrium [27-28]. If there are isolated clusters with anisotropy energy KV then the magnetisation of the clusters can reorient freely for $T > T_B$, where $K_B T_B \sim KV/25$. Thus, hysteresis occurs for $T < T_B$, this is seen by FC field cooled and ZFC magnetisation.

The history dependency is refer to that, the observed magnetic moment is depend on the magnetic field sequence and temperature changes that were responsible to obtain the desired condition for the sample where it was measured. A more specific type of behaviour for the history dependency is so-called the irreversibility (or hysteresis) behaviour. The importance of irreversibility in ferromagnets for example; is illustrated in the M(H) curve, where the shape will change except if saturation is obtained on the loop. Therefore a different M(H) curve will be record when a magnetic field below saturation is applied [27-28].

3.7 Sapphire Substrates

Sapphire, or Al_2O_3, is an anisotropic crystal that has a corundum structure; it has a density of 3.98 g/cm^3 and a lattice constant of 4.785Å. It is the best candidate as a substrate for the deposition of DMS materials, because the lattice constant matches between sapphire and most of the semiconductor materials. This close agreement between lattices constant reduces the strain problem causes by the interface between the substrate and the deposited material during the growth process. Sapphire is transparent from up to 6eV, which covers the band gap of all semiconductors, hence it is widely used as a substrate if optical measurements are required.

Sapphire substrates are either a single or double side polished. Thus, the transmission is different between these two types. There is much more scattering from a single side polished film so that sapphire substrates used for this work were double side polished. Figure (3.8) show the transmission spectra for our sapphire.

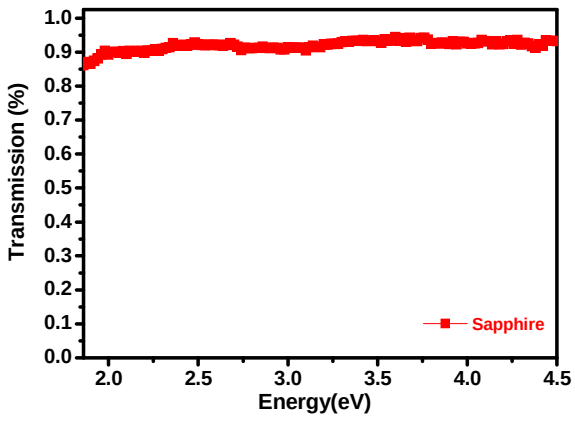

Figure (3.8): The optical transmission spectrum of a sapphire substrate measured at RT.

In the absence of the films and consider the thick sapphire alone, the free transmission, T_s is given by:

$$T_s = T^2(1 + R^2 + R^4 + \cdots) = \frac{T^2}{1-R^2} = \frac{(1-R)^2}{1-R^2} \quad \text{…….....} \quad (3.15)$$

Where T and R , the transmission and reflection coefficient respectively.

$$T + R = 1 \quad \text{…….....} \quad (3.16)$$

$$R = \left(\frac{s-1}{s+1}\right)^2 \quad \text{…….....} \quad (3.17)$$

where s is the substrate refractive index. Combining eqn.(3.16), eqn.(3.17) and eqn.(3.15) yields,

$$T_s = \frac{2s}{s^2+1} \quad \text{…….....} \quad (3.18)$$

The transmission spectrum shown in figure (3.8) is for a blank sapphire substrate measured as a function of energy in the range from 1.7 to 4.5 eV at RT, where the maximum transmission is about T= 0.89 compared with the theoretical values of T=0.86 from eqn (3.18) using the refractive index of sapphire of about 1.76, and the differences is due to a small amount of scattering, which is acceptable [30-31].

The MCD and the Faraday rotation of a blank sapphire substrate was measured as a function of photon energy range from 1.5 to 4 eV at RT in a field of 1.8T, as shown in Figure (3.9). The scattering of the MCD and FR at energies below 1.8 eV may be due

to the intensity fall-off for the xenon lamp that reduces the light sensitivity. The MCD and FR for the sapphire are larger than that of the thin film, and weakly dependent on temperature. Therefore, in order to obtain the spectrum of the MCD and FR for the deposited film on a sapphire substrate, the substrate contribution must be subtracted.

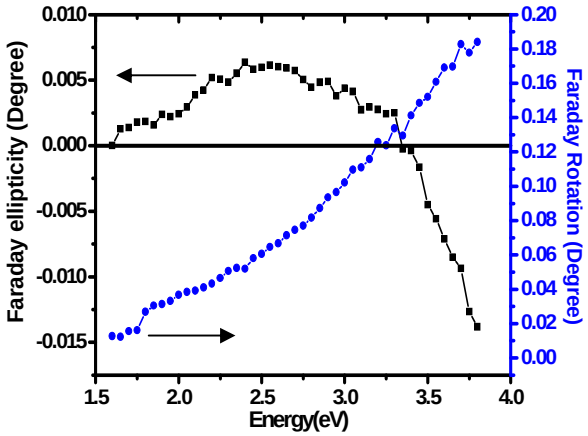

Figure (3.9): Faraday ellipticity and rotation of sapphire substrate in arbitrary unit at RT and 1.8T.

3.8 References

[1] M. N. R. Ashfold, *et al.*, "Pulsed laser ablation and deposition of thin films,," *Chemical Society Reviews, vol. 33, pp. 23-31, (2004).*

[2] H. U. Krebs, *et al.*, "Pulsed laser deposition (PLD) - A versatile thin film technique," *Advances in Solid State Physics 43*, vol. 43, pp. 505-517, (2003).

[3] D.B.Chrisey and G.K.Hubler, *Pulsed Laser Deposition of Thin Films*: (Wiley. Interscience, Canada,1994).

[4] B. Chapman, *Glow Discharge Processes: Sputtering and Plasma Etching*: (John Wiley & Sons, New York, 1980).

[5] B. R. Pamplin, *Molecular beam epitaxy* (Pergamon Press, New York, 1985).

[6] Minju Ying, *et al.*, "ZnO gap states investigated using magnetic circular dichroism,," *Journal of Physics D-Applied Physics, vol. 48, p. 255502, (2015).*

[7] Minju Ying, *et al.*, "Surface-polarity-dependent ferromagnetisminarsenic-implantedZnO films preparedbyMBE," *Materials Letters144, 12–14, (2015).*

[8] K. Yang and J. Dho, "Semiconductor-like and Metal-like Transport Properties of Doped ZnO Films Prepared by Using Pulsed Laser Deposition,," *Journal of the Korean Physical Society, vol. 55, pp. 188-192, (2009).*

[9] P. T. Murray and D. T. Peeler, "Pulsedlaser interactions with graphite,," *American Institute of Physics, AIP Conference Proceedings 288, 359 (1993).*

[10] M. S. Alqahtani, "Magnetic and Magneto-Optical Properties of Doped Oxides," in Department of Physics and Astronomy (2012), The University of Sheffield.

[11] P. M. Lam, *et al.*, "Monte Carlo simulation of pulsed laser deposition," *Physical Review B*, vol. 66, (2002).

[12] X. H. Xu, *et al.*, "A study of the optimization of parameters for pulsed laser deposition using Monte Carlo simulation," *Thin Solid Films*, vol. 515, pp. 2754-2759, (2006).

[13] X. Tan, *et al.*, "Dependence of morphology of pulsed-laser deposited coatings on temperature: a kinetic Monte Carlo simulation," *Surface & Coatings Technology*, vol. 197, pp. 288-293, (2005).

[14] A. M. Fox, *Optical Properties of Solids*,: eighth edition ed. (John Wiley & Sons, 2005).

[15] E. Hecht, *Optics*: 4th edition, (Addison-Wesley 2002).

[16] E. C. y. Díaz, *et al.*, " Electrical, structural and optical properties of ZnO thinfilms grown by pulsed laser deposition. ," *International Journal of Physical Sciences Vol. 6 (18), pp. 4382-4387, (2011).*

[17] J. Tauc, *Amorphous and liquid semiconductors* London, New York,: Plenum. ix, 441 p, (1974).

[18] T. J, "Optical properties and electronic structure of amorphous Ge and Si," *Materials Research Bulletin vol.3, 37-46, (1968).*

[19] K. Sato, "MEASUREMENT OF MAGNETO-OPTICAL KERR EFFECT USING PIEZO-BIREFRINGENT MODULATOR,," *Japanese Journal of Applied Physics, vol. 20, pp. 2403-2409,(1981).*

[20] A. Behan, "Characterisation of Doped ZnO Thin Films for Spintronic Applications,," *in Department of Physics and Astronomy (2008), The University of Sheffield.*

[21] K.W. Hipps and G. A. Crosby, "Applications of the photoelastic modulator to polarization spectroscopy," *J. Physical Chemistry, 83, 555, (1979).*

[22] K. H. M. Suzuki, *et al.*, "Direct measurement of magnetic circular dichroism and Kerr rotationspectra in vacuum ultraviolet using fourmirror polarizer," *[Review of Scientific Instruments]. 66, 1589, (1995).*

[23] M. Seth and T. Ziegler, "Magnetic Circular Dichroism Spectrum of Plastocyanin by Calculation," *Inorganic Chemistry, vol. 48, pp. 1793-+, (2009).*

[24] W. V. Drent and T. Suzuki, "Ultra-violet range magneto-optic study of FCC-Co and Co/Pt multilayers," *Journal of Magnetism and Magnetic Materials 175, 53, (1997).*

[25] J. Clarke and A. I. Braginski, *The SQUID handbook*: (Wiley-VCH, Weinheim, 2004).

[26] a. Gallop.J.C, and Petley.B.W, , "SQUIDs and their applications,," *IOP Science, vol. 9, pp417, (1976).*

[27] R. L. Fagaly, "Superconducting quantum interference device instruments and applications,," *Review of Scientific Instruments, vol. 77, 101101, (2006).*

[28] M. Mceifresh, "FUNDAMENTALS OF MAGNETISM AND MAGNETIC MEASUREMENTS FEATURING QUANTUM DESIGN'SMAGNETIC PROPERTY MEASUREMENT," " *ed. Quantum Design: Quantum Design, (1994).*

[29] J. Clarke, "PRINCIPLES AND APPLICATIONS OF SQUIDS,," *Proceedings of the Ieee, vol. 77, pp.1208-1223, (1989).*

[30] R. Reed, "1998; Available from: http://hypertextbook.com/facts/2007/GaryChang.shtml."

[31] G.R.S. Co, " 2011; Available from: http://www.generalruby.com/sapphire.html."

Chapter 4

Optical and Magneto-Optical Properties of Graphite and Graphene

4.1 Introduction

Much research has been conducted on carbon nanostructures. Figure (4-1) illustrates the last 20 years' worth of publications on carbon nanostructures. As can be seen from Figure (4-1), there has been a high number and a vast increase of the studies or pieces of research carried out on sp^2 carbon-based materials since 2008 [1].

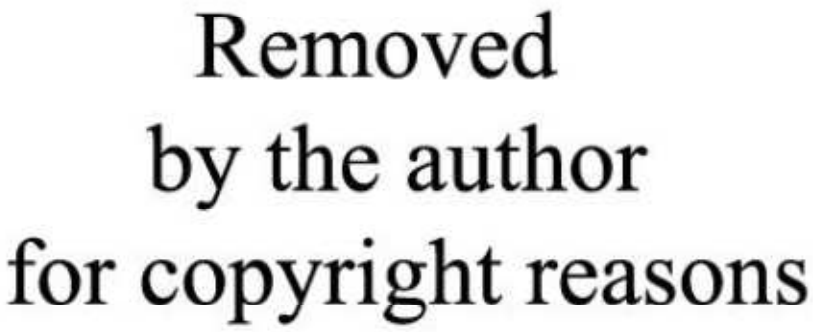

Figure (4-1): Plot of the number of publications in the last 20 years on carbon materials [http://charts.webofknowledge.com.eresources.shef.ac.uk].

Chapter 4- Graphite and Graphene

Graphene and graphite have recently received considerable interest due to their novel physical properties, especially Graphene. As a result of recent developments that have occurred in the study of Graphene, especially since the discovery that monolayer graphene could be grown, the field has increased rapidly as described below [2-4]

The structure of graphite comprises layers of linked hexagons of carbon atoms in a 2D system with carbon bonding involving sp^2 (trigonal). The layers are arranged in a stack-like structure in a sequence of (AB), so that half the atoms in a layer are exactly above and below the carbon atoms in the adjoining layers and half are exactly above and below the hexagon centers [5-6].

Graphene has a two-dimensional structure (single layer of graphite) and unique electronic properties. It is a one-atom-thick allotrope of carbon. The carbon atoms in Graphene are arranged in a honeycomb lattice-like structure and the material consists of two triangular Bravais lattices; where, it has two atoms for each unit cell. The subsequent reciprocal lattice contains two non-equivalent vertices [3, 7-8].Only Graphene and, to a decent estimate, its bilayer are zero-gap semiconductors (they could also be called as zero-overlap semimetals), which have a simple electronic spectrum with one type of electron and hole. While the spectra become gradually more complicated for three or more layers[9].

The optical properties and the optical constant for graphite have been determined by different models and techniques, which have also provided more accurate information about crystal states [10]. One of these techniques is related to the evaluation of the energy depending on the dielectric constant, both theoretically and experimentally [11].

Chapter 4- Graphite and Graphene

There has been interest in graphite for a long time, but the interest has certainly increased since graphene started to be made. The great optical property of graphene – i.e. the excellent optical transparency coupled with high conductivity [12], has resulted in it being involved in many applications, such as in solar cell materials and terahertz-IR detectors[12]. Reflectance and transmittance are measurements have been made as a function of frequency, temperature, and carrier density[13-14].

The optical and magneto-optical (Faraday rotation and magnetic circular dichroism MCD) properties for graphite and graphene have been studied in the IR region by many groups [15].The majority of previous work on the magneto-optical properties of graphite have been studied numerically [16]. On the other hand, all magneto-optical properties of graphene were discovered in many electromagnetic spectrums like IR [17].

In this chapter, we describe thin films of Graphite and Graphene and their characteristics, by measuring the optical absorption and the magnetic circular dichroism MCD with the Faraday rotation FR in a simultaneous time at room temperature in the visible over an energy range of 1.5-4.5 eV.

Basically, this chapter investigates the optical and magneto-optical response of two sets of thin films, which were graphite and graphene thin films. The first section of this chapter explains the crystal and band structure of graphite and graphene. This is followed by a brief study of the literature to explain the previous work which has been done on the optical and magneto-optical properties of graphite and graphene, and emphasizes the most relevant studies.

The results section will be divided into two parts. The first part is concentrated on graphite thin films in detail starting with the growth technique, where they have been grown in Sheffield.

Then the structural changes and the topography of surface for the graphite films were described by X-Ray diffraction technique XRD and AFM atomic force microscopy. A flat surface topography has been seen by the SEM measurements. However, the AFM has detected a height variation of (±5nm) for a film with a ~20nmthickness. XRD for thin graphite films will be presented [18].In addition, the optical absorption of the graphite films was used to estimate the thicknesses by considering parameters taken from the bulk. The final part of the section on graphite films will present the Faraday rotation and the magnetic circular dichroism MCD in the visible spectrum region.

The second part of the results section will concentrate on graphene thin films, which have been obtained from our collaborators in other groups. Starting with thin films growth details and describes the M-O properties of graphene thin films in the visible region.

4-2 Crystal Structure of Graphite:

Graphite is a lamellar material [6, 19] composed of bond layers; in each layer, the carbon atoms form a hexagonal two-dimensional array by covalent bonds [5-6]. As shown in Figure (4-2), the distance between two carbon atoms, or the (in-plane) bond length in a graphene layer, is 1.42Å [5-6, 9]. Every unit cell has four atoms. The lattice constants for the primitive hexagonal cell are a=2.46Å and c= 6.70Å [5-7]. The distance between adjacent layers (inter plane) is 3.35Å [5, 7, 9], and the bonding of adjacent graphene layers is due to the weak van der Waals force, hence the use of graphite as a lubricant.

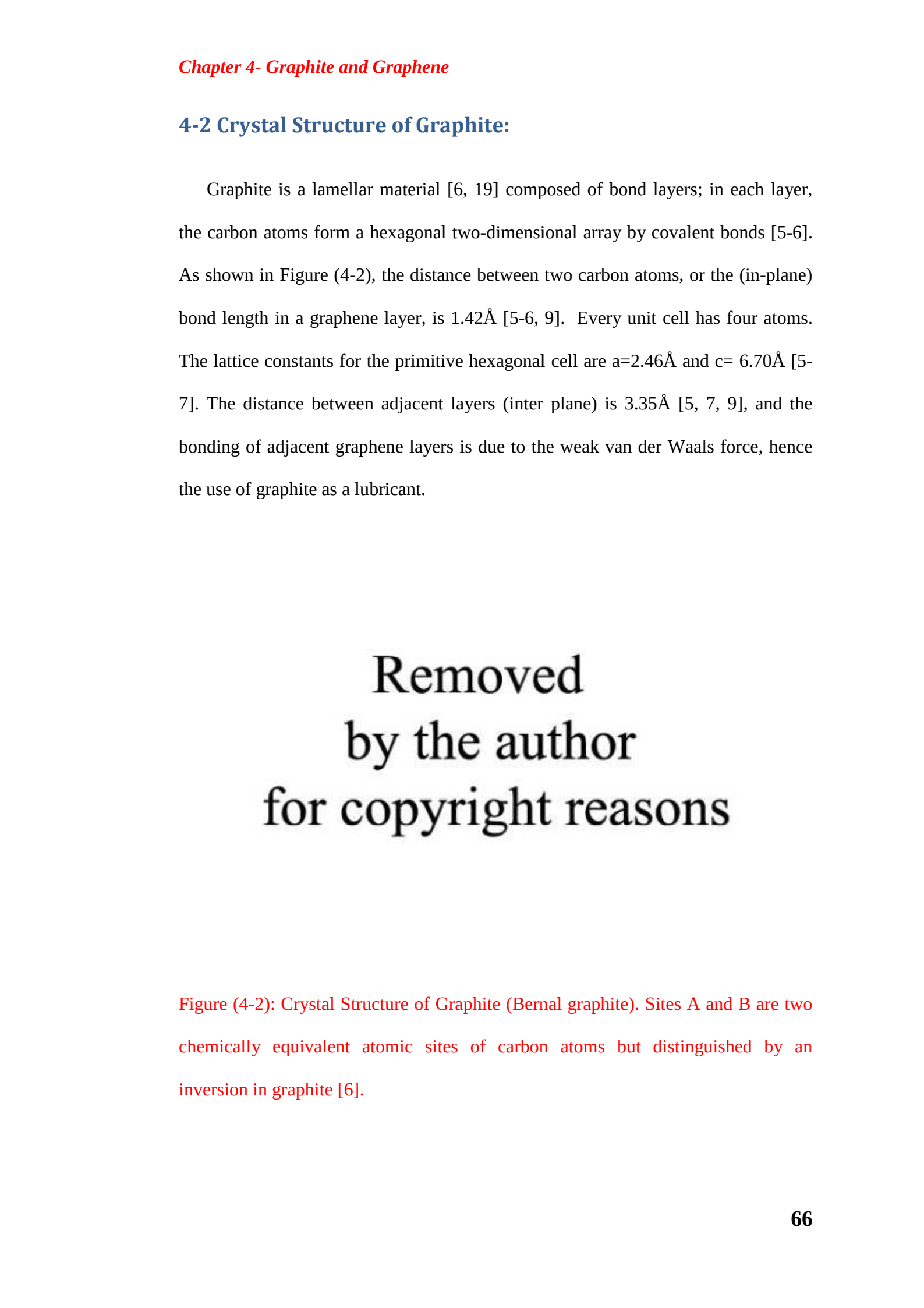

Figure (4-2): Crystal Structure of Graphite (Bernal graphite). Sites A and B are two chemically equivalent atomic sites of carbon atoms but distinguished by an inversion in graphite [6].

There are a variety of configurations for graphite layers. The first is Bernal graphite, which has an ABA stacking sequence as shown in Figure (4-2) with the lattice vectors and also in Figure (4-3a) without mentioning the lattice vectors, and the second is rhombohedral graphite Figure (4-3b), with a stacking sequence of ABCABC [5-6]. The properties and band structure of graphite are strongly influenced by the different stacking sequences (as is explained later).

As shown in Figure (4-3a) the carbon atoms in layer B of the Bernal structure are straight under the centre of a hexagonal cell of carbon in layer A. On the other hand, the angle of the carbon hexagon in layer B in a rhombohedral structure, which is directly above the centre of the hexagon in layer A; the centre of the hexagon in layer B is also below an unequal carbon hexagon corner in layer C [5-6].

However, a pure Bernal single graphite crystal is rare, which is not suitable for interpreting the physical properties, due to the occurrence of stack inaccuracy, insertion, and rise in fault intensity [6, 9]. It is worth mention that the physical structure of our graphite films it is not necessary the Bernal structure.

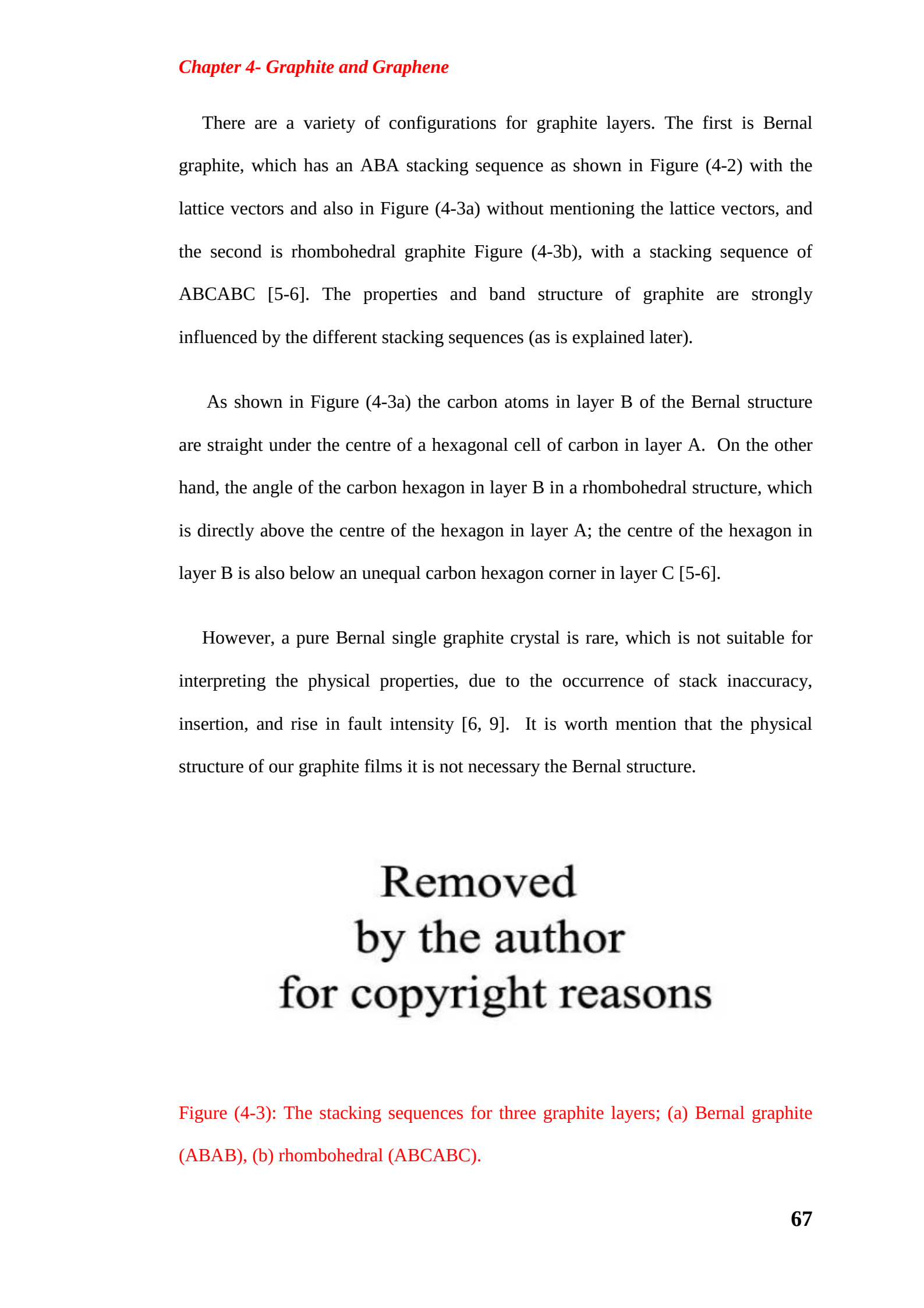

Figure (4-3): The stacking sequences for three graphite layers; (a) Bernal graphite (ABAB), (b) rhombohedral (ABCABC).

4-3 Band Structure of Graphite:

It is known that graphite is a semimetal and that a layer of single graphene is a zero-gap semiconductor [9]. Therefore, the number of layers in graphene has an effect on its electronic structure. When the number of graphene layers is increased, the behaviour of bulk graphite is recovered.

In the previous section, the different kinds of structure sequences of graphite layers were introduced. These differences affect the electronic structure of graphite, and this has been rated by a variety of models [6, 20]. The rhombohedral graphite band structure has been analyzed using the Haering -McClure model [21]. The Slonczewski-Weiss-McClure (SWCMcC) SWCMcC model is the most commonly model, which was used by Charlier to determine the ABA band structure configuration and to illustrate graphite's properties, such as the optical and transport properties close to the Fermi energy level [20]. Thus, the orbital interactions in the same and the nearest plane for carbon atoms near the Fermi level can be expressed as a function of a number of variables of the "energy eigen value" [5-6]. As can be seen from Figure (4-2), per unit cell there are four atoms. In fact, the unit cell for graphite and the graphene bilayer is the same, because of the stack of bilayer graphene forms the graphite lattice [7].

Graphite is anisotropic; the effects of the inner metallic bond within the layers make the graphite an excellent conductor in plane, electrically and thermally. In contrast, vertically, it becomes a weak electric and thermal conductor, because of the weak van der Waals forces between adjacent layers [5, 9]. This weak interaction between the inner layers is actually the main difference between graphene and

graphite. The band structure of graphite is overlapping, which causes its semimetalic properties, and it is a zero-band-gap for graphene [1, 6].

Figure (4-4) shows the Brillouin zone of graphite (Bernal structure) and also shows the SWMcC band model of 3D-graphite, which explains the electronic energy bands.

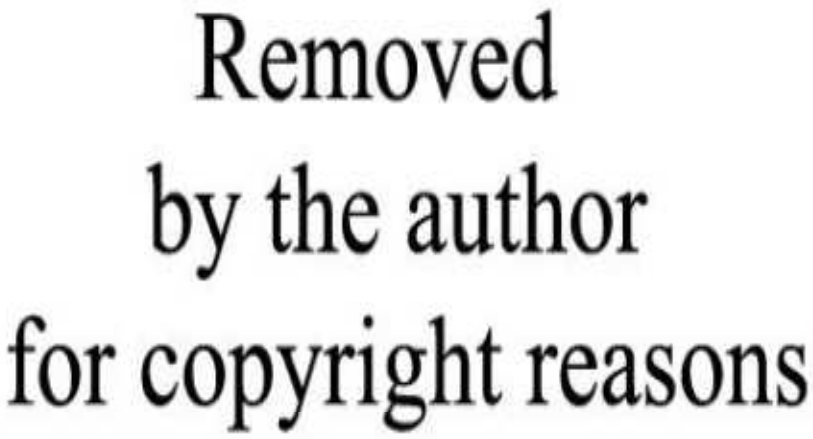

Figure (4-4): Upper figure: The Brillouin zone of graphite where the electron and hole are located in the area of the edges HKH and H'K'H'. Bottom figure; the electron energy bands of graphite near the HKH axis in the (SWMcC) model, showing the dependency of the wave vector (ξ , σ) on the energy E. [1, 5, 7]

Figure (4-5): In-plane structure of graphite and reciprocal lattice vectors [5, 22].

Chung [5] gave a clear explanation for the translation vectors and reciprocal lattice vectors for ABA, as shown in Figure (4-2), Figure (4-5) and the equations below. The coordinates for the four unit cell atoms A, B, A´ and B´ are given:

$$\overrightarrow{\rho_A} = (0,\ 0,\ 0),$$
$$\overrightarrow{\rho_B} = \frac{a}{2}\left(\frac{1}{\sqrt{3}},\ 1,\ 0\right),$$
$$\overrightarrow{\rho_{A'}} = \left(0,\ 0,\ \frac{c}{2}\right),$$
$$\overrightarrow{\rho_{B'}} = \left(-\frac{a}{2\sqrt{3}},\ -\frac{a}{2},\ \frac{c}{2}\right) \qquad \text{.....(4.1)}$$

The lattice translation vectors for an in-plane graphite crystal are:

$$\vec{a}_1 = a\left(\frac{\sqrt{3}}{2}, -1/2, 0\right), \qquad |\vec{a}_1| = a = 2.46\ A^o$$

$$\vec{a}_2 = a\left(\frac{\sqrt{3}}{2}, 1/2, 0\right), \qquad |\vec{a}_2| = a = 2.46\ A^o$$

$$\vec{a}_3 = c(0,0,1), \qquad |\vec{a}_3| = c = 6.71\ A^o \qquad \text{..... (4.2)}$$

where a_1, a_2 and a_3 are the primitive lattice vector of the orthonormal coordinates (x, y, z).The "nearest neighbour distance" for the in-plane graphite lattice is a_o=1.42 A^o, and the lattice factor is a= $\sqrt{3}$ a_o. The straight lattice vector is [5, 22]:

$$\begin{aligned}\vec{R_n} &= n_1\vec{a_1} + n_2\vec{a_2} + n_3\vec{a_3} \\ &= a\left(\frac{\sqrt{3}}{2}(n_1+n_2), \frac{a}{2}(-n_1+n_2), cn_3\right)\end{aligned} \quad \ldots\ldots\ldots\ldots\ldots\ldots\ldots\ldots (4.3)$$

where n_1, n_2 and n_3 are integers, and $\vec{a}_1$,$\vec{a}_2$, $\vec{a}_3$ are the translation vectors.

The reciprocal lattice vectors b for graphite are determined as a function of the primitive vectors:

$$\begin{aligned}\vec{b_1} &= \frac{2\pi}{a}\left(\frac{1}{\sqrt{3}}, -1, 0\right), & |\vec{b_1}| &= \frac{2\pi}{a}\frac{2}{\sqrt{3}} \\ \vec{b_2} &= \frac{2\pi}{a}\left(\frac{1}{\sqrt{3}}, 1, 0\right), & |\vec{b_2}| &= \frac{2\pi}{a}\frac{2}{\sqrt{3}} \\ \vec{b_3} &= \frac{2\pi}{c}(0, 0, 1), & |\vec{b_3}| &= \frac{2\pi}{c}\end{aligned} \quad \ldots\ldots\ldots\ldots\ldots\ldots\ldots\ldots (4.4)$$

As shown in Figure (4-4), this reciprocal lattice shapes the outline of the first Brillouin zone, and the reciprocal lattice vector is [5, 22]:

$$\begin{aligned}\vec{G_m} &= m_1\vec{b_1} + m_2\vec{b_2} + m_3\vec{b_3} \\ &= \left(\frac{2\pi}{\sqrt{3}a}(m_1+m_2), \frac{2\pi}{a}(m_1-m_2), \frac{2\pi}{c}m_3\right)\end{aligned} \quad \ldots\ldots\ldots\ldots\ldots\ldots\ldots\ldots (4.5)$$

Wherem_1, m_2 and m_3 are integers.

4-4 Band Structure of Graphene:

Graphene was first isolated in 2004 and, since then, it has won the attention of many researchers, who have attempted to explain it is unique mechanical, electrical, thermal and many other properties. Its electronic properties are considered to be an attractive feature of graphene [14, 23].

Graphene is a single layer of graphite, with Dirac charge carriers [24], where the charge carriers have an energy depend linearly on K. The pattern of the 2D layers of the carbon atoms is a hexagonal structure, as shown in Figure (4-6) [8].

Figure (4-6): Graphene structure.

One of the unique electronic properties of graphene is its mobility (1400 $cm^2V^{-1}s^{-1}$); this is higher than the mobility of a bulk Si semiconductor [23]. The free carbon atoms have a $1s^2 2s^2 2p^2$ electron arrangement, while in the 2s, 2px, 2py and 2pz orbits, the major roles in bonding are played by valence electrons [25].

The dispersion relation close to the Dirac point in pristine graphene is $E = \pm\hbar v|q|$ (where v is the Fermi velocity and q is the Brillouin zone point or Dirac point) [23]; hence at the K point, for pristine graphene the valence and conduction

band meet together and form a "cone shape" [23]. Conversely, the conduction band is produced by the upper π anti-bonding, and the valence band is produced by the lower π bonding [6]. The most noticeable properties at this point are that the velocity of all conduction electrons have the value of ~ *C*/300, where *C* is the speed of light [8], without regard to their energy; the Fermi level (E_f) is at the cross-over point, as seen in Fig (4-7a), and the density of state at these levels is zero, which is the reason for the zero-gap in graphene [23, 25]. Figures (4-7b) and (4-7c) illustrate that the Fermi levels (E_f) lie in the valence band for p-type graphene, while (E_f) lies in the conduction band for the n-type band structure of graphene [8, 23].

Figure (4-7): Schematic band structure of single layer graphene. (a) Band structure of pristine graphene (b) p- type and (c) n- type graphene band gap [23].

The honeycomb lattice in graphene includes two in equivalent carbon atoms, A and B, or, in another expression, two equivalent carbon sub lattices, A and B Figure (4-8) [7], so the lattice (unit) vectors a_1 and a_2 are[6, 25]:

$$\mathbf{a}_1 = \left(\sqrt{3}a/2, a/2\right), \mathbf{a}_2 = \left(\sqrt{3}a/2, -a/2\right) \quad \text{…….……} \quad (4.6)$$

(a=2.46 A^o) the lattice constant.

Figure (4-8): Graphene hexagonal lattice, a_1 and a_2 the lattice unit vectors [7].

In 1947, Wallace proposed the first graphene tight-binding model [26]. He explained that "the nearest and next nearest neighbour interaction between p_z orbital with the neglect of the overlap between the wave function from more remote atoms." Equation (4.7) represents the form of the graphene π electron [7, 26] dispersion relation that is calculated to the nearest neighbour from the tight-binding.

$$E(k_x, k_y) = \pm\gamma\sqrt{1 + 4\cos\left(\frac{\sqrt{3}k_x a}{2}\right)\cos\left(\frac{k_y a}{2}\right) + 4\cos^2\left(\frac{k_y a}{2}\right)} \quad \ldots\ldots\ldots (4.7)$$

When $k_x = \frac{2\pi}{\sqrt{3}a}$, and $k_y = \frac{2\pi}{3a}$ that means the E (kx, ky) = $E\left(\frac{2\pi}{\sqrt{3}a}, \frac{2\pi}{3a}\right) = 0$ Eq(4.7) will be zero.

Where γ = 2.7 eV is the hopping energy for the nearest neighbour carbon atoms in the π orbital. a_{cc} =1.42 A^o represents the distance between two carbon atoms [6-7, 27].

The plus and minus sign in equation (4.7) sequentially means that the anti-bonding π* is empty and the π band is full in graphene, where the two bands (π, π*) contact at the points (K, K′) respectively [7]. An expansion of equation (4.7) around (K, K′) points yields to a linear dispersion bands, which is the previous relation used in pristine graphene $E = \pm\hbar v|q|$, where q is measured with respect to the K-point [7].

4-5 Previous Work

4-5-1 Optical and Magneto-Optical Properties of Graphite:

Optical properties and the optical constant for graphite have been determined by different models and techniques, which have also provided more accurate information about crystal states [10, 15]. Many of these techniques are related to the evaluation of the dielectric constant, both theoretically and experimentally [28-31].

Usually, from an optical point of view, graphite in all its forms is considered as uniaxial, where the c optic axis is perpendicular to the plane. Therefore, in order to be able to explain the optical response at each wavelength, two complex optical functions are needed. The light polarized perpendicular to the c axis was described by using the ordinary dielectric function $\varepsilon_o(\lambda)$. While, to describe the light polarized interaction along to the c axis, the extraordinary dielectric function $\varepsilon_e(\lambda)$were was used [15]. In order to obtain the complex dielectric function$\varepsilon(\lambda)$, which is associated with the complex refractive index [$\varepsilon(\lambda) = \tilde{n}^2 = (n + ik)^2$], and optical absorption coefficient $\alpha = 4\pi k/\lambda$, we need to know n, k and λ, the

refractive index, extinction coefficient and light wavelength, respectively. All the known values are in table 4.1[15],

Absorption spectroscopy is a broadly used technique to study and present the essential optical properties of the materials. This operates by measuring the spectra of reflection and transmission as a function of energy at room or low temperatures. Our absorption system was described in details in Chapter 3, the light source covers the energy range from 1.5 eV to 4.5 eV. All the measurements for the graphite and graphene thin films were taken within that energy range.

In this chapter, optical absorption is used as a method to estimate the film thicknesses and its orientation, using a complex refractive index from bulk parameters[15], considering the reflection from the front and back sides of graphite films, which will be explained later in the results section of this chapter.

Similar to the optical properties the Magneto-Optical properties for graphite have been investigated numerically [16]. Magneto-optics, which has been explained in Chapter 3, is a description tool of the observed optical effects that occurs when light interacts with matter under an external magnetic field.

Therefore, we found that measuring the Faraday rotation in the visible region for graphite thin films and compare it with theory, would be an interesting research[16]. In addition, our M-O system also measures both the magnetic circular dichroism MCD and the Faraday rotation simultaneously together. There are no available calculations and studies of the MCD for graphene and graphite in the visible region.

Removed
by the author
for copyright reasons

Table 4.1: Refractive index and extinction coefficient at different wavelength [15].

4-5-2 Optical and Magneto-Optical Properties of Graphene:

There is massive amount of literature on the optical properties and of Graphene. Due to interband and intraband transitions, Graphene has clear and ordinary optical absorptions. Graphene absorption spectrum shows different behaviour within the optical regions. The absorption spectrum of graphene in the visible range is frequency independent. In the UV-region an excitonic absorption peak shows up (as predicted in theory). While the Drude absorption peak is observed in the far-IR (FIR) region [12].

The important optical property of graphene – i.e. the excellent optical transparency [12] – has resulted in it being involved in many applications, such as in solar cell material and terahertz-IR detectors [12].

Chul et al[12]used the chemical vapour deposition technique to grow graphene and calculate the spectrum for optical transmission and reflection, some of the data is

shown in the Figure (4-9). The frequency ranged from far-IR to UV range (4meV-6.2eV) [12-13]. They also noticed a Drude peak in the absorption in the far-IR region [12].We note that the absorption data is remarkably similar to $<\varepsilon_2>$ of graphite as shown in Figure (4-10) adapted from Jellison[15].

Figure (4-9): (a) Large-scale graphene/sapphire and sapphire transmission and reflection in the UV-region; (b) the experimental and theoretical absorption of large-scale graphene and monolayer graphene, respectively [12].

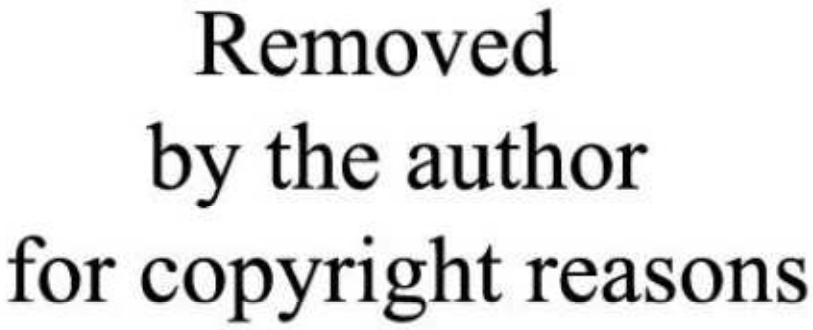

Figure (4-10): The pseudo-dielectric function was measured for the HOPG samples, with a perpendicular c axis to the surface. The measurements were taken at various angles of incidence which shown in the figure [15].

Crasseeet al [32] and her group used different methods to measure the Faraday rotation in graphene (single and multilayer) in the Infrared. They put the sample on top of a “split-coil” and placed a “grid-wire gold polariser” in front and after the sample Figure (4-11). By rotating the two polarisers, the Faraday rotation can be measured from the rotation angle [17, 32].

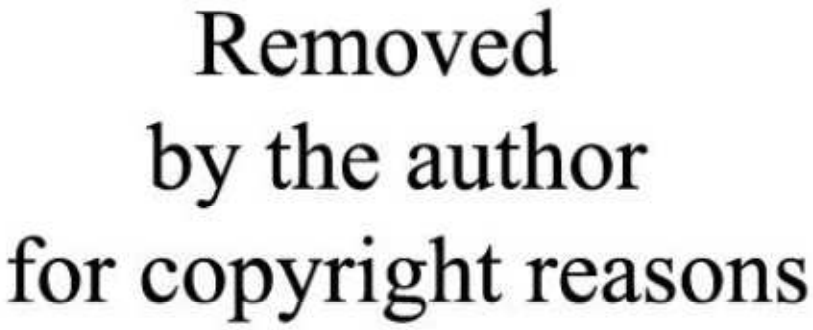

Figure (4-11): The magneto-optical Faraday rotation experiment diagram.

4.6 Present Work

4.6.1Graphite Thin Films

4.6.1.1 Graphite Sample Preparations

A cylinder of carbon, from GoodFellow Cambridge limited with purity of 99.997% was used to prepare a graphite target. The cylinder was chopped into small cylindrical pellet of 25 mm diameter and about 5 mm thickness and then located on the target holder using a sticker. A set of graphite films of varying thickness was grown using pulsed laser deposition (PLD). All the films were made in Sheffield by PLD using an excimer Xe-Cl laser operate at 308 nm wavelength. The optical pulse length of the laser is about 28 ns and it operates at 10 Hz pulse frequency which gave an energy density of up to 400 mJ per pulse, as explained in Chapter.3.

A series of films was made from single targets at base oxygen pressure 1.85×10^{-5} Torr and deposited on c-cut sapphire substrates at a distance of 50 mm, that was held at 450°C for various time depositions, see table (4.2).

In addition to the PLD technique, spin coating was also used to prepare the thin films. An excess amount of a solution of graphite in acetone solution was placed on a sapphire substrate, which was then rotated at typically 2000 to 4000 rpm to spread the graphite fluid by centrifugal force. We found that graphite thin films which were made by the pulsed laser deposition technique are better quality than the spin coating technique that produced rougher films. All the results given in this chapter for graphite are for films made by PLD.

Sample	Deposition time(minute)
PldGr2	4
PldGr3	2
PldGr4	1
PldGr5	30 second
PldGr6	15 second

Table (4.2): Growth details for Graphite thin films by PLD on a sapphire substrate, held at 450°C deposition temperature.

4.6.1.2 Graphite Characterisations (Physical)

In this section, we will present several methods that been used to provide us with structural information including the texture and crystallization for the graphite thin films that were grown by PLD.

A Dektak surface profiler was utilized to measure the thickness of the samples, which represented the real thicknesses for the films. In addition, the optical absorption data by using parameters taken from the bulk was used to estimate the thicknesses of the films. Where, taking in to account, the front and back side's reflections of the film, in order to get the effective thickness, which is the thickness of the part of the film that is aligned parallel to the plane. Then, this was compared with theory, the details are given in section (4.6.1.3) [15].

The Dektak/bulk thickness measurements showed that the thickness depends linearly on the deposition time for graphite films as expected; this is shown as black line in Figure (4-12). The value of the thickness was also obtained from the optical absorption (case A, B and C – the methods are discussed later) assuming perfect alignment in the graphite grains in the plane of the film and using the value of $\tilde{\varepsilon}_{xx}$ for bulk graphite. Optical estimates gave a consistently lower value of the thickness, which indicates some misalignment of the films because, as is clear from Figure (4-12), the absorption coefficients are very anisotropic, however, it is hard to get a quantitative measure of the amount of misalignment from this set of data.

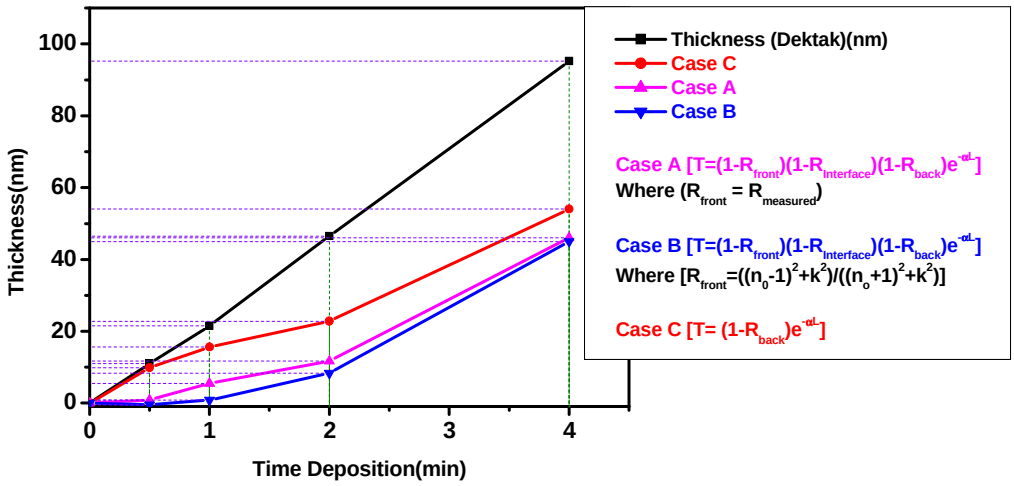

Figure (4.12): Graphite film thickness measured by Dektak and optical density by using different reflections equations, using bulk experimental values for the absorption α (as will be discussed in section 4.6.1.3).

The topography for the grain size surface, and the structural changes of the graphite films were characterized by AFM atomic force microscopy and XRD. All the following films were grown at base pressure by PLD at 450 ºC deposition temperature. Dr. Xiaoli Li performed the XRD and AFM measurements in the Key Laboratory of Magnetic Molecules and Magnetic Information Materials, Shanxi Normal University in China

X-ray diffraction XRD is a widely used technique to investigate the structure of thin films. Figure (4.13) shows the XRD patterns of the graphite films grown on sapphire substrate at a base pressure for (1 minute).

The XRD demonstrates two peaks, the first peak indexed as (002) is for small crystallites of graphite aligned with the c axis perpendicular to the plane. The second

peak is from the sapphire substrate, which also shows that the films were partially textured. The appearance of the (002) diffraction line in the XRD pattern is a behaviour we ought to observe because it represents the separation of the carbon atoms between the planes. Lin, et al. [33] have reported the same behaviour for the graphite cathode, as shown in Figure (4.14).The first prediction was we thought that the films were aligned due to the sharp (002) peak, and when they are not aligned the (101) peak is always weaker.

As seen in Figure (4.13) there was no evidence of the (101) peak index around $2\theta = 55^{o}$, which may imply that most of the grains were aligned with c axis normal to the film. Even if the (101) peak were present we still could not detect it; therefore, we cannot deduce that the films were entirely aligned. However, in bulk polycrystalline graphite, the (101) peak was significantly less intense than the (002) peak so this is not a sensitive test of alignment Figure (4.14).

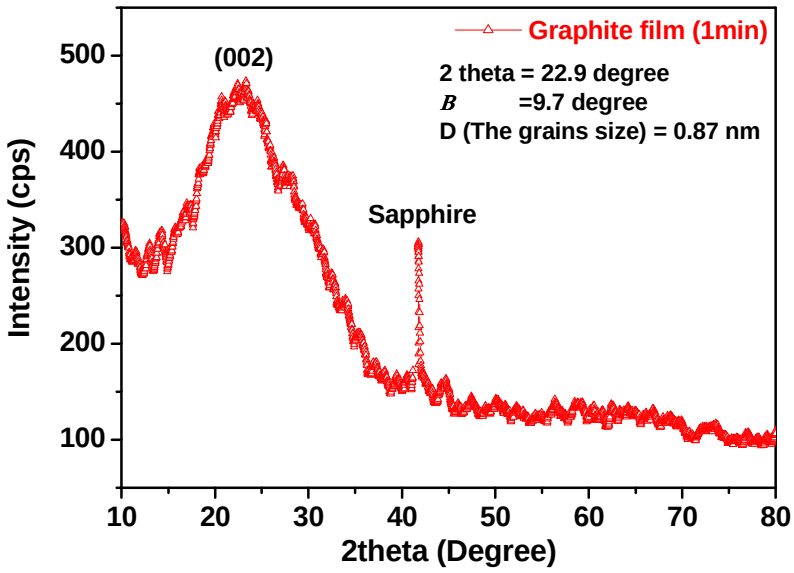

Figure (4.13): XRD spectrum of synthesized Graphite thin films with (21nm) Dektak thickness.

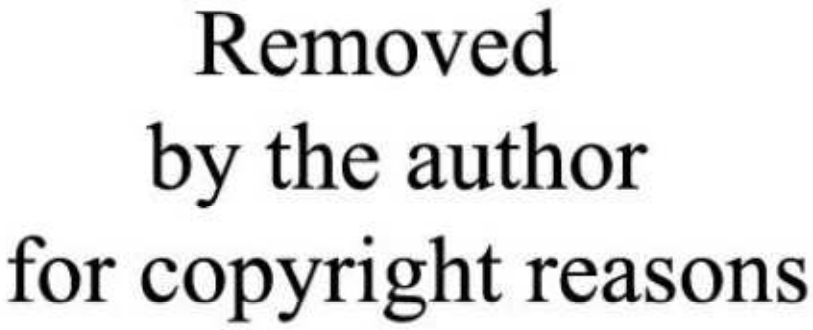

Figure (4.14): X-ray diffraction patterns of natural graphite, pyrolytic graphite (PG) and graphite foam. The relative sizes of the 26.55^{o} and 55^{o} peaks is clearly evident [33].

We can calculate the average size of the crystalline grains in the graphite films using the Debye-Scherrer formula as given:

$$D = \frac{0.94\,\lambda}{\beta\cos\theta} \qquad \ldots\ldots\ldots\ldots\ldots\ldots (4.8)$$

Where D is the grain size, λ= 1.5406 Å is the wavelength of Cu Kα X-ray, θ the diffraction angle, and β is the full width at half maximum (FWHM) in radians. The grain size of the (1minute) films is about 8.7A^{o} which is quite comparable to grain height ≈ 8.6Å obtained from the AFM data. Hence the broad peak at (002) indicates the existence of the small grain size. Also, it shows that the lattice spacing is as expected were it detected from the centre of the peak. It is worth mentioning that the grain sizes for the rest of the graphite films were approximately the same value as the (1minute) film.

As mentioned previously atomic force microscopy AFM data, were obtained by Dr. Li in China. Figure (4.15) and (4.16) illustrate the AFM data for the graphite thin films with (1minute) (21nm) thickness and (30second) (11nm) thicknesses respectively, thicknesses measured by Dektak.

AFM detected a height variation of (±5nm) for the films. In addition, the AFM figures show that the grains are visible and the films are continuous.

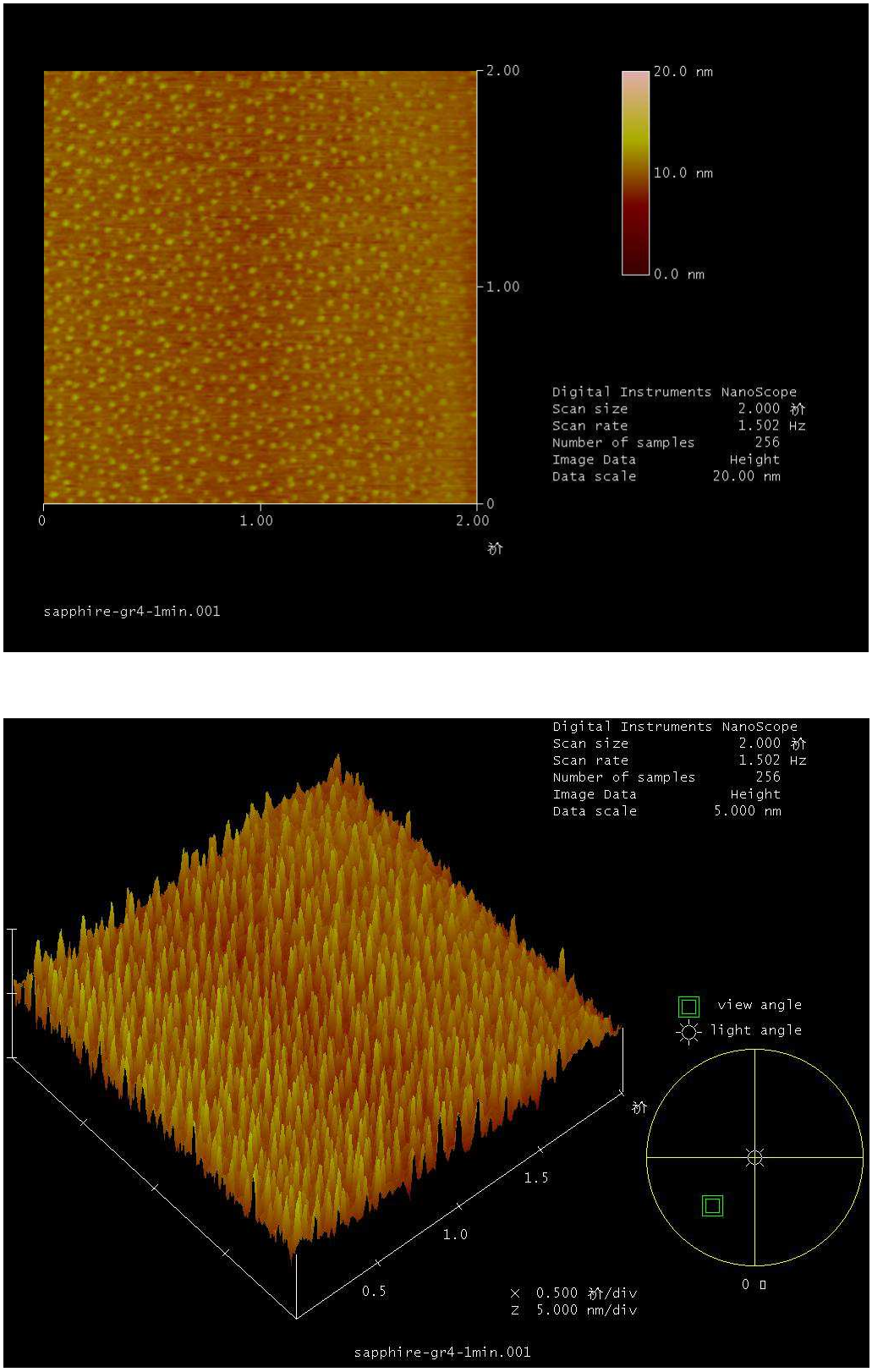

Figure (4.15): AFM for Graphite thin films with (1minute) (21 nm) thickness.

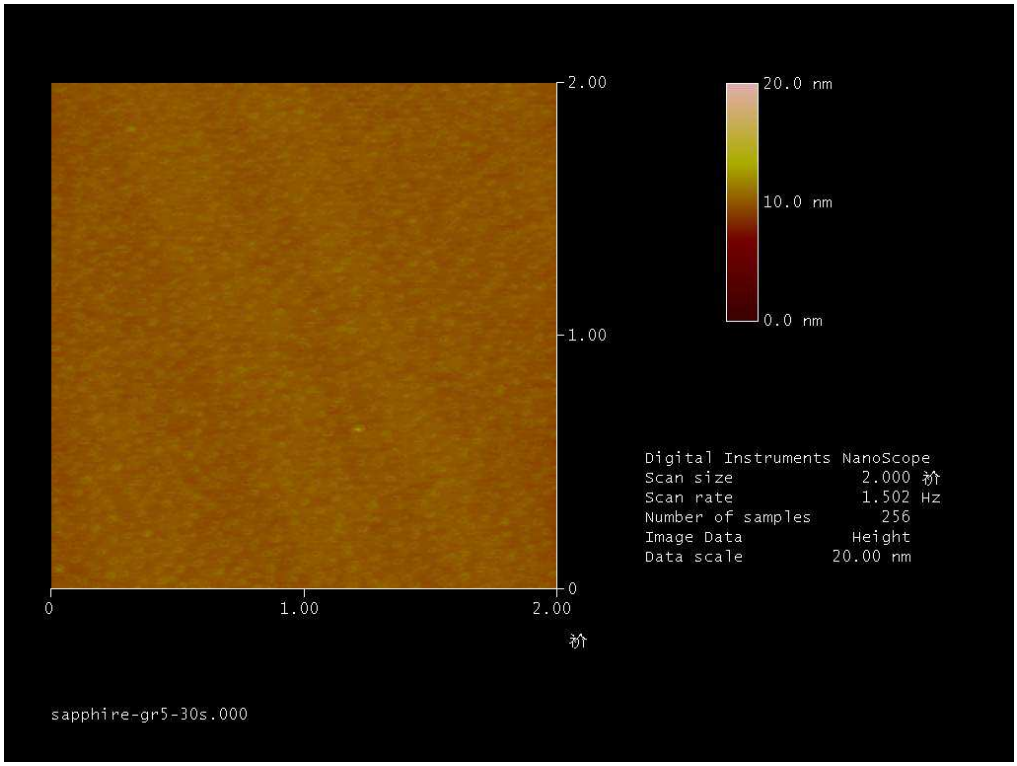

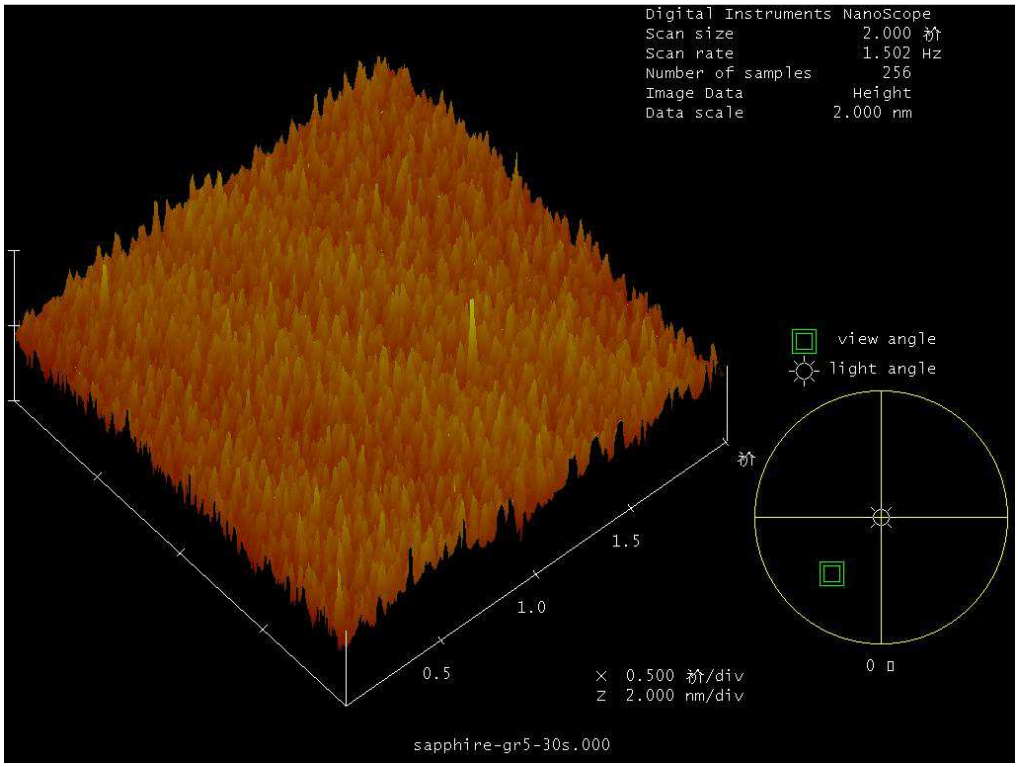

Figure (4.16): AFM for Graphite thin films with (30 second) (11nm) thickness

4.6.1.3 Graphite Optical Properties

We measured reflectance from the front and the transmittance from the back to get the absorptions α(E). As mentioned in the paper by G.E. Jellison[15] in which they reported measurements of the absorption along different directions, it was very anisotropic as expected, large for ***E*** in the x-y plane.

All the equations were described previously in Chapter 3 to determine the absorption spectrum by measuring the spectrum of reflection and transmission at room temperature, which cannot be used to determine the absorption for graphite thin films because they are too transparent. The transmission was calculated by assuming that reflectivity from the front and back surface of the film is equal. Transmission and reflection spectra of Graphite/sapphire were measured using the reflection coefficient at interfaces.

The films appeared to absorb less than what we have expected. This was probably due to the fact that the alignment in the (X and Y) direction was much bigger than that in Z-direction, therefore only a fraction of the film was contributing. Hence we put the light parallel to the Z-direction, and the electric field was all in the (X and Y) direction, to get a maximum absorption. This was only interesting in the optical absorption when we took into consideration the reflection from the back and the front surface.

To extract the properties of a very thin film on a substrate, therefore we tried several methods for that.

In all the other films that have been mentioned in this thesis the thickness can be estimated using equation 4.8 because the refractive index of the film was close to that of the substrate – but this is not valid here:

$$T = (1 - R_{front})(1 - R_{back})e^{-\alpha L} \quad \text{..... (4.8)}$$

Hence, when the films absorb very weakly by assuming a total transmission, then the transmission will depend on conservation energy and neglects scattering and reflection from the back side of the films (the assumption here is that all the light that is not absorbed is specularly reflected), is given by:

$$T = (1 - R_{measured})e^{-\alpha L} \quad \text{..... (4.9)}$$

Where R_{front}= $R_{measured}$, is the reflection from the front side of the film.

$R_{interface}$, is the reflection from the film. R_{back}, is the back side reflection of the film, or the substrate, L is the film thickness, and α is the absorption coefficient.

Case(A) For our graphite films we used different calculation methods to get the absorption and estimate the film thicknesses. There are obvious reflections, which occur at the front, middle and back interfaces.

If the absorption is strong or the film is thick, so we can neglect multiple passes, then the transmission is given by:

$$T = (1 - R_{front})(1 - R_{interface})(1 - R_{back})e^{-\alpha l} \quad \text{..... (4.10)}$$

This equation is standard, but it gave a negative α. This occurred because R_{front} is too big and there was more transmission light than expected.

Now, we describe equation (4.10) in detail. Where,

$R_{front} = R_{measured}$ …….. (4.11)

$R_{interface}$, which is the reflection from the graphite films, in this case, will be energy This is definitely an underestimate for depending on for each wave length, is by the following Eq:

$$R_{interface} = \frac{(n_{film} - n_{substrate})^2 + k^2}{(n_{film} + n_{substrate})^2 + k^2} \quad \text{…….. (4.12)}$$

Where, n_{film} and k both are optical constants, the refractive index and extinction coefficient respectively. The values are from (table1) in G.E.Jellison paper [15] for nine different wavelengths (nm), as a function of energy. n_s is the sapphire refractive index, which is energy depended on too.

Reflection from the back side of the film was obtained by using the following formula:

$$R_{back} = \left(\frac{n_s - 1}{n_s + 1}\right)^2 \quad \text{…….. (4.13)}$$

where n_s, is the refractive index of the substrate as energy in depended. Where the value of $n_s$for sapphire substrate is (≈ 1.6).

Case(B) For a few individual cases, when the film is very thin, there will be multiple reflections from the front side of the film in addition to the back reflections from the substrate. Therefore R_{front} eq (4.11) will be replaced by the following:

$$R_{front} = \frac{(n_o-1)^2+k^2}{(n_o+1)^2+k^2} \qquad \text{..... (4.14)}$$

Where, n_o and k, are the same values are from G.E.Jellison paper [15] for nine different wavelengths (nm), as a function of energy.

Case(C) In this case we depend only on the back side reflections of the film to measure the absorption and neglect front and interface reflections, as:

$$T = (1 - R_{back})e^{-\alpha l} \qquad \text{..... (4.15)}$$

This approximation will certainly give an over-estimate for the absorption α. The transmission coefficients for each film are shown in figure (4.17).

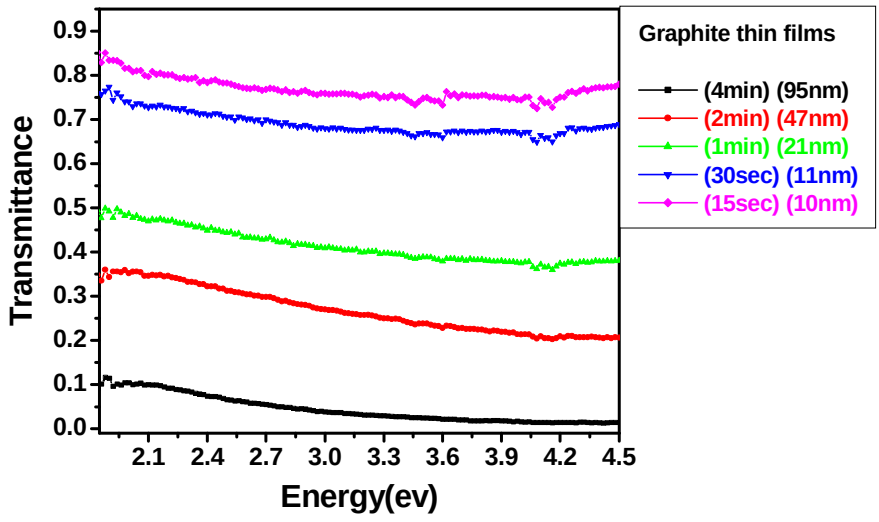

Figure (4.17): Transmission spectrum of the graphite films.

The conclusion from the previous cases is: Case A and B, overestimate light loss due to reflection since the films are not totally aligned the reflection at the interface is going to be little and that will lead to a much smaller dielectric constant. While Case C heavy underestimates the light loss. Therefore, to determine the best thickness for the graphite films to use in the M-O calculations, we need to add another case.

Case (D) by using the thickness from Case B, when we consider the reflections from the front and back of the films, and the Dektak thicknesses, we can get the aligned fraction f, as given:

$$L_B = L_{Dek} .f \qquad \text{..... (4.16)}$$

The fraction number obtained from eq (4.16) will be used in eq(4.10):

$$T = (1 - R_{front} . f)(1 - R_{interface} . f)(1 - R_{back})e^{-\alpha L_{B2}} \qquad \text{..... (4.17)}$$

Were L_{B2} is the apparent thickness obtained by taking into consideration the aligned fraction.

4.6.1.4 Graphite Magneto-Optical Properties

Magneto-optical measurements are an accurate technique that can be relied on to study and analyse graphite properties.

The magnetic circular dichroism MCD is measured in the visible region of the spectrum order simultaneously with the Faraday rotation FR (see Chapter3), for graphite thin film deposited by PLD on a sapphire substrate. The applied magnetic is

perpendicular to the plane of the sample, it is B= 1.8T, and parallel to the direction of incidence.

The absolute values of the MCD and FR for graphite thin films have been determined. However, the results are subject to error due to the uncertainty in measuring the thickness of the aligned grains because it is only this orientation that will give the large calculated FR [16].

Faraday rotations for graphite thin film deposited by PLD for (30second) and (1minute) are shown in Figure (4.18) which has been plotted depending on the Dektak thicknesses for each film. All FR figures show a strong peak around 4.09 eV also show a dip around ~ 3.7eV which is comparable to the MCD peak at the same energy as shown in Figure (4.22).

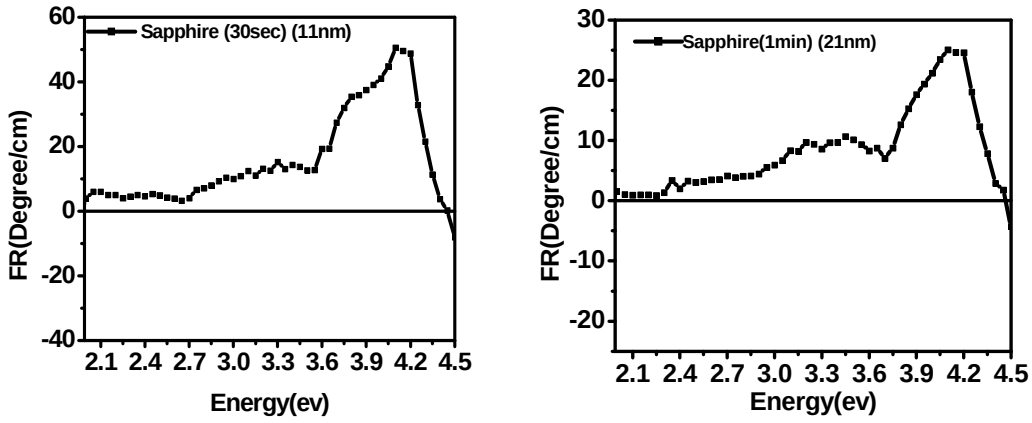

Figure (4.18): Faraday rotation for graphite thin film deposited by for (30 second), and (1minute) on a sapphire substrate in the energy range from 1.8 to 4.5 eV was measured in a field of 1.8 Tat room temperature.

In addition Figure (4.19) shows the FR for graphite thin film where the thickness of the film deposited in 1 minute has been taken as that measured by the Dektak and using the formulae given as cases A, B, C and D.

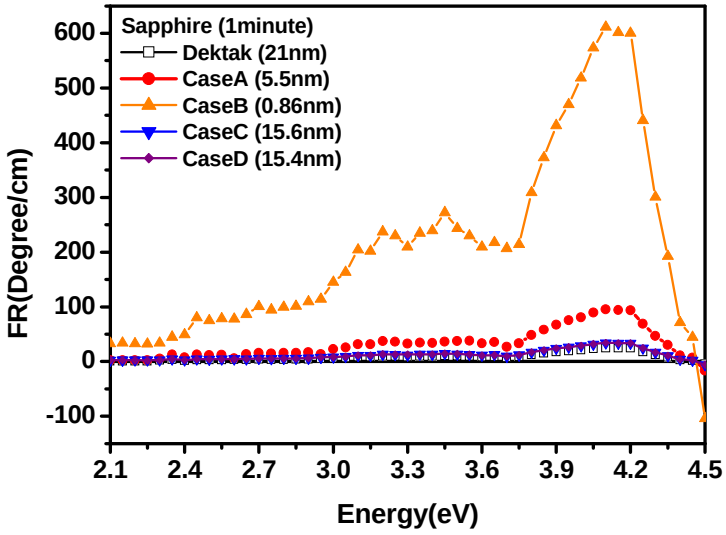

Figure (4.19): The FR for graphite thin film using the thickness measured by Dektak and the optical density using bulk values for the absorption α, deposited by PLD for (1minute) on a sapphire substrate in the energy range from 1.8 to 4.5 eV .These results were obtained in a field of 1.8 T at RT.

Therefore to demonstrating the similar behaviour seen for all graphite films which were grown in different deposition times, we scaled the FR data for all films in arbitrary units for a range between 1 and 0 as shown in Figure (4.20). Peaks at ~ 4eV are very similar but the thinner films did have a large FR in the range $2.6 < E < 3.4$ eV.

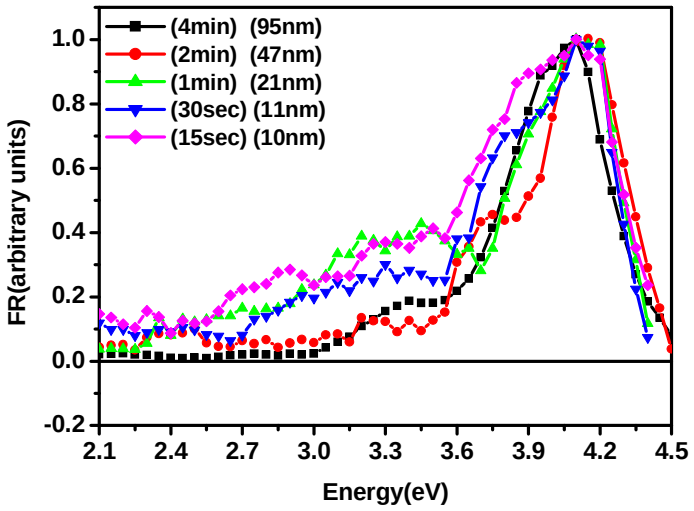

Figure (4.20): Scaled Faraday rotation for graphite thin film deposited by PLD for (4, 2 and 1) min and (30 and 15) second on a sapphire substrate in the energy range from 2.1 to 4.5 eV.

All films have approximately the same FR shapes, but the magnitudes are different as may be seen from table (4.3) and we believe this is because the alignment fraction is different; there is also a real thickness dependence. Unfortunately it was hard to work it out.

Time	Dektak (nm)	Case A	Case B	Case C	Case D	Max FR (Degree/cm)	Max FR (rad/mm.T)	Max MCD (Degree/cm)
2min	47±2	11.7	8.33	22.8	20.8	26.7	0.025	13.6
1min	21±2	5.5	0.86	15.6	15.4	25	0.025	40.5
30sec	11±2	0.89	---	9.88	6.08	50.58	0.049	36.6
15sec	10±2	0.79	---	8.9	4.2	47.9	0.044	109.6
Graphene	0.335	---	---	---	---	4679	4.53	821.5

Table (4.3): Measurements of thickness using Dektak and Transmission data, assuming α in the films takes the bulk value.

On the other hand, the FR data are not compatible with Verdet constant that was given in T.G. Pedersenas shown in Figure (4.21) as the calculated number valid in the limit of very large field is much bigger than any of our measured values.

The Verdet parameter is a constant that expresses the strength of the Faraday rotation for the substance, as given in eq (4.18). It may be expressed in radian/mmT and it is temperature dependent.

$$\theta = \mathrm{VBL} \qquad \ldots\ldots\ldots\ldots\ldots\ldots\ldots\ldots\ldots\ldots \quad (4.18)$$

Where V is the Verdet constant in radian/mmT units, B is the magnetic field; L is the sample thickness and $\theta$is the angle of rotation.

Figure (4.21) illustrates the FR for graphite thin film (1minute) with (21nm) Dektak thickness in a magnetic field of 1.8 T, in Verdet constant units, and the Verdet constant spectra in a field of 158T from T.G. Pedersen [16]. It is clearly

shown that the measured Verdet constant is much smaller than that found by Pedersen.

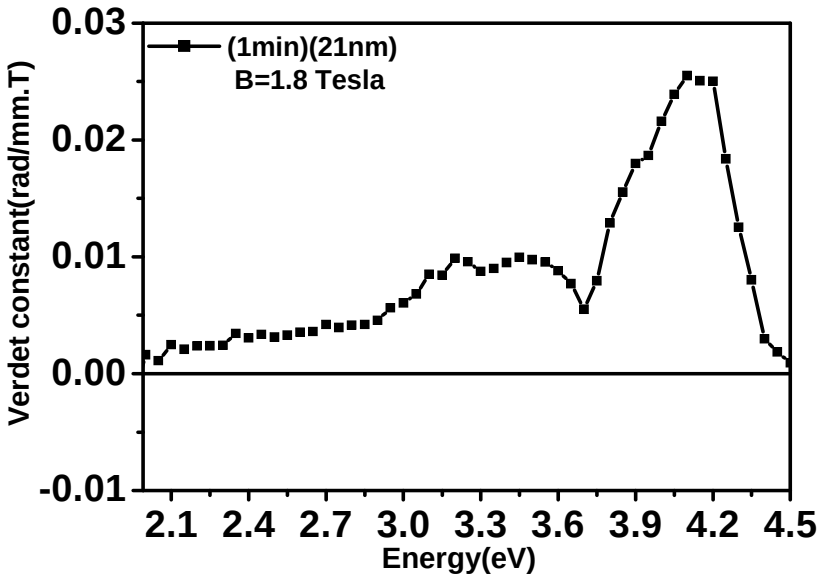

Removed
by the author
for copyright reasons

Figure (4.21): The top figure is Verdet constant for graphite thin film deposited by PLD for (1minute) with (21nm) Dektak thickness, in a field of 1.8 T. The bottom figure is Faraday rotation for calculated Verdet constant spectra, where(s) is proportional to 1/B S=700 corresponds to 158T T.G. Pedersen[16].

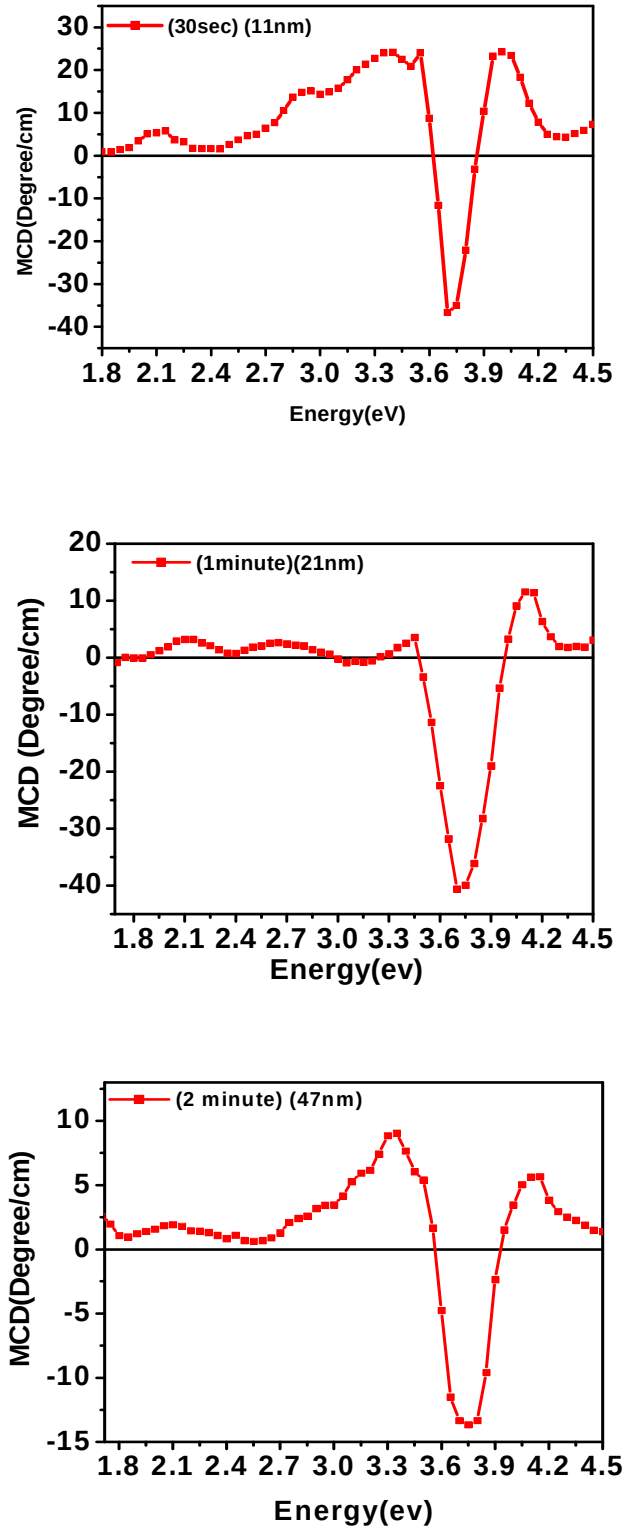

Figure (4.22): The MCD for graphite thin film deposited by PLD for (30 second), (1minute) and (2 minute) on a sapphire substrate in the energy range from 1.8 to 4.5 eV were measured in a field of 1.8 T at RT.

Figure (4.22) shows the MCD data for graphite films for (30second), (1minute) and (2minute) with Dektak thicknesses of (11nm), (21nm) and (47nm) respectively. The frequency dependence of the MCD measured on these films was comparable; however, the magnitudes were different widely as illustrated in figure (4.23) which shows the MCD data for thickness measured by Dektak and optical density using the bulk value for the absorption α.

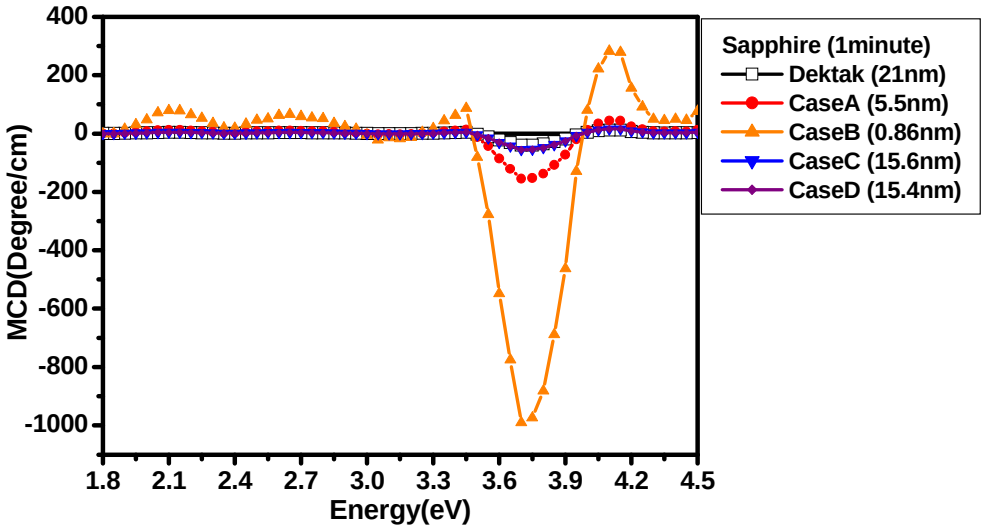

Figure (4.23): The MCD for graphite thin film deposited by PLD for (1minute) on a sapphire substrate in the energy range from 1.8 to 4.5 eV were measured in a field of 1.8 T at RT, for thickness measured by Dektak and the optical density using bulk values for the absorption α.

In addition a scaled plot in arbitrary units for a range between 1 and 0 shown in Figure (4.24) to demonstrate the similarity in the MCD behaviour for all graphite thin films grown in different deposition time.

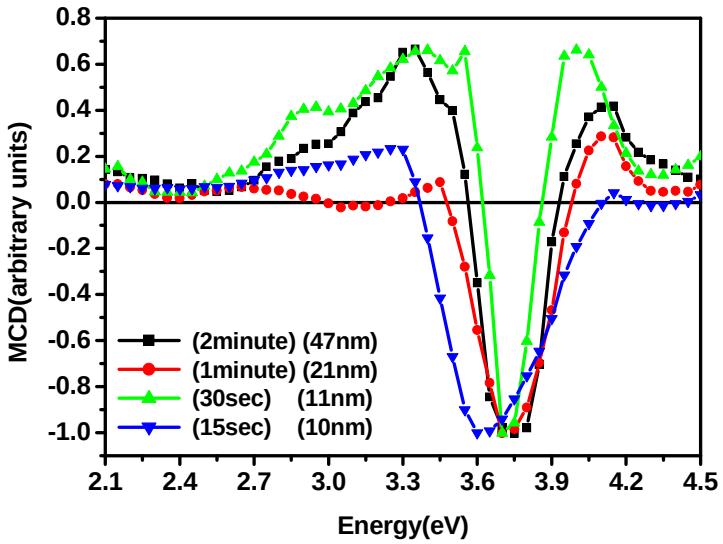

Figure (4.24): Scaled MCD for graphite thin films deposited by PLD for different times on a sapphire substrate in the energy range from 2.1 to 4.5 eV. The data was scaled so that the smallest value was -1 for each film.

The MCD data showed a strong feature at the exciton energy at ~3.7eV. The small peak in the MCD at ~4.09 eV might be due to some leaking of the FR signal into the MCD channel because of a little strain induced birefringence. The Kramers-Kronig analysis is valid for dielectric constants rather than refractive indices; however, it has often been found to be approximately correct for magneto-optics. The fact that the FR shows a dip where the MCD shows a peak at ~3.7eV is an indication that the Kramers- Kronig relations are approximately correct here.

4.6.2 Graphene Thin Films

4.6.2.1 Graphene Sample Preparations

Graphene thin films were grown by the chemical vapour deposition technique CVD on the same sapphire substrates in a collaborator group research Laboratory in the Institute of Semiconductors ,Chinese Academy of Sciences, Beijing [34].

4.6.2.2 Graphene Magneto-Optics Properties

All the previous works on M-O properties for Graphene have focused on measuring the FR and calculating it numerically in the Infra-Red IR region of the electromagnetic spectrum and in a very high magnetic field [32]. There are no previous measurements for the MCD for graphene in the visible region.

The MCD and FR presented data for graphene film was in the energy range from (1.8 to 4.5) eV was taken at RT in a field of 1.8 T. In Figure (4.25) the graphene MCD data shows a strong feature at the exciton energy at ~ 3.9eV.

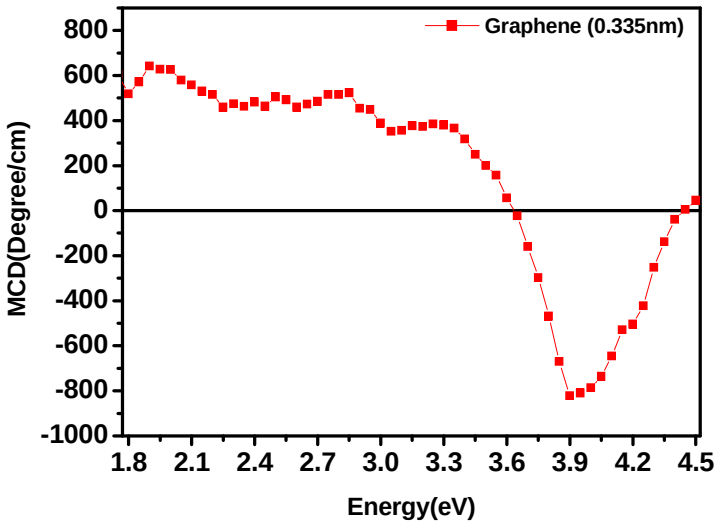

Figure (4.25): The MCD for the graphene thin films. MCD is in the energy range from 1.8 to 4.5 eV was measured at RT in a field of 1.8 T.

It has shifted a bit from the energy range that has been found previously in graphite films ~ 3.7eV. This is worrying because the Kramer-Kronig relations predict that the peaks of the FR and MCD occur at different energies, but the peaks shown in figures (4.25) and (4.26) are both at 3.9eV. Also the FR is very large compared with the MCD. Hence the results here need to be repeated before publication.

In addition, the Faraday rotation in Verdet units for Graphene thin film is shown in Figure (4.26). Both spectrum FR and MCD have a comparable behaviour, which is seen around the exciton energy value at ~ 3.9eV.

We see that the Verdet constant for graphene taken from this measurement is much closer in magnitude to that given by the theory rather than the graphite [16]. Hence the results still need to be verified before publication.

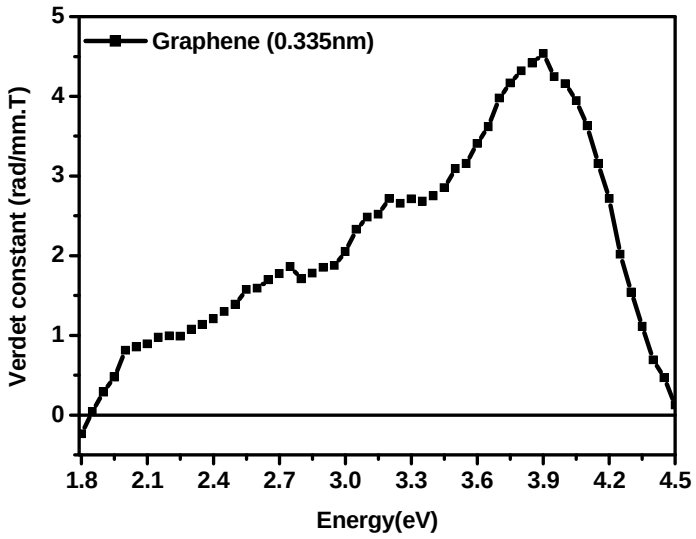

Figure (4.26): The Faraday rotation in Verdet constant units for Graphene thin film prepared by low-pressure chemical vapour deposition on a sapphire substrate too. The Verdet constant is in the energy range from (1.8 to 4.5) eV was measured in 1.8 T field at RT.

4.7 Summary

- This chapter reported the investigations of the optical and magneto-optical properties of graphite and graphene thin films and it concentrated on explaining the physical characterizations, the optical methods and the M-O effects for graphite thin films. The results for graphite were compared those for with graphene.
- Two techniques have been used to made graphite thin films; pulsed laser deposition and a spin coating technique. We found that graphite thin films that had been made by pulsed laser deposition technique were better quality than those produced by spin coating method. All the results are given in this chapter for graphite thin films made by PLD on the sapphire substrate.
- Dektak measurements of the thickness showed that the thickness of the films depended linearly on the deposition time.
- Because the optical properties of graphite are very anisotropic and the Faraday rotation had been calculated only for a magnetic field aligned along the z-axis, we needed to know the level of alignment of the films. Hence we used the optical density to estimate the level of alignment. We assumed that the magneto-optical effects would be smaller in other orientations in common with the other components of the dielectric tensor.
- The value of the thickness was obtained using different methods for estimating the optical absorption. All methods that were applied in this chapter assumed an alignment of the graphite grains in the plane of the film and using the value of ε_{xx} for bulk graphite [15] gave a consistently lower value which indicates some misalignment.

- If we assume that graphite films are sufficiently aligned so we could use the calculated values of the reflection from the front and the interface between the substrate and the film using the measured value of ε_{xx}, we got unphysical values for α, therefore the films were not entirely aligned.
- The XRD for graphite films shows only two peaks, the first (002) peak is for a small crystallites of graphite and the second peak is for the sapphire substrate [18], which revealed that at least some of the films were aligned with z perpendicular to the plane of the film.
- AFM detected a height variation of (±5nm) for a graphite film of thickness approximately (21nm) and (11nm) for (1minute) and (30second) deposition time respectively (these thicknesses were measured by Dektak).

- We found that the spectral shapes of the Faraday rotation and the MCD found from different films were very similar. However, the magnitudes varied widely which we ascribed in part to the uncertainty in measuring the thickness of the aligned grains.
- Both the Faraday effect and MCD (measured per unit thickness) are very much larger for graphene.
- There are oscillations due to standing waves in the FR at low energies for graphite films, and the FR of graphite was positive, which are both in agreement with theory.
- The MCD data for both graphite and graphene shows a strong feature at the exciton energy at ~3.7eV and 3.9eV respectively.

4.8 References

[1] M. S. Dresselhaus, "Fifty years in studying carbon-based materials," Physica Scripta, vol. T146, p. 10pp, (2012).

[2] A. K. Geim and A. H. MacDonald, "Graphene: Exploring carbon flatland," Physics Today, vol. 60, pp. 35-41,(2007).

[3] A. K. Geim and K. S. Novoselov, "The rise of graphene," Nature Materials, vol. 6, pp. 183-191,(2007).

[4] A. K. Geim, "Graphene: Status and Prospects," Science, vol. 324, pp. 1530-1534, (2009).

[5] D. D. L. Chung, "Review graphite," Journal of Materials Science, vol. 37, pp. 1475-1489, (2002).

[6] X. Li, "Epitaxial Graphene Films On Sic: Growth,Characterization, And Devices," Institute of Technology: Georgia. p. 141, Georgia, (2008).

[7] C. N. R. Rao, et al., "Graphene: The New Two-Dimensional Nanomaterial," Angewandte Chemie-International Edition, vol. 48, pp. 7752-7777, (2009).

[8] M. Fox, Optical Properties of Solids vol. Second Edition ed. Oxford Universtiy: Press Inc.,New York (2010).

[9] B. Partoens and F. M. Peeters, "From graphene to graphite: Electronic structure around the K point," Physical Review B, vol. 74, pp. 075404,(2006).

[10] E. A. Taft and H. R. Philipp, "Optical Properties Of Graphite," Physical Review, vol. 138, pp. A197-&,(1965).

[11] Y. Wang, et al., "Room-Temperature Ferromagnetism of Graphene," Nano Letters, vol. 9, pp. 220-224, (2009).

[12] C. Lee, et al., "Optical response of large scale single layer graphene," Applied Physics Letters, vol. 98, pp.071905, (2011).

[13] L. A. Falkovsky, "Optical properties of graphene," in International Conference on Theoretical Physics 'Dubna-Nano2008'. vol.129, pp.012004, (2008).

[14] B. D. A. Daniel R. Cooper, Nageswara Ghattamaneni, Benjamin Harack,, et al., Experimental Review of Graphene. [Review Article]. Volume 2012, Article ID 501686, 56 pages, (2012).

[15] G. E. Jellison, Jr., et al., "Measurement of optical functions of highly oriented pyrolytic graphite in the visible," Physical Review B, vol. 76, p. pp.085125, (2007).

[16] T. G. Pedersen, "Tight-binding theory of Faraday rotation in graphite," Physical Review B, vol. 68, p. pp.245104, (2003).

[17] J. C. Martinez, et al., "Giant Faraday and Kerr rotation with strained graphene," Optics Letters, vol. 37, pp. 3237-3239, (2012).

[18] L. Tang, et al., "Preparation, Structure, and Electrochemical Properties of Reduced Graphene Sheet Films," Advanced Functional Materials, vol. 19, pp. 2782-2789, (2009).

[19] K. S. Novoselov, et al., "Electric field effect in atomically thin carbon films," Science, vol. 306, pp. 666-669, (2004).

[20] J. C. Charlier, et al., "Tight-Binding Model For The Electronic-Properties Of Simple Hexagonal Graphite," Physical Review B, vol. 44, pp. 13237-13249, (1991).

[21] R. R. Haering, "Band Structure Of Rhombohedral Graphite," Canadian Journal of Physics, vol. 36, pp. 352-362, (1958).

[22] A. M. Dodd Gray, Bhaskar Mookerji, "Crystal Structure of Graphite, Graphene and Silicon," Physics for Solid State Applications, vol. 2, pp. 3-5, (2009).

[23] Beidou Guo1, Liang Fang1,*, Baohong Zhang2 and J. R. G. , *, "Graphene Doping: A Review," Insciences J. , vol. 1(2), pp. 80-89, (2011).

[24] W. Bao, et al., "Stacking-dependent band gap and quantum transport in trilayer graphene," Nature Physics, vol. 7, pp. 948-952, (2011).

[25] F. G. A. H. Castro Neto "The electronic properties of graphene," Reviews Of Modern Physics, vol. 81, pp. 109-162, (2009).

[26] P. R. Wallace, "The Band Theory Of Graphite," Physical Review, vol. 71, pp. 476-476, (1947).

[27] S. Reich, et al., "Tight-binding description of graphene," Physical Review B, vol. 66, pp.035412, (2002).

[28] A. B. Djurisic and E. H. Li, "Optical properties of graphite," Journal of Applied Physics, vol. 85, pp. 7404-7410, (1999).

[29] G. H. GREENAWAY.D. L., F. BASSANI, and E. TOSATTI, "Anisotropy of the Optical Constants and the Band Structure of Graphite," Phys. Rev. B, vol. 178, p. 1340, (1969).

[30] L. G. Johnson and G. Dresselhaus, "Optical Properties Of Graphite," Physical Review B, vol. 7, pp. 2275-2284, (1973).

[31] R. F. Willis, et al., "Secondary-Electron Emission-Spectroscopy And Observation Of High-Energy Excited-States In Graphite - Theory And Experiment," Physical Review B, vol. 9, pp. 1926-1937, (1974).

[32] I. Crassee, et al., "Giant Faraday rotation in single- and multilayer graphene," Nature Physics, vol. 7, pp. 48-51, (2011).

[33] M.-C. Lin, et al., "An ultrafast rechargeable aluminium-ion battery," Nature, vol. 520, pp. 324-328, (2015).

[34] W. G. Luo, et al., "Synthesis of Homogenous Bilayer Graphene on Industrial Cu Foil," Chinese Physics Letters, vol. 31, p. pp.067202, (2014).

Chapter 5

Magneto Optical Studies of non-Magnetic ZnO Thin Films

5.1 Introduction

This chapter is focused on presenting and explaining the benefits of conducting magneto-optical studies on non-magnetic ZnO and doped ZnO. We will discuss how the magnetic circular dichroism MCD is a powerful technique to identify the energy gap states in weakly absorbing polar ZnO thin films that have been grown either by molecular beam epitaxy MBE or by pulsed laser deposition PLD with and without Al. The capability of MCD to detect the energies of the states that arise from extended defects and oxygen vacancies will be explored in the chapter for both types of thin films. The PLD thin films preparation and the MCD measurements were undertaken at the University of Sheffield (UoS). The MBE thin films were grown by Dr. Ying at the Key Laboratory of Beam Technology, Beijing Normal University in the Republic of China [1].

5.2 Understanding Use of Non-magnetic pure and doped ZnO.

Doping is an important practice for semi-conductor nanostructures to facilitate the control of their physical properties. It has been found that ZnO has many more potential applications following doping, including uses in nano wires and other forms of nanostructures, along with other transition metals such as nickel, iron and cobalt [2-3]. Zinc oxide's range of band gaps around (3.4eV) in the UV region and it is large exciton binding energy at room temperature (estimated as 60meV) gives it many potential use in ultraviolet (UV) luminescence devices, gas sensors, thin film transistors that are transparent in the visible spectrum, solar cells, and light emitting diodes (LEDs) [4].

The electronic and magnetic properties of the ZnO are dependent on the existence of states in the energy gap. The properties intrinsic states to pure zinc oxide are dependent on the oxygen vacancies, anti-site ions, interstitials, grain boundaries and the surfaces [3] . In other cases, it is properties are affected by the doping material that is introduced into the material to improve the intended property. The limited mobility in the wide band semiconductors is due to ionised donors that originate from the defect gap states that tend to scatter the mobile carriers. Zinc oxide is found to naturally grow as oxygen deficient and therefore it is n-type carriers [4].

It has been established that the zinc oxide polar material demonstrates differences between the samples grown with O-polar or Zn-polar surfaces. Specifically, they include structural density defects that influence the absorption of the impurities and thus the precise optically states that are active and normally associated with the O-polar surfaces [5-8], Figure (5-1) [9].

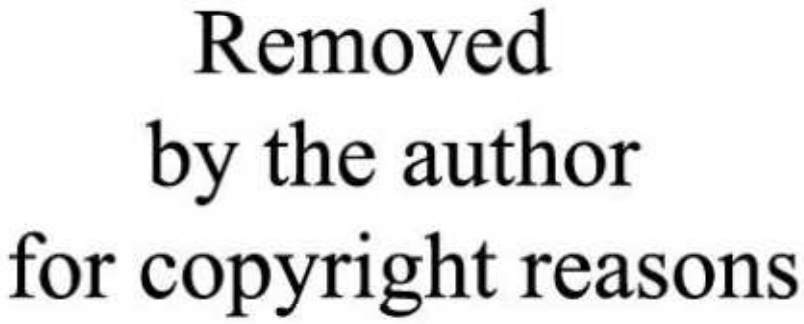

Figure (5.1): A hexagonal wurtzite crystal structure of ZnO contain of alternating zinc (Zn) and oxygen (O) atoms. The polar surface (0001) of ZnO is either Zn or O terminated. Figure taken from [9]

Polar films of zinc oxide are used in hetero junctions, enhancement of the piezoelectricity and also in catalysis. It is therefore, important to clarify the influence that O- or Zn-termination has on gap states for the films [10-12].

The results also indicate that the number of applications is found to increase rapidly when the doped ZnO is considered. Specifically, it has been established that the ZnO conductivity increases rapidly when it is doped with Al (AZO) or the Ga ions, which is cheaper and also more bio-compatible that indium tin oxide ITO [13], for use as photocurrent detectors [14-15]. Since pure ZnO has a band gap which is below the band gap of ITO, hence, it increases after Al doping [16]. Doping with TM, mean

while, has been found to produce many cases of ferromagnetism at room temperature. Oxygen vacancies are necessary but the magnetism is enhanced by increasing the carriers' number, by the co-doping with on Al or Ga [17-19].

There has been an increased interest among researchers in the use and application of the ZnO, InGaZnO and the ZnCoO, all of which are crucial to achieve resistive switching [20-22]. Their effects are considered to be dependent on the oxygen vacancies, which means that the technique used in measure the energy states that is associated with these oxygen vacancies are particularly crucial [20, 22].

Furthermore, the states in the gap are crucial for many applications and they may be measured by the photoluminescence (PL), which is often used to measure energy states. Research illustrates that this technique is not usually available with ZnO, since the photoluminescence (PL) is found to be quenched through the dopant transition metal or the Al ions [23-24]. In addition, measuring the gap states by measuring their direct absorption is difficult, because this is normally masked by the scattering due to crystalline imperfections and surface roughness.

In this chapter, we will illustrate the use of magnetic circular dichroism (MCD) in the detection of the weak absorption processes that are observed in thin films of zinc oxide [1]. MCD measures the absorption difference between left and right circularly polarised light which is both insensitive to scattering and suitable for samples that have quenched luminescence, such as doped ZnO films.

5.3 Magnetic Circular Dichroism Spectra in ZnO.

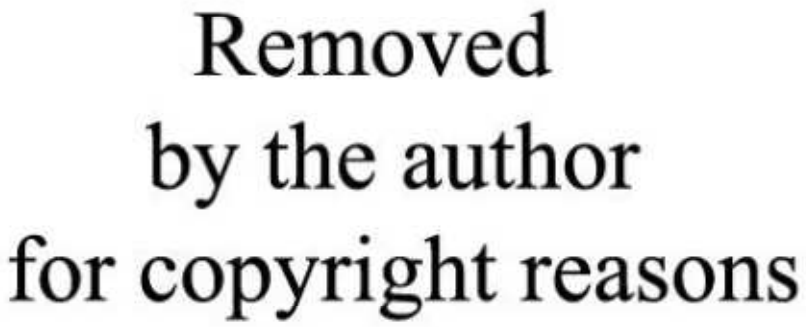

Figure (5.2): ZnO Bulk-band structure, where standard pseudopotential (SIC-PP) used for calculation. The horizontal dashed lines shown the width of the d-band and measured gap energy. Figure is taken from Ozgur et al [2].

In this section we will focus on the ZnO possible transitions with point defects. As shown in Figure (5.2) bulk ZnO has an empty conduction band and a full valance band and, the energy gap is about 3.4eV at room temperature [2]. We are interested in the states that occur in this gap due to defects, particularly states due to oxygen vacancy. The lowest state of energy for a neutral oxygen vacancy is found to be a spin singlet which is a deep donor, also another spin triplet is still within the energy gap [19]. The great number of vacancies, inside the grains, are found to be singly ionised paramagnetic states, however [25].

For all these cases, there is a broad energy range because of the lattice relaxation of the medium and the fact that the depletion regions are located close to the grain boundaries. There are also extensive defect states that are normally associated with the depletion layer and which are contained within the grain boundaries and become spin polarised, allowing them to accepts extra electrons when a magnetic field applied.

Optical absorption and MCD spectra are also expected to arise from shallow Al donors if they are only able to bind a single electron [1]. When a magnetic field is applied, all the electronic states are splits according to the order of $\mu_B|B|$ energies in the material, hence unequally population of the spin states, leading to an induced magnetisation. In many cases, a sample may show an MCD signal due to a small concentration of paramagnetic centres when the overall bulk susceptibility is diamagnetic. For a nonmagnetic material at RT the states have a small imbalanced population with an order of 10^{-3} in a magnetic induction of 1.8T , as used for our films, making the MCD signal weak, but still observable [1].

Diamagnetic MCD spectra are dispersive in the energy range of about $\mu_B|B|$; and since the induction that is used for the given experiments $\approx$ 1.8T, correspond to the specified energy which is of the order 10^{-4}eV. This is smaller than the resolution for the equipment used that ranges within 10^{-2}eV, hence the diamagnetic signal cannot be observed through our measurement [1]. The diamagnetic MCD spectra produced can also be observed through the large value for |B|, which is the only signal that is associated with the transition that occurs when an electron is transferred from levels that are completely full to completely empty levels. A large value of B is needed, however, or a more sensitive detection system, if this is to be observed [1].

When the transitions contribute just to the absorption but not to the observable MCD, they are called ‘silent’ transitions, as is in figure (5-3)(a) demonstrates the transition that occurs to the ionised Al donor states, while (b) illustrates the conduction band transitions, which occur within the singlet state for the neutral oxygen vacancy. The excitation experienced from the triplet state in the oxygen vacancies of the conduction band, meanwhile, provide a state that is partially ionised as shown in figure (5-3)(c). Figures (5-3)(d)-(f) illustrate the possible transitions that can be observed from a defect state that is singly occupied [1]. The partially ionised state shown in figure (5-3)(d) is similar to our results presented in this chapter for a singly occupied oxygen vacancy.

Figure (5.3): Schematic diagram for ZnO possible transitions. (a) Shows the MCD silent transitions to an ionised Al defect which occur from the valance band. (b) Also shows the MCD silent transitions like (a), but this time the transitions to the conduction band is from a spin singlet oxygen vacancy. (c) Observed MCD signal for a transition from the oxygen vacancy triplet state to the conduction band. (d) MCD signal for an occupied defect state with a single ionisation (e) MCD signal for a transition to the singly occupied oxygen state from the valance band, which guides to a defect singlet, and finally (f) MCD signal for a transition to the oxygen defect triplet [1].

If the zinc oxide has been heavily doped with Al, another contribution is noticed due to the existence of a significant number of degenerate electrons in the conduction and impurity bands. A finite MCD will occur for transitions from the valance band if the density of final states in the conduction band is spin dependent [1]. In the case of the occupations denoted by n_0, which is low, so the Boltzmann statistics are used so the MCD ~ $n_o\mu_B B/ k_B T$, and when the conduction electrons being degenerate the MCD ~ μ_B BG (E_F) ~ $Bn_0^{1/3}$ [1].

There are also other transitions that could occur around grain boundaries in the defect states. Hence, in ZnO, the grain boundaries have a conducting layer and also a high number of the singly ionised defects of oxygen [25]. These conducting layers can be responsible for the magnetism in the undoped films, since it originates from the spin splitting of the electronic states in the layers [1, 25].

5.4 Present Work:

5.4.1 Thin Films Preparations Techniques.

Two different types of films have been used in this chapter. ZnO polar films grown by MBE and ZnO films, with and without doping with Al, grown by PLD. Table (5.1) provides a summary of the growth method and thicknesses for the samples that have been used in this chapter.

Samples	Growth method	Deposition time (second)	Thickness (nm)	Energy Gap (eV)
O polar ZnO	MBE	-----	400	----
Zn polar ZnO	MBE	----	400	----
ZnO	PLD	40	155	3.4
1%Al doped ZnO	PLD	40	380	3.6
1%Al doped ZnO	PLD	60	430	3.7
1%Al doped ZnO	PLD	70	660	3.6
2%Al doped ZnO	PLD	40	310	3.7

Table (5.1): Summary of the prepared samples by MBE and PLD.

5.4.1.1 Molecular Beam Epitaxy MBE Technique.

Molecular beam epitaxy MBE technique was used by Dr.Ying, at the Key Laboratory of Beam Technology, Beijing Normal University in China to grow two polar ZnO films, as shown in table (5.1) [1]. The films were grown on sapphire substrates following degreasing with chloroethylene and acetone and then deionized water have been used to rinse it. The films were grown using a radio-frequency plasma-assisted system (Ommi Vac) with radical sources, such as Zn which had been evaporated by Kundsen cell (Veeco), and oxygen atoms produced by an rf-plasma system (SVTA).

A three unit cell with an (~10 nm) thick buffer layer of MgO rock salt was used to grown the Zn-polar ZnO films. While, for O-polar ZnO films a strained rock salt with layer thickness of (~ 0.5 nm) and an ultra-thin layer of MgO was employed to grow the films. At low temperatures of around 450^{o}C, an additional ZnO buffer layer of 10nm thickness was deposited, before the high temperature deposition of the 400 nm thick ZnO epilayer for both films [1, 26]. (Zn and O) polar terminating films were grown to investigate the possible types of defects associated with their growth.

5.4.1.2 Pulsed Laser Deposition PLD Technique.

All the targets used to grown (ZnAl)O thin films by PLD were prepared in the group's laboratories at the University of Sheffield (UoS). All powders were purchased from Alfa Aesar, hence the purity of the ZnO powder was of 99.9995%. A stoichiometric amount of each powder was weighed appropriately and mixed together using the following this percentages: $Zn_{1-x}Al_xO$ where (x= 1 and 2) % of Al_2O_3.

The mixture was then ground together three times for 20 minutes each by using a pestle and mortar as mentioned in chapter **3.2**. The first sintering of the mixture was performed in air furnace for ~ 12 hours at 400^{o}C annealing temperature. Then, after grinding for another 20 minutes, the target was annealed again at 600^{o}C for ~ 12 hours. The final annealing of the mixture as a powder was at 900^{o}C, again for around 12 hours. After that, the final powder was compressed in a vacuum to a pressure of 25000 kPa resulting in a cylindrical pellet with 25 mm diameter, which was then sintered for the last time at around 900^{o}C for 13-15 hours. More details are given in chapter **3.2.**

An XeCI Excimer laser with 308nm wavelength and pulse energies up to 400mJ, was used to synthesise thin films with various thicknesses on c-cut sapphire substrates at a temperature of 450^{o}C for the different ablation times of 40, 60 to 70 minutes as shown in the table (5.1), and at an oxygen pressure range of (1- 3 x10^{-5}) Torr within the chamber in order to grow oxygen deficient films.

5.4.2 Experimental Results

The following section presents the MCD and absorption spectra of the films. The energy spectra for MCD and absorption were taken in a range between 1.7 and 4.5 eV. A monochromator with a photo detector, together with a xenon lamp, were used to measure the transmission spectra. The loss coefficient α was obtained from the intensity lost in the film. The loss coefficient is a combination of the real absorption plus scattering from the grain boundaries in the films also scattering from the front and back surfaces of the film [1].

The MCD measurements were performed at room temperature in order to measure the Faraday rotation and ellipticity of the MCD simultaneously in an applied magnetic field of 1.8T. A pair of polarisers and a photoelastic modulator were used to take the MCD spectra for $1.7 < E < 4.5$ eV [1, 27]. All the MCD data presented in this chapter were obtained for a weakly absorbing film, to enable the detector to record the intensities and prevent the data ,in both Faraday and MCD channels, falling to zero [1].

5.4.2.1 MCD spectra of O-polar Films fabricated by MBE

The two O-polar and Zn-polar films were grown on a substrate that is a single-side polished, this cause a large amount of scattering from the substrate back side in below the band edge, hence the weak absorption spectra could not be measured accurately. The O-polar films have previously been found to have defects more than the Zn-polar films, in contrast with our films which showed an enhanced crystalline quality for the O-polar films. The film quality was deduced from the sharpness of the edge seen in the O-polar films above the band edge of 3.34eV as seen in earlier work [5-8].

The data in Figure (5-4) shows that the loss coefficient α is small for ZnO and but increases weakly with energy until the band gap at 3.32 eV is reached [28].

Figure (5-4): The absorption, α, for the O-polar and Zn-polar ZnO films.

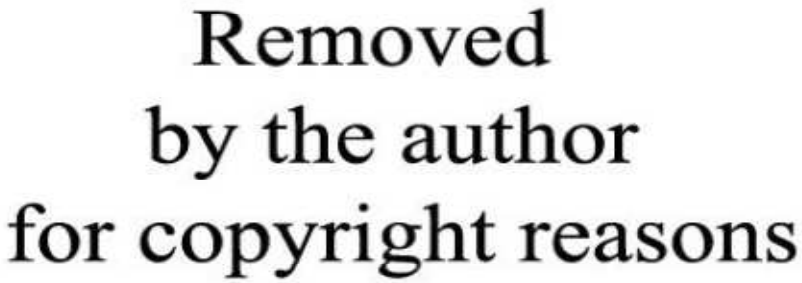

Figure (5-5): (a) The MCD spectra for 400nm thickness O-polar and Zn-polar ZnO films, grown by MBE. (b) The MCD spectra of the sapphire substrate [1]. The MCD measurements were undertaken in our group laboratories at the University of Sheffield (UoS).

Figure (5-5a) shows the MCD spectra which were done at the UoS for 400nm O-polar and Zn-polar ZnO films, grown on sapphire substrates by MBE. The signal from the substrate has been subtracted from the presented MCD data. As seen in the figure (5.5a) the MCD spectra for both films were rather flat, however, it is larger for the Zn-polar films with slow increase in the energy range in between $1.8 < E < 3$ eV, demonstrating the increase of the defects density near the band edge.

The MCD spectra for the O-polar film have a very shallow maximum at around 2.5eV which contrary with the 'green line' seen in the PL spectrum where it has a broad emission band at the same energy 2.5eV with a width of around 0.5eV [19, 23, 25]. The Zn-polar films have significant magnetic active gap states, which concluded from the larger MCD signal. The spin processes as described in figure (5.3d-f) with a singly occupied oxygen vacancy state and figure (5.3c) with the triplet state in their initial state, all occur in these polar films [25]. Figure (5.5b) shows the very small MCD spectra for sapphire substrate about 0.004 in (degree/cm) compared to 0.2-0.4 for ZnO, which is an MCD feature for wide band gap materials like sapphire ~ 8.7eV.

5.4.2.2 MCD Analysis of (ZnAl)O Films fabricated by PLD.

Figure (5-6): Data for PLD growth films of ZnO and (ZnAlO). (a) Illustrate the absorption α for all films with different thicknesses. (b) The corrected MCD data [1].

Figure (5-6 a and b) shows the absorption and MCD data were taken at the UoS respectively, for one pure ZnO film and the 1% (ZnAl)O films with various thicknesses and for one 2% (ZnAl)O film, with all films being grown by PLD. The purpose of preparing these samples was to investigate the defect states in nonmagnetic ZnO and (ZnAl)O films using MCD, which is a sensitive method to differ between transmission loss due to absorption and scattering. I will start by discussing the absorption results then the MCD results for all films.

From the absorption data the band gaps for all films grown by PLD were calculated by using Tauc plots more details of which are provided in chapter 3, and the energy gap Eg (eV) are given in the insert shown in figure (5.6a). The absorption spectra shown a

fast increase for pure ZnO below the band gap compared to the (ZnAl)O films, which is an indication of a better film quality [24, 29].

The donor states formed by adding Al to ZnO are easily ionised to give a carriers with a high density at room temperature within the conduction band. This causes the band edge to move from 3.5 eV to ~3.65 ± 0.05 eV, because of the Burnstein Moss effect [5, 8, 29]. There is unusual behaviour for the band gap of the 1% Al films with 430nm thicknesses, which does not follow the expected increase with thicknesses, as the energy gap for the 430nm film does not lie between the energy gaps for the 380nm and 660nm films as would be expected.

Further evidence for the deterioration in the film quality after doping with Al is clear from the data for the 2%Al film with 310nm thicknesses, which shows the largest energy loss of $\alpha \sim 0.05 cm^{-1}$ below the band gap.

In the following paragraphs I will start to discuss the MCD results for all films prepared by PLD as shown in figure (5.6b).

Similar spectral behaviour for the MCD of the pure ZnO films can be seen in figure (5.6b) and the O-polar film in figure (5.5a) per unit thickness. The measured signal from the polar film was bigger than the pure ZnO film because it is thicker, 400nm compared with 155nm for the PLD film. The MCD shows an overall small positive behaviour above the low energy range, but a small negative region can also be seen near the band edge. This negative region is caused by the transitions to the split band states created by an applied magnetic field [14-15].

In addition, the magnetically polarized states for the ZnO film have an approximate stable density of states in the band gap; although this depends on the number of defects in the film, which is smaller for O-polar films than for the PLD films.

The MCD spectrum for the three 1%Al doped with ZnO films with various thicknesses is also shown in figure (5.6b). The MCD signal at low energy has a small positive behaviour in (ZnAl)O films containing 1% Al doping compared to the positive MCD spectra that dominated in pure ZnO. The elimination of the positive MCD signal is caused by the Al doping, which provides electrons to the partially occupied gap states of the oxygen vacancy, thereby causing the MCD signal by changing the states to doubly occupied states that are nonmagnetic. As mentioned earlier in the chapter the data shown in figure (5.3d) illustrates that the single occupied defect state transition, observable by the MCD for a single occupied oxygen vacancy, but not observed for an Al donor, since this has a much smaller energy < 0.01eV in that case, which is not accessible to our apparatus. The MCD signal for $E < 2.6$eV is reduced strongly by the additional carriers provided by small concentration of Al. This emphasises the fact that oxygen vacancy alone could play the main role in enhancing the magnetism in ZnO, whereas the effect of the aluminium donors enhances the magnetism only in the presence of oxygen vacancies [18]. The partially occupied Al donors form a polarised impurity band that causes the strong negative signal starting from above 2.6eV up to the band edge.

The MCD spectrum for the 2%Al doped with ZnO film with a thickness of 310nm is also shown in figure (5.6b) and demonstrates a slightly bigger positive MCD signal at low energy than the 1%Al doped with ZnO films. This positive signal is caused by the additional singly ionised oxygen states due to the doping with 2% of Al, which increase the density of grain boundaries. While the negative MCD signal starts from around 2.6eV up to the band edge from the Al impurity band, in comparison to the PL result, we noticed that doping with Al reduced the intensity at around 2.2eV of the PL signal, whereas the signal for our 2% Al doping film was partly enhanced [24,25].

5.5 Conclusion.

- MCD is a very powerful technique that gives information about the magnetic polarisation of the states for magnetic materials. In this chapter we show that it is also a sensitive technique to determine weak absorption in non-magnetic material in a magnetic field and also to assist in the characterisation of the gap states.
- Both the MCD and PL techniques could work together in the investigations of gap states. The PL technique is usually less available, however, because the PL spectrum will be quenched by Al ions or dopant transition metal.
- For the two polar ZnO based films, we concluded that the O-polar films contained fewer spin polarised gap states than the Zn-polar film, which was an unexpected outcome. The spin polarisable states are shown as the broad signal in the MCD spectra at a big energy range.
- A similar MCD spectrum was seen in the case of the O-polar film figure (5.5a) and the pure ZnO films in figure (5.6b) per unit thickness.
- All three 1%Al doped with ZnO films showed a weak positive MCD signal at low energies which is due to full polarized gap states by the additional electrons from the 1%Al doping.
- Increasing the Al concentration has reduced the mobility of the mobile carriers scattering within the charged states. Hence MCD is a powerful technique to determine the source of scattering in ZnO:Al films, and also to detect the presence of singly ionised oxygen vacancies in ZnO.

- Increasing the Al concentration has indeed increased the band gap, however this variation with thicknesses was not applicable for all our 1% Al films, because unusual behaviour was seen for the 430nm film.
- A very weak positive MCD signal was detected for the sapphire substrate at energies above 2.4eV, which is very far from the sapphire band gap at 8.7eV.
- We expect that MCD will be used in many weakly absorbing transparent materials in the visible region.

5.6 References

[1] M. Ying, et al., "ZnO gap states investigated using magnetic circular dichroism," Journal of Physics D-Applied Physics, vol. 48, p. 255502, (2015).

[2] U. Ozgur, et al., "A comprehensive review of ZnO materials and devices," Journal of Applied Physics, vol. 98, p. 041301, (2005).

[3] Sze. S .M, Semiconductor Devices Physics and Technology vol. 2nd edn. New York: Wiley, (2002).

[4] B. B. Straumal, et al., "Magnetization study of nanograined pure and Mn-doped ZnO films: Formation of a ferromagnetic grain-boundary foam," Physical Review B, vol. 79, p. 205206, (2009).

[5] S. Lautenschlaeger, et al., "Asymmetry in the excitonic recombinations and impurity incorporation of the two polar faces of homoepitaxially grown ZnO films," Physical Review B, vol. 77, p. 144108, (2008).

[6] T. Nakamura, et al., "Near-surface structure of polar ZnO surfaces prepared by pulsed laser deposition," Thin Solid Films, vol. 559, pp. 88-91, (2014).

[7] J. Williams, et al., "Polarity-dependent photoemission spectra of wurtzite-type zinc oxide," Applied Physics Letters, vol. 100, p. 051902, (2012).

[8] D. C. Oh, et al., "Comparative study of photoluminescences for Zn-polar and O-polar faces of single-crystalline ZnO bulks," Applied Physics Letters, vol. 93, p. 241907, (2008).

[9] http://www.edn.com/design/led/4391796/2/White-LEDs-Printed-on-Paper-A-Doctoral-Thesis-Part-I.

[10] H. Tampo, et al., "Two-dimensional electron gas in Zn polar ZnMgO/ZnO heterostructures grown by radical source molecular beam epitaxy," Applied Physics Letters, vol. 89, p. 132113,(2006).

[11] Z. L. Wang, "ZnO nanowire and nanobelt platform for nanotechnology," Materials Science & Engineering R-Reports, vol. 64, pp. 33-71, (2009).

[12] B. Meyer and D. Marx, "Density-functional study of Cu atoms, monolayers, films, and coadsorbates on polar ZnO surfaces," Physical Review B, vol. 69, p. 235420, (2004).

[13] B. E. Sernelius, et al., "BAND-GAP TAILORING OF ZNO BY MEANS OF HEAVY AL DOPING," Physical Review B, vol. 37, pp. 10244-10248, (1988).

[14] A. Mahroug, et al., "Structural, optical and photocurrent properties of undoped and Al-doped ZnO thin films deposited by sol-gel spin coating technique," Materials Letters, vol. 134, pp. 248-251,(2014).

[15] T. Terasako, et al., "Carrier transport and photoluminescence properties of Ga-doped ZnO films grown by ion-plating and by atmospheric-pressure CVD," Thin Solid Films, vol. 549, pp. 12-17, (2013).

[16] Y. C. Yang, et al., "Giant piezoelectric d(33) coefficient in ferroelectric vanadium doped ZnO films," Applied Physics Letters, vol. 92, p. 012907,(2008).

[17] X. H. Xu, et al., "Carrier-induced ferromagnetism in n-type ZnMnAlO and ZnCoAlO thin films at room temperature," New Journal of Physics, vol. 8, p. 135, (2006).

[18] S. F. Qi, et al., "Carrier-mediated nonlocal ferromagnetic coupling between local magnetic polarons in Fe-doped In2O3 and Co-doped ZnO," Physical Review B, vol. 84, p. 205204, (2011).

[19] F. Leiter, et al., "Oxygen vacancies in ZnO," Physica B-Condensed Matter, vol. 340, pp. 201-204, (2003).

[20] W.-Y. Chang, et al., "Unipolar resistive switching characteristics of ZnO thin films for nonvolatile memory applications," Applied Physics Letters, vol. 92, p. 022110, (2008).

[21] M.-S. Kim, et al., "Effects of the oxygen vacancy concentration in InGaZnO-based resistance random access memory," Applied Physics Letters, vol. 101, p. 243503, (2012).

[22] G. Chen, et al., "Resistive Switching and Magnetic Modulation in Cobalt-Doped ZnO," Advanced Materials, vol. 24, pp. 3515-3520, (2012).

[23] S. Yamamoto, "Photoluminescence quenching in cobalt doped ZnO nanocrystals," Journal of Applied Physics, vol. 111, p. 114307,(2012).

[24] Y. Liu and J. Lian, "Optical and electrical properties of aluminum-doped ZnO thin films grown by pulsed laser deposition," Applied Surface Science, vol. 253, pp. 3727-3730, (2007).

[25] J. D. Ye, et al., "Correlation between green luminescence and morphology evolution of ZnO films," Applied Physics a-Materials Science & Processing, vol. 81, pp. 759-762, (2005).

[26] Z. Liu, et al., "Polarity-manipulation based on nanoscale structural transformation on strained 2D MgO," Journal of Physics D-Applied Physics, vol. 47, p. 105303, (2014).

[27] K. Sato, "Measurement of Magneto-Optical Kerr Effect Using Piezo-Birefringent Modulator," Japan. J. Appl. Phys, vol. 20pp. 2403-2409, (1981).

[28] M. Ying, et al., "Surface-polarity-dependent ferromagnetism in arsenic-implanted ZnO films prepared by MBE," Materials Letters, vol. 144, pp. 12-14,(2015).

[29] B.-Z. Dong, et al., "Effect of thickness on structural, electrical, and optical properties of ZnO : Al films deposited by pulsed laser deposition," Journal of Applied Physics, vol. 101, p. 033713, (2007).

Chapter 6

Magnetic and Magneto Optical Properties of ZnCoO and ZnCoAlO Thin Films

6.1 Introduction

Diluted magnetic semiconductors (DMS) in recent time have attracted a great deal of interest especially after focusing on the possibility of combining semiconducting capability with magnetic storage. DMS is one of the best candidates to be utilized in Spintronics, due to the possibility of combining the carriers charge in addition to the spin of carriers in understanding electronic functionality [1-3]. Zinc oxide is one of the most important elements in the DMS family, due to its unique properties. ZnO has a wide band gap that is ~ 3.37eV at 300K, it is transparency in the visible region makes it very favorable and useful in several optical applications such as solar cells; it also a high exciton binding energy ~ 60meV [4]. To obtain room temperature ferromagnetism, ZnO has been doped with small percentages of various transition metals such as; Mn, Fe, Co, V, Cr, and Ni. However, it is still controversial whether the observed ferromagnetic signal entirely rises from the nanophases blocked of particles or is a bulk property [3, 5]. As well as ongoing work to determine the origin of the ferromagnetic signal with a Curie temperature above RT, there are many other line of research that are

seeking for other ways to improve the magnetic properties such as the coercive field and remanence [5-6].

This chapter will describe the results of a sequence of studies of the magnetism and magneto-optic properties measurement on Co-doped ZnO and Co-doped Al-ZnO laser ablated thin films. In order to clarify the effects of using different preparation methods for films on the magnetic properties.

We investigate the effects of including Al to the target, changing the preparation of the target, annealing the target in various temperatures and varying the film thickness. We aim to discover the best method to grow thin films with a larger cohesive field and a usable remanence at room temperature. The results presented in this chapter are analysed to determine the contribution of Co metal nanoparticles to the magnetism. We also study an oxide sample, which does not include any metallic inclusions to any measurable extent [6-7].

Several groups have previously studied the origin of ferromagnetism in the ZnCoAlO and ZnCoO, this work is summarized in the next section. We compare and assess our results in comparison with the previous work. Some of the data presented in this chapter have been published [6, 8].

6.2 Literature Review

Experimental studies observed that room temperature ferromagnetism is found in oxides such as ZnO and TiO_2, doped with small percentages of transition metals TM [5]. A theoretical model by Dietl et al. of p-type TM-doped ZnO suggested that the hole-mediated interactions between doped TM ions scan produce

ferromagnetism at room temperature [9-10]. Experimentally n-type TM-doped ZnO systems have been found to show a ferromagnetism behavior [5, 11]. Several authors have shown that both the magnetization and the magneto-optic properties are enhanced by adding Al to ZnO, because it induces ferromagnetic coupling between Co nanoparticles within the ZnAlO matrix [6, 10-12]. The careful control of the aluminum doping and oxygen deficiency in n-type ZnMnO and ZnCoO are able to produce values for the ferromagnetic moments of $5\mu_B$ and $3\mu_B$ per transition metals TM ion respectively [11]. They also found that the free electrons inclusion produced by Al-doping is favorable. Thus, it gives rise to the magnetism in doped ZnO.

In spite of extensive studies on TM-doped ZnO to distinguish the origin of the ferromagnetism, the subject is still controversial. Also in the case of Co-doped ZnO system, the studies are still ongoing to investigate whether metallic Co is the sole source of ferromagnetism in the ZnCoO film [6].

Clear magnetism has also been observed in films with high densities of defects but without any transition metals TM ions indicating the importance of crystalline defects [13-14].

The work of Kaspar et al. [15] found that epitaxial thin films of Co-doped ZnO that had a high structural quality has no significant room temperature ferromagnetism. They used PLD to deposit the films on c-plane and r-plan sapphire substrates [15]. They used several techniques for analysis; a vibration sample magnetometer (VSM) was used to measure the magnetic properties with the field applied in the plane of the film, X-ray photoelectron spectroscopy (XPS) and high-resolution transmission electron microscopy (TEM) techniques were used

to investigate the microstructure details of the films, which they used to show the absence of empty spin states near the conduction band. In addition, it was confirmed that there is no change in the electronic structure of the films as measured from the optical MCD spectra. Thus, the author's conclusion was that ferromagnetism in Co: ZnO films cannot be induced only by itinerant conduction band electrons, even when the fraction of the carrier concentration of the magnetic dopant concentration is significant [15].

Opel et al., grew $Zn_{0.95}Co_{0.05}O$ thin films by PLD at 400°C and 500°C using a KrF excimer laser (248 nm) at a repetition rate of (2 Hz) homoepitaxially on single crystalline ZnO substrates. They state that the observed ferromagnetism in Co: ZnO films arises from the metallic cobalt nano-inclusions[16]. The micro-structural analysis detailed was investigated by a high-resolution X-ray diffraction (HRXRD), transmission electron microscopy (TEM), and electron spectroscopic imaging. The films were studied magnetic by SQUID magnetometry, X-ray magnetic circular dichroism (XMCD) and AC susceptibility measurements. The hysteresis loops at 300 K and the ZFC/FC at 100 Oe as a function of temperature were measured by SQUID are shown in Figure (6-1) and are fitted very well by Langevin functions.

Figure (6-1): (a) Magnetization curves at room temperature from$Zn_{0.95}Co_{0.05}O$ thin films grown at 400°C (green squares) and 500°C (blue circles) with a magnetic field applied to parallel the film plane. Solid lines represent the fit to the Langevin function(b) Zero field-cooled (open symbols) and field cooled magnetization measurements (closed symbols), taken at 100 Oe as a function of temperature T. Figures are taken from Opel et al, [16].

The linear diamagnetic contributions from the substrate have been subtracted from the loops, data in Fig (6-1a) (corrected). As seen from the inset in Fig (6-1a) both samples show that, the remanent magnetization at 300K is close to zero.

Superparamagnetic particles in a ZnO matrix can be used to produce the measured magnetisation curves, as shown by the fit for the data to the Langevin function shown in Fig (6-1a). In addition, they measured the ZFC/FC magnetisation for both samples as shown in Fig (6-1b), where the difference between these measurements at low temperature indicates the presence of nano particles. The ZFC curves have a maxima at around 15 K and 38 K for the samples grown at 400°C or 500°C, respectively, hence, they can be interpreted to indicate the presence of different size blocked superparamagnetic metallic Co nanoparticles within a diamagnetic ZnO matrix [16].

X-Ray magnetic circular dichroism (XMCD) spectroscopy was used by Tietze et al., the origin of ferromagnetism in three different types of samples with 5% Co-doped ZnO. The films were prepared by PLD technique using KrF excimer laser with a wavelength of 248 nm. SQUID magnetometry and XAS measurements were performed to characterize the origin of the observed ferromagnetism in the films. They found that the XMCD signals from the Co, Zn and O ions indicated that all ion cores were paramagnetism. Therefore, they suggested that the oxygen vacancies as the origin for room temperature ferromagnetism rather than Co ions in doped ZnO [17].

Another study was performed by Neal et al., using magnetic circular dichroism (MCD) measurements to identify the ferromagnetism of ZnO doped with 5% Co thin film with 200 nm thickness grown by PLD with 10mTorr of O_2 pressures in the chamber [18]. Room temperature ferromagnetism has been detected from the SQUID measurements for the 5% Co-doped ZnO film and for the undoped ZnO

film, which was grown for reference. Figure (6-2) shows the MCD spectrum for both doped and undoped ZnO films at 10K, where both were grown on a *c*-cut sapphire substrate. The sapphire signal dominated the MCD signal for the un-doped ZnO, and the d-d transitions detected at 2eV for the 5% Co-doped ZnO. They concluded that the ferromagnetism of the sample is connected with the electrons in a defect band of ZnO which are polarized [18].

Figure (6-2): Compared MCD spectrum of an undoped ZnO film to that of $Zn_{0:98}Co_{0:02}O$ film, both grown on a c-cut sapphire substrate. Both sets of data were taken at 10 K in a field of 0.45 T. The arrows indicate the d-d transitions at 2 eV and the feature at the ZnO band edge at3.4 eV for the $Zn_{0:98}Co_{0:02}O$ film. Figure is taken from Neal et al, [18].

Heald et al, [19] studied two sets of ZnCoO films that were grown by PLD in two different laboratories. The first sets of films were deposited using an off-axis PLD configuration, utilizing a KrF excimer laser with wavelength of 248 nm with a repeated rate of 1–5 Hz. The films were annealed in Zn vapor at 600 °C for 5 h. and showed an n-type conductivity and weak room temperature ferromagnetism after the annealing, as expected [20]. This was compared to a film that showed lack of metallic cobalt Co (0), within the detection limit was confirmed by XANES and EXAFS measurements. Another set of films were epitaxial Co-doped ZnO deposited on single crystal c-plane sapphire (0001) and r-plane sapphire ($1\text{-}10^2$) substrates. The substrate temperature was at a 475–550°C in 10 mTorr O_2 [19]. Quantum Design SQUID magnetometer was utilized to carried out in Magnetization measurements. The morphology of the films observed the presence of secondary-phase Co metal particles which accounted for all the magnetic properties that they observed [20].

6.3 Present Work

6.3.1 Sample preparation

The samples used in this chapter were grown in our group laboratories in the University of Sheffield. A few of the samples described in this chapter were grown by two visitors, Dr Li from Key Laboratory of Magnetic Molecules and Magnetic Information Materials Science, Shanxi Normal University, China [6] and Dr. Ying from Key Laboratory of Beam Technology, Beijing Normal University, China [8]. The source of the samples will be mentioned throughout this section.

Different sets of targets were prepared at different conditions to grow thin films in order to investigate the possibility of producing thin films with high usable remanence and coercive field at room temperature and to provide a high concentration of carriers for exchange coupling to occur. All powders were purchased from Alfa Aesar had purities of 99.9995% for ZnO and 99.998% for Co metal. Accordingly, four sets of targets have been prepared using three different methods as follows:

Method 1: for targets;

I. The $Zn_{1-x}Co_xO$ (x= 5 and 10) % target.

II. The $Zn_{1-x-y}Co_x Al_yO$ (x= 5,10,15,20,25 and 30) %, (y=1%) target

For I and II targets, powders of ZnO and metallic Co and, where desired Al_2O_3 were mixed in a stoichiometric amounts as required. The mixture was then ground

together by using a pestle and mortar as mentioned in chapter 3.1 for 30 minutes, which it is better than the mechanical grinders in mixing the powder to get a hard target with a high density. The first grinding step was followed by sintering the mixture in air furnace for ~ 12 hour at 400^{o}C annealing temperature. Then, the same powder was reground for around another 30 minutes and annealed again at 600^{o}C for ~ 12 hour. The final annealing for the mixture as a powder was at 800^{o}C for around 12 hour too. After the final anneal, the powder was compressedin vacuum to a pressure of 25000 kPa into a target mould and sintered for the last time at around 1150^{o}C for 13-15 hours. The resulting target is a cylindrical pellet with 25 mm diameter, more details are given in chapter 3.1.This procedure was used to prepare both the ZnCoO and ZnCoAlO targets.

Method 2: for target;

III. The $Zn_{1-x}Co_xO$ (x= 5 and 10) % target.

The powders for this target were ground together once only for 30 minutes before compressing them to form a target mould, and then annealed for just one time for 15 hours at 1100^{o}C. The final target was used for laser ablation.

Method 3: for target;

IV. The $Zn_{1-x-y}Co_x Al_yO$ (x= 5 and 10)%, (y=1%) target.

The target preparation followed the procedure as in I and II. The only difference was that the desired percentage of metallic Co powder was added only to the mixtures in step three of the target preparation.

6.3.2 Experimental Results

All thin films were prepared by PLD, using an excimer Xe-Cl laser with a pulse-rate of about 28 ns, **as explained in Chapter. 3.** The films were ablated on to a c-cut sapphire substrate (0001) purchased from CrysTec GmbH at temperature of 400^{o}C for different times 4,8 and 16 minutes at base pressure of 10^{-5} Torr within the chamber; the substrate had been cleaned ultrasonically in methyl alcohol to remove any contaminants or dust before ablation. The distance between the substrate and the target in the PLD chamber was about 5cm through the ablation process, in order to achieve the constant deposition rate. The target holder was rotating at a speed of about 60 rpm during the growth process to reduce target drilling.

Films structural properties were measured by the use of near edge x-ray absorption and extended x-ray absorption fine structure (EXAFS) measurements were performed at the Advanced Photon Source using beam lines 20-ID-B [15] by our collaborator Dr. Steve M. Heald in the Argonne National Laboratory, for some of our films.

The SQUID magnetometer was used to measure the magnetic properties. The hysteresis loops of the films were measured in the temperature range of 5-300 K with magnetic field up to 1 Tesla applied in the plane of the film. ZFC/FC magnetisation measurements were also taken.

Magneto-optical measurements were carried out cover an energy range of 1.5-3.5 eV in Faraday geometry. Dektak was used to measure the thicknesses of the films described in this chapter. The structural, magnetic and magneto-optical data for all the films will be discussed in this chapter as seen in the following sections.

The percentages of the cobalt that was in the form of metallic cobalt that existed in the film was determined by near edge x-ray absorption, to demonstrate the source of the ferromagnetism in the film, whether it is from the effect of Co metal or it is intrinsic to doped ZnO and due to grain boundaries. We calculate the expected magnetisation from the metallic cobalt clusters at 5K assuming that all Co atoms in the metallic clusters carry the magnetic moment appropriate for the bulk metal of 1.7 μ_B per ion, as shown in the following formula in ($\mathbf{emu/cm^3}$):

Magnetusation from the cobalt metal is, $[(\boldsymbol{f})(\mathbf{x})(\mathbf{66.94 \times 10^{-3}})]$ .... (1.6)

Using; The molecular mass of ZnO is (81.4) and the density is (5.61 g/cm^3). Hence the number of Zn (f.u.) per cm^3 is $\frac{\mathbf{N_A \times 5.61}}{\mathbf{81.4}}$ = 0.415×$\mathbf{10^{23}}$, (N_A is Avogadro's number). This formula is used including that, f is the percentage of cobalt in metallic regions measured by EXAFS and *x* is the percentage of Co added to the target.

Content	Deposition time (minute)	Thickness (nm)	Metallic Co	Hc (Oe) 5 K	Hc (Oe) 300 K	Ms (emu/cm^3) 5 K	Ms (emu/cm^3) 300 K	M_S(300k) / Ms(5k)
$Zn_{0.94}Co_{0.05}Al_{0.01}O$ Method1 (II)	16	255±2	% 24 ± %3	67±50	40±20	44	36	0.832

Table (6-1): Summary of the magnetic measurements for $Zn_{0.94}Co_{0.05}Al_{0.01}O$

As an example of a film containing metallic Co we present details in table (6-1) for $\mathbf{Zn_{0.94}Co_{0.05}Al_{0.01}}$ films grown on a sapphire substrate for 4 minutes. It has a 5 % percentage of Co in the target of which 24% is in metallic cluster and has high magnetization of ~44 and 36 emu/cm^3 at 5, 300K ,respectively. Where 24% of metallic cobalt has been detected by EXAFS. The calculated saturation magnetisation at 5K due to metallic Co is ~8 emu/cm^3, which is much small than the measured magnetization. The magnetization that can be directly attributed to the metallic cobalt is found from equation (1.6):

$$\boldsymbol{M_{metal} = (f)(x)(66.94 \times 10^{-3}) = (24)(5)(66.94 \times 10^{-3}) = 8\ emu/cm^3} \quad \textbf{... (2.6)}$$

Therefore, we could conclude that the metallic Co has only a small effect on the magnetization in the film. Similarly, in all the films described in this chapter the direct contribution to the magnetization from the metallic Co itself is very small [6, 8].

However, it is noticeable that all films with high magnetization ≥ 30 emu/cm^3 actually contained some metallic Co. This suggests that there are some mechanisms by which the small clusters of metallic Co actually enhance the intrinsic magnetization of the films.

6.3.2.1 Discussion of MCD Results

As we mentioned in the previous chapters, MCD is a powerful technique were carried out to give extra information about the exchange coupling between the oxide magnetism and the Co nanoparticles. The MCD spectrum is known and been studied before as in [21].

Figure (6-3): The imaginary part of the off-diagonal dielectric tensor as a function of energy. The insert show the various relaxation times from 0.3 and 0.1. Figure taken from [21].

Figure (6-3) illustrates the result of the MCD spectrum as a function of energy, showing the behaviour of various relaxation time τ. Where it is clear from the plot that, as the reducing of the relaxation time, leads to decreases the shape of the dielectric function plot until it becomes a flat shape. The influences of two parameters are shown in the plot; the part of the spectrum from electron scattering in nanoparticles, which arises from the metallic particle, and fraction, determined the shape of spectrum. The strong negative peak between 2-3 eV as shown in figure (6-3) is evidence for metallic Co in the film [21]. Hence, a positive MCD spectrum is seen if the film has no metal effect on the magnetization.

On the other hand, if we have a film, which has small grains, then the MCD spectrum is large and positive but if it is also has metallic Co, we will expect a large negative spectrum. If the grain sizes are large and positive, it means the effect all from the grain, but if it is large and negative then it is smaller effect.

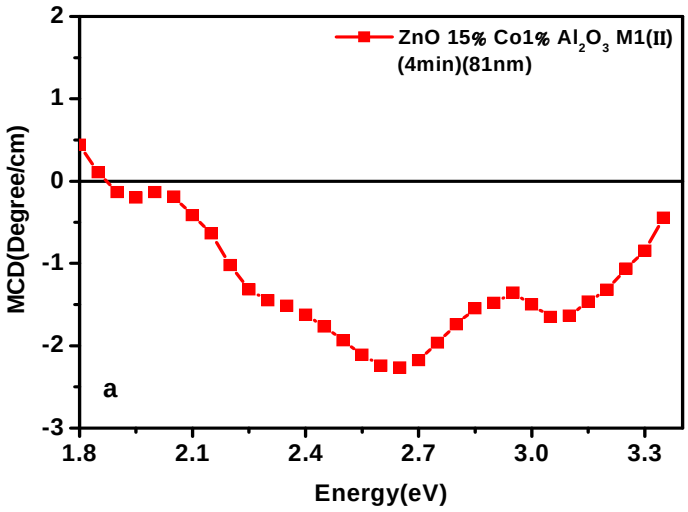

Figure (6-4): MCD spectrum for $Zn_{0.84}Co_{0.15}Al_{0.01}O$ film deposited for 4minute (81nm) using the same target prepared by M1 (II) method. The MCD signal indicates the effect of Co nano particles on the magnetization.

This is shown by the MCD spectrum for the film $\mathbf{Zn_{0.84}Co_{0.15}Al_{0.01}O}$ taken at room temperature in figure (6-4). This film contained 6% of metallic Co and had a rather small magnetization at 5K. If metallic cobalt and hence the magnetisation that could be attributed directly to metallic Co was 5.9 emu/cm^3 which was small compared with the measured value of 13.8 emu/cm^3. The large negative spectrum between ~ 2-3eV is a typical Co nanoparticles behavior as seen before in [21]. The ZnO band edge occurs at ~ 3.4 eV but it is raised by the presence of aluminum. There is also a dip, negative signal, near the band edge at around 3.1eV that can be related to the effects of the polarized carrier arising from the Al added to the film, and also because deposition was done at base pressure [22].

A positive MCD spectrum is seen when there is no detectable metallic Co observed in the film composition. Figure (6-5) shows the MCD spectrum deposited for 8 minute $\mathbf{Zn_{0.84}Co_{0.15}Al_{0.01}O}$ film, grown at base pressure with thickness of 160nm. There was no metallic cobalt detected from the near edge absorption measurements. The films shows a grain size of about 35nm, which is resulted in the small measured magnetization of 7emu/cm^3 at 5K by SQUID. The observed positive MCD is occurring from transitions originating spin polarised states associated with the film surfaces and the grain boundaries. It is similar to the signal that was identified to a transition from states bound at Zn vacancies for samples that were heavily oxygenated. In this case the samples were all grown at base pressure but it does look as if there are similar states at the surfaces of the grains [8].

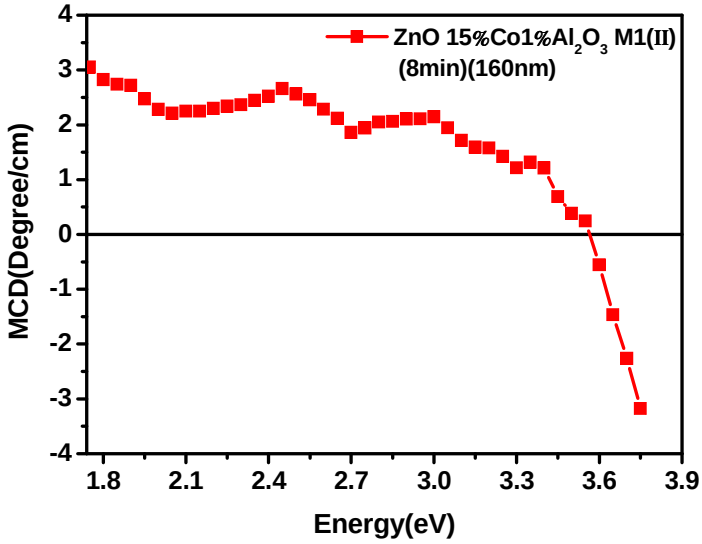

Figure (6-5): MCD spectrum for $Zn_{0.84}Co_{0.15}Al_{0.01}O$ film deposited at base pressure from a target prepared by using M1(II) method, showing a strong positive MCD. Grain size of the film is about 35nm

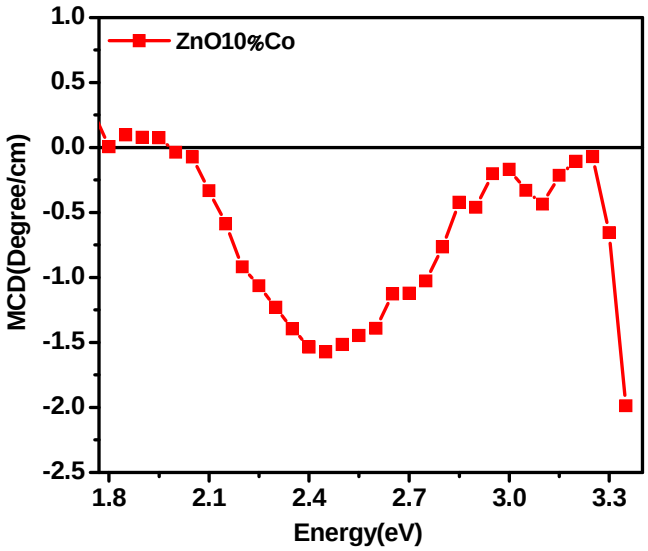

Figure (6-6): Room temperature MCD spectrum for $Zn_{0.90}Co_{0.10}O$ film deposited for 8minute (136nm). M1(I) was the target preparation method. Shows a negative MCD for a sample with no detected metallic cobalt.

Film $\mathbf{Zn_{0.90}Co_{0.10}O}$ in figure (6-6) where grown on a sapphire substrate for 8 minute at base pressure with thickness of 136nm. The target were prepared following method M1(I). A high saturation magnetization has been measured in the film of about 49±5 (emu/cm^3) at 5K, although there was no metallic cobalt detected in the film structure from the EXAFS. Therefore it is a good example for a sample showing a ferromagnetic behaviour with a negligible metallic cobalt [6].

In what follows we have found it useful to quantify the MCD by taking an average of the signal between 2eV and 3eV because this is the range where the signal from the grain boundaries is positive and that for the metallic cobalt is negative. Clearly, some samples have both a signal from the grain boundaries and also from cobalt nanoparticles and in this case the signal partially cancels

6.3.2.2 Measurement of Grain Size

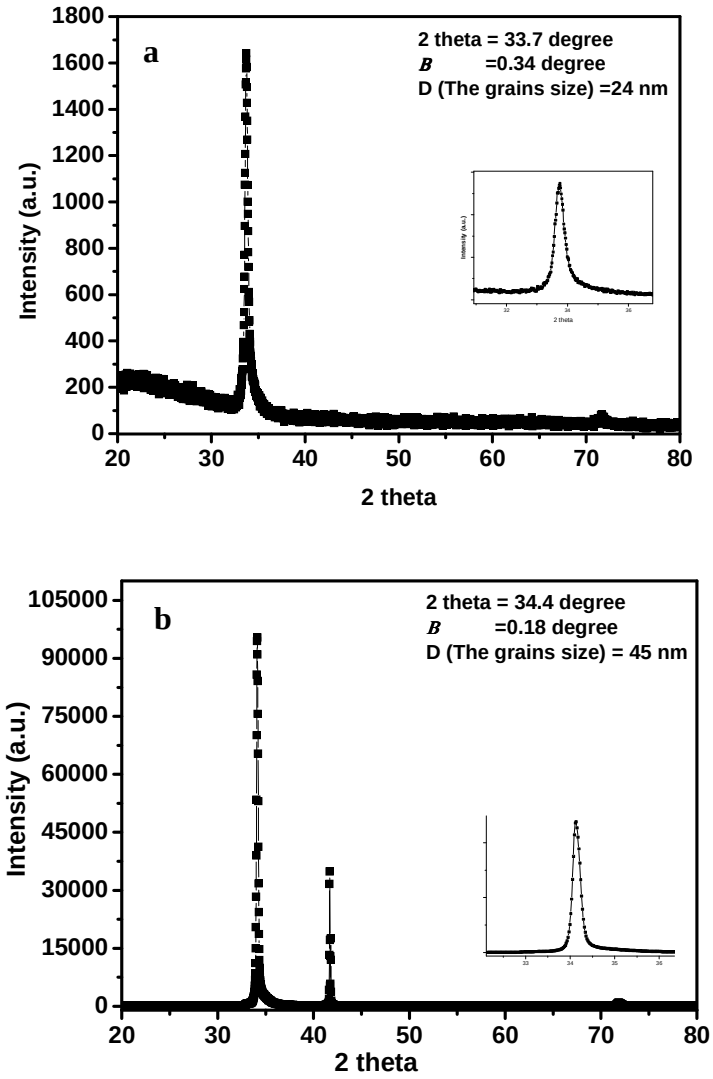

Figure (6-7): XRD patterns of the 2θ scan for, (a) 5% ZnCoAlO film with thickness of 46nm, 2θ ~ 33.7^{o}, and 4 minute deposition time. (b) is for 10% ZnCoAlO film with thickness of 312nm, and 2θ ~ 34.4^{o} and 16 minute deposition time. Both films were grown at 400oC and base pressure on a sapphire substrate at RT. M1(II) were used to prepare the target for (a) and (b).

The XRD results for all the films showed only a very well defined peak corresponding to a (002) reflection showing that the films were well oriented on the substrate with the z-axis perpendicular to the plane. The value of 2θ varied between 33.7^{o} and 34.4^{o} corresponding to a variation of the c-axis. The values of the grain size which been calculated by using Debye-Scherrer formula, as explained in chapter 4, is varies between 24nm and 45nm which is in the range where Straumal [23] predicts magnetism . Typical plots are shown in Figure (6-7 a and b) for the film doped with 5% Co, 1%Al and thickness 46 nm and the film doped with 10% Co and 1% Al and thickness 312nm, respectively, (a sapphire peak is also visible here).

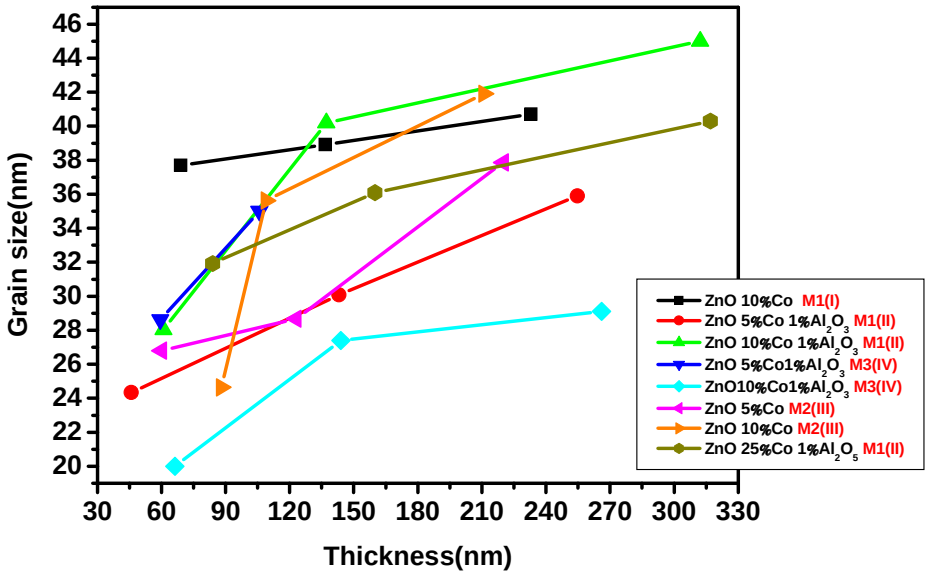

Figure (6-8): Grain size as a function of film thicknesses. Films details are shown in the insert.

For all the films that we made the grain size increased as the film thickness was increased as shown in Figure (6-8). The films with the smallest grains were the ones where the powders were only mixed and sintered once M2(III), or if the cobalt was included for only one sintering process M3(IV). Adding aluminum also seemed to give smaller grains.

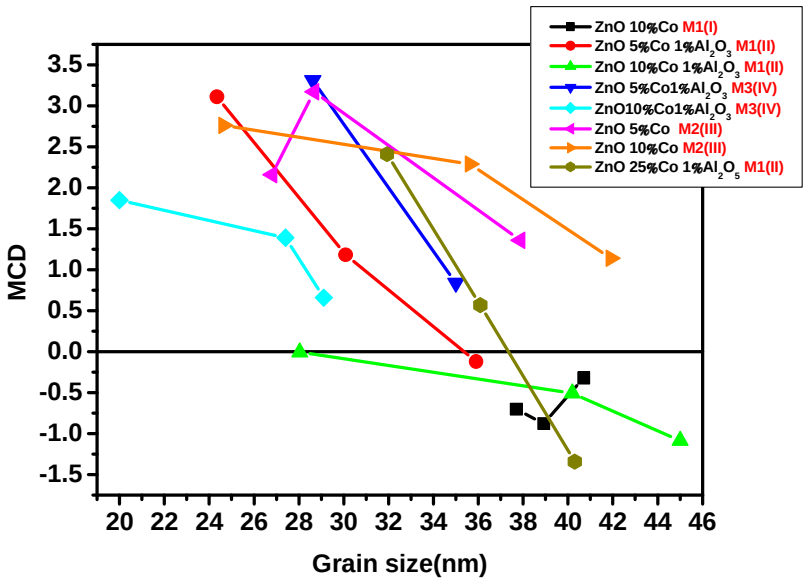

Figure (6-9): MCD value as a function of films grain size. Films details are shown in the insert.

As illustrated in figure (6-9) and (6-10) that the MCD is associated with grain size, since grain size depends on thickness, therefore we got thickness dependence. Small grain size and thinner film have shown a positive MCD signal, as seen in the last two figures. $\mathbf{Zn_{0.90}Co_{0.10}O}$ (black line) and $\mathbf{Zn_{0.89}Co_{0.10}Al_{0.01}O}$ (green line) both set of films showed a negative MCD behaviour due to the considerable amount of metallic Co, which have been detected by EXAFS for some of them.

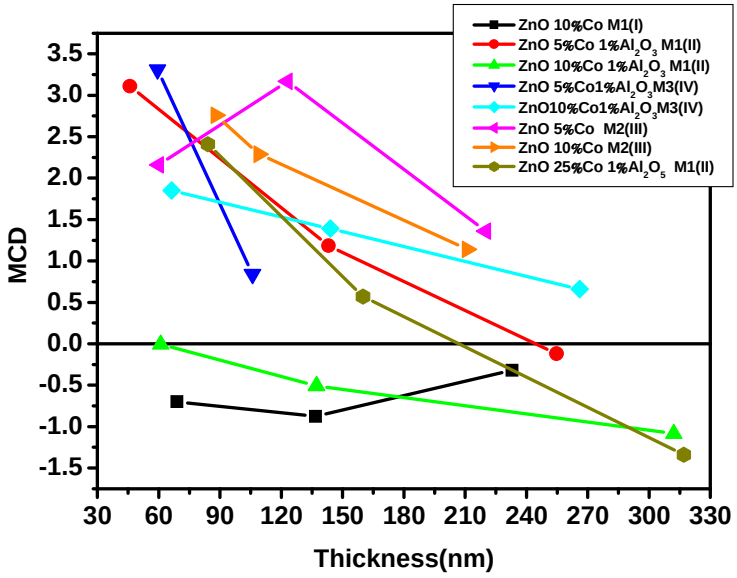

Figure (6-10): MCD value as a function of films thicknesses. Films details are shown in the insert.

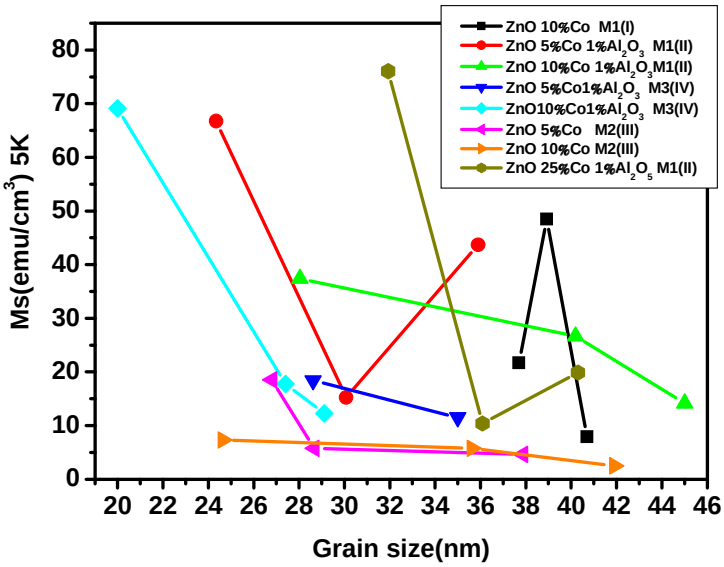

Figure (6-11): Magnetization value as a function of films grain size. Films details are shown in the insert.

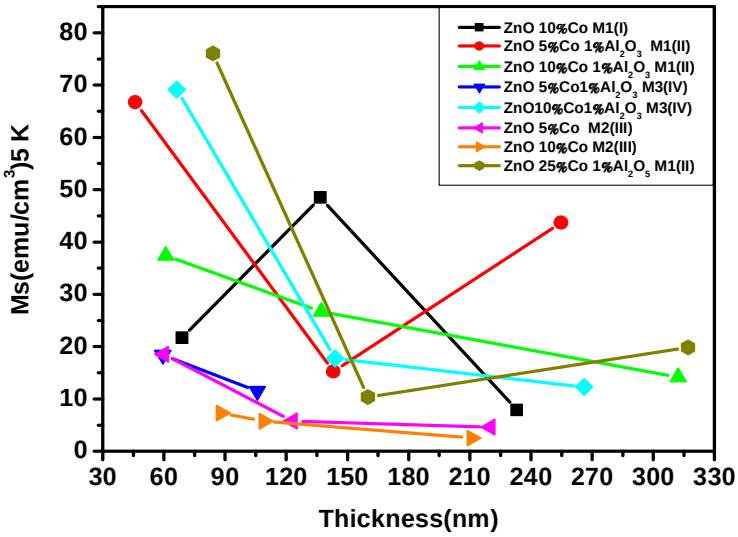

Figure (6-12): Magnetization value as a function of films thicknesses. Films details are shown in the insert.

Figure (6-11) and (6-12) illustrate the magnetization value as a function of films grain size and thickness, films details as shown in the insert. We consider if the measured saturation magnetisation at room temperature is correlated better with either the film thickness or the average size of grains. However this is not very clear because the grain size depends on thickness however the correlation does appear to be slightly better with the film thickness.

We can also compare the magnetisation of films with similar grain sizes and thickness to see which method of target preparation and composition gives the largest magnetisation. The method M2(III) gave consistently low magnetisation below ~15emu/cm^3. Those fabricated using M1(II) gave high (~60emu/cm^3) or medium (~35emu/cm^3) magnetisations however we got mixed results for M3(IV) because we got a high magnetisation with 10% cobalt but a low one with 5%.

We see that there is surprisingly little variation with the concentration of cobalt as the three films with the largest magnetisations had 5%, 10% and 25% cobalt and only two of them contained aluminum.

6.3.2.3 Magnetic Properties

To study the effect of target annealing on the film properties, for this purpose we compare the films prepared from two different 10% Co- doped ZnO targets. The magnetic properties are summarized in table (6.2). A $\mathbf{Zn_{0.90}Co_{0.10}O}$ thin film which was annealed at 1150^{o}C, and with a thickness of 136nm shows a very large magnetization of (40±5 and 49±5) emu/cm^3 at300K and 5K respectively. The second film is also made with 10%Co doped ZnO, but the target were annealed at lower temperature of 1000^{o}C. The first film is similar to film C in [6] that it is magnetisation is high.

Content	Annealing temperature (^{0}C)	Thickness (nm)	Metallic Co	Hc (Oe) 5 K	Hc (Oe) 300 K	Ms (emu/cm^3) 5 K	Ms (emu/cm^3) 300 K	M_S(300k) / Ms(5k)
$Zn_{0.90}Co_{0.10}O$ Method1 (I)	1150	136±2	~1	100±50	50±50	49±5	40±5	0.82
$Zn_{0.90}Co_{0.10}O$ Method1 (I)*	1000	131±2	% 9 ±3	800±50	165±50	13±1	9±1	0.84

Table (6-2): Summary of the magnetic measurements for $Zn_{0.90}Co_{0.10}O$ film 136nm, and $Zn_{0.90}Co_{0.10}O$ film 131nm, both films were grown for 8minute following M1(I) for targets preparation. The final sintering temperatures for the two targets were different, 1150^{o}C and 1000^{o}C, respectively. The film which marked * were grown by Dr Li at UoS [6]

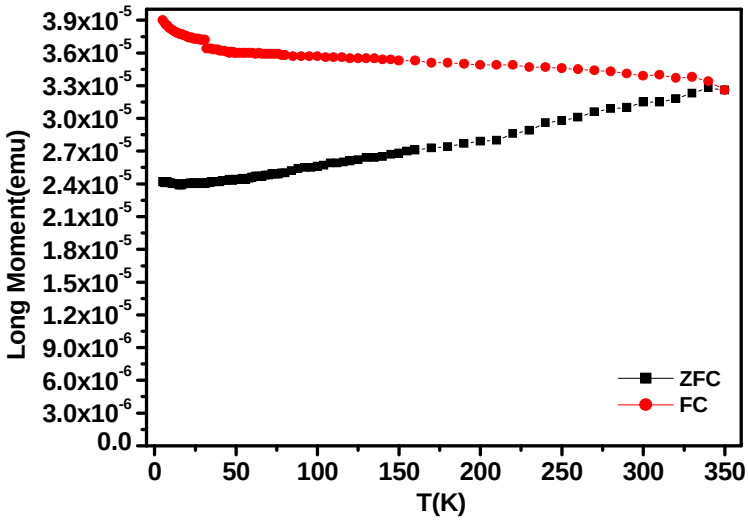

Figure (6-13): ZFC/FC magnetisations for $Zn_{0.90}Co_{0.10}O$ film measured in 100 Oe with field applied in the film plane. Film deposited for 8minut (136nm) film grown at 400°C. M1(I) was the target preparation method with sintering temperature at 1150°C.

Removed
by the author
for copyright reasons

Figure (6-14): Comparison ZFC/FC magnetisations for $Zn_{0.90}Co_{0.10}O$ film measured in 100 Oe with field applied in the film plane. Film deposited for 8minut (131nm) film grown at 400°C. The target sintering temperature was at 1000°C

Figure (6-13) and (6-14): show the ZFC/FC magnetisations for the two film measured in 100 Oe with field applied in the film plane. Both films were deposited for 8minutes at 400^{o}C growth temperature. The target for the film with 136nm thickness was annealed at 1150^{o}C, hence, the target for the film with 131nm thickness were cooked at 1000^{o}C. Large coercive fields are associated with cobalt nanoparticles where the size of the blocking temperature depends on the average volume of the nanoparticles. Some of the films made with the targets that had been sintered at 1150 ^{o}C had very significant concentrations of cobalt nanoparticles but small coercive fields. This implies that films made from targets that had been sintered at high temperature contained very small Co nanoparticles.

6.4 Conclusion

In this chapter we have performed a magnetism and magneto-optic measurement on Co-doped ZnO and Co-doped Al-ZnO thin films, thus to investigate the presence on nanoparticles in the doped films and their contribution to the observed magnetic and magneto optical results. The effects of different methods of film preparations in the magnetic properties seem to depend on one method to another; never the less adding Al to the target enhanced the magnetization.

We have found that grain size is important together with film thicknesses. Thus thin films with small grain size showed a big magnetization and a positive MCD signal.

Also $\frac{M(300K)}{M(5K)} \geq 0.9$ whereas films containing metallic cobalt frequently showed $\frac{M(300K)}{M(5K)} \geq 0.8$.

Films made from Co doped ZnO targets annealed at high temperature, seems to show a smaller nano particles than those made from targets sintered at lower temperature. Observable metallic nano partials showed a negative MCD signal, while the positive MCD signal is only a feature of grain boundaries. Some Co doped ZnO films demonstrated a considerable magnetization even with the absence of the metallic Co.

Large Hc at low temperature is due to large Co nano particles that occur for target sintered at lower temperatures. In general, the results were rather disappointed, as the aim was to prepare films with rather large Hc at room temperature.

6.5 References

[1] S. A. Wolf, *et al.*, "Spintronics: A spin-based electronics vision for the future," *Science*, vol. 294, pp. 1488-1495, (2001).

[2] M. Bibes and A. Barthelemy, "Oxide spintronics," *Ieee Transactions on Electron Devices*, vol. 54, pp. 1003-1023, (2007).

[3] U. Ozgur, *et al.*, "A comprehensive review of ZnO materials and devices," *Journal of Applied Physics*, vol. 98, p. 041301, (2005).

[4] C. Klingshirn, "Zinc Oxide From Fundamental Properties Towards Novel Applications Introduction," *Zinc Oxide: from Fundamental Properties Towards Novel Applications*, vol. 120, pp. 1-6, (2010).

[5] J. M. D. Coey, "Dilute magnetic oxides," *Current Opinion in Solid State & Materials Science*, vol. 10, pp. 83-92, (2006).

[6] Q. Feng, *et al.*, "Enhanced magnetic properties in ZnCoAlO caused by exchang-ecoupling to Co nanoparticles," *New Journal of Physics*, vol. 18, p. 113040, (2016).

[7] C. Clavero, *et al.*, "Interface effects in the magneto-optical properties of Co nanoparticles in dielectric matrix," *Applied Physics Letters*, vol. 90, (2007).

[8] M. J. Ying, *et al.*, "Advantageous use of metallic cobalt in the target for pulsed laser deposition of cobalt-doped ZnO films," *Applied Physics Letters*, vol. 109, (2016).

[9] T. Dietl, *et al.*, "Zener model description of ferromagnetism in zinc-blende magnetic semiconductors," *Science*, vol. 287, pp. 1019-1022, Feb 11 (2000).

[10] A. J. Behan, *et al.*, "Two magnetic regimes in doped ZnO corresponding to a dilute magnetic semiconductor and a dilute magnetic insulator," *Physical Review Letters*, vol. 100, p. pp: 047206, (2008).

[11] X. H. Xu, *et al.*, "Carrier-induced ferromagnetism in n-type ZnMnAlO and ZnCoAlO thin films at room temperature," *New Journal of Physics*, vol. 8, (2006).

[12] Z. Quan, *et al.*, "Enhanced Room Temperature Magnetoresistance and Spin Injection from Metallic Cobalt in Co/ZnO and Co/ZnAlO Films," *Acs Applied Materials & Interfaces*, vol. 5, pp. 3607-3613, (2013).

[13] G. Z. Xing, *et al.*, "Defect-induced magnetism in undoped wide band gap oxides: Zinc vacancies in ZnO as an example," *Aip Advances*, vol. 1, Jun (2011).

[14] M. Kapilashrami, *et al.*, "Transition from ferromagnetism to diamagnetism in undoped ZnO thin films," *Applied Physics Letters*, vol. 95, Jul 20 (2009).

[15] T. C. Kaspar, *et al.*, "Lack of ferromagnetism in n-type cobalt-doped ZnO epitaxial thin films," *New Journal of Physics*, vol. 10, p. 055010,(2008).

[16] M. Opel, *et al.*, "Nanosized superparamagnetic precipitates in cobalt-doped ZnO," *European Physical Journal B*, vol. 63, pp. 437-444, (2008).

[17] T. Tietze, *et al.*, "XMCD studies on Co and Li doped ZnO magnetic semiconductors," *New Journal of Physics*, vol. 10, p. 055009, (2008).

[18] J. R. Neal, *et al.*, "Room-temperature magneto-optics of ferromagnetic transition-metal-doped ZnO thin films," *Physical Review Letters*, vol. 96, May 19 (2006).

[19] S. M. Heald, *et al.*, "X-ray absorption fine structure and magnetization characterization of the metallic Co component in Co-doped ZnO thin films," *Physical Review B*, vol. 79, (2009).

[20] T. C. Kaspar, *et al.*, "Hidden ferromagnetic secondary phases in cobalt-doped ZnO epitaxial thin films," *Physical Review B*, vol. 77, (2008).

[21] D. S. Score, *et al.*, "Magneto- optical properties of Co/ZnO multilayer films," in *International Conference on Magnetism (ICM 2009)*, Karlsruhe, GERMANY,(2009).

[22] J. G. Lu, *et al.*, "Carrier concentration dependence of band gap shift in n-type ZnO : Al films," *Journal of Applied Physics*, vol. 101, Apr 2007.

[23] B. B. Straumal, *et al.*, "Grain boundaries as the controlling factor for the ferromagnetic behaviour of Co-doped ZnO," *Philosophical Magazine*, vol. 93, pp. 1371-1383, (2013).

Chapter 7

Conclusions

7.1 Conclusion

The work described in this thesis is divided into three sections: the first section is concerned with the growth of thin films of Graphite and Graphene, and describes measurements of their characteristics in the visible region over an energy range of 1.5-4.5 eV using optical absorption and magnetic circular dichroism MCD simultaneously with the Faraday rotation FR at room temperature. The second section focuses on an investigation of the magneto-optical studies of non-magnetic ZnO, with and without Al doping using MCD. The final section reports an investigation of the magnetism and magneto-optical studies of ZnCoO and ZnCoAlO thin films in order to gain a better understanding of the origins of magnetism in doped ZnO.

Graphite thin films were grown on sapphire substrates by two different techniques: PLD and a spin coating technique, where only the films made by PLD have been studied for this thesis as they were better quality than those made by spin-coating. All the graphite films were made with a substrate temperature at 450^{o}C and at under base pressure for various deposition times and thicknesses. Graphene thin films were prepared by the chemical vapour deposition technique CVD on the same sapphire substrates.

This was done in order to compare the FR for graphite with the theoretical estimate and to make the first measurement of the MCD for graphite and both MCD and FR for graphene in the spectral region. Magneto-optical measurements were performed on graphite and graphene films to measure the MCD and FR spectrum in the visible region. The Dektak surface profilometer was used to measure the thickness of the graphite films. This was compared with the estimated thicknesses obtained from the optical absorption data for the part of the film that was oriented perpendicular to the substrate, using parameters taken from the bulk. This was to estimate the effective thickness for the part of the film that was oriented perpendicular to the substrate. In addition, the structure and crystallization measurements were characterized using AFM and XRD respectively, also just for graphite films. The results indicated that the films made by PLD were only partially oriented with the c-axis perpendicular to the plane of the film.

Similar spectral behaviour of the FR and the MCD spectra were detected for graphite films, whereas the magnitudes were different due to the uncertainty measurements for the aligned grain thickness.

Larger effects were shown for the FR and MCD measurements in graphene films, with strong exciton energy features at ~3.7eV and 3.9eV respectively, as measured by the MCD.

The second project was to explore the use of the MCD, to study the gap states in non-magnetic ZnO films grown by two methods:

A- Molecular beam epitaxy (MBE) technique; to grow O-polar and Zn-polar ZnO films of 400 nm thickness on a sapphire substrate.

B- PLD technique; to grow (ZnAl)O thin films with (1 and 2) % of Al_2O_3 dopant, on sapphire substrate also with various thicknesses .

The MCD and absorption spectra for all films were performed in an energy range between 1.7 and 4.5 eV at room temperatures.

The MCD spectra for the polar ZnO based films were similar, and showed a broad signal in the high energy range, which is a result of the spin-polarised states in the films. Nevertheless, the Zn-polar film has more spin-polarised gap states.

A weak, positive MCD signal was detected at low energies for ZnO films doped with 1%Al, because of the extra electrons added to the polarized gap states from 1% Al doping. Also, the existence of singly ionised oxygen vacancies in the ZnO matrix was determined by MCD. As a conclusion, a high performance of the MCD in weakly absorbing materials in the visible region is very probable highly expected.

The third project was to investigate the origin of the ferromagnetism observed in ZnCoAlO and ZnCoO thin films. A sequence of various targets grown under different conditions was prepared; this was described in chapter 6 section (6.3.1). All films were grown at base pressure at 400^{o}C on sapphire substrates, for depositions times of 4, 8 and 16 minutes. The thicknesses of the films were determined using a Dektak profilometer. X-ray diffraction (XRD) was utilized to identify the structural properties of all the films. SQUID magnetometry was used to measure the magnetic properties: hysteresis loops and the field cooled - zero field cooled (FC/ZFC) magnetisations, of the films in the range 5-300 K. MCD data were obtained over an energy range of 1.5-3.5 eV.

We have found that thicknesses and grain size both together have an important role in explaining the behaviour of the MCD signal, thus thin films with small grain size showed a big magnetization and a positive MCD signal. It has found that a high temperature target annealing decreases the percentage of nano particle in the films.

7.2 Future Work

Since, graphite and graphene are very competitive materials, optically and electronically. I would like to investigate other methods of making graphite films to see if it were possible to obtain better quality films with more alignment, to compare with theory. The MCD results for graphene were very dramatic, these were clearly very difficult experiments, therefore, I would like to repeat them. In addition, I would continue studying the optical and magneto-optical properties for these films in order to get a better understanding of the energy states and the structure.

I contributed to a published work with Dr Ying (Appl. Phys. Lett. 109, 072403 (2016) on Co doped ZnO, which involved only three different pressures: base pressure, 10mTorr and 100mTorr for different thicknesses. It would be interesting to grow films in a wider range of deposition pressures, with the same thicknesses in order to investigate the origin of the magnetism within the band gap. Also different samples under various growth conditions could be prepared in order to obtain the nanoparticles inclusion with different sizes. Then I would perform more structural measurements such as EXAFS, XRD and AFM to gain additional information about the films.

In addition, low temperature MCD measurements for the current films or future growth films could be of great interest, since films may show several different behaviors due to secondary phases that can be only detectable at low temperatures, because, as signals from such phases may be weak at high temperatures.

Growth reproducibility for TM doped ZnO films is one of the main concluded difficulties encountered in this work. The guarantee of getting the same properties from two similar films grown under identical conditions is poor. Therefore, despite our efforts, unusual and surprising results for these films are predicted, due to the uncontrolled growth conditions, despite our efforts. An example of the uncontrolled factors is the laser plume, which is a very important factor that effects film quality. This will have an effect on film crystallinity and defect concentration in the sample. Hence, the film's magnetisation will be also affected due to the effect of defects on the carrier concentration. Therefore, a better way to prepare reproducible films is definitely required.